ISTANBUL TECHNICAL UNIVERSITY ★ GRADUATE SCHOOL

DESIGN OF BORON DOPED (NICKEL MANGANESE COBALT CONTAINING) NMC 811 CATHODE ACTIVE MATERIALS

M.Sc. THESIS

İbrahim Can TOPAKTAŞ

Department of Metallurgical and Materials Engineering

Materials Engineering Programme

NOVEMBER 2024

ISTANBUL TECHNICAL UNIVERSITY ★ GRADUATE SCHOOL

DESIGN OF BORON DOPED (NICKEL MANGANESE COBALT CONTAINING) NMC 811 CATHODE ACTIVE MATERIALS

M.Sc. THESIS

İbrahim Can TOPAKTAŞ
(506201402)

Department of Metallurgical and Materials Engineering

Materials Engineering Programme

Thesis Advisor: Prof. Dr. Özgül KELEŞ

NOVEMBER 2024

İSTANBUL TEKNİK ÜNİVERSİTESİ ★LİSANSÜSTÜ EĞİTİM ENSTİTÜSÜ

BOR KATKILANMIŞ (NİKEL MANGAN KOBALT İÇEREN) NMC811 KATOT AKTİF MALZEMELERİNİN TASARIMI

YÜKSEK LİSANS TEZİ

İbrahim Can TOPAKTAŞ
(506201402)

Metalurji ve Malzeme Mühendisliği Anabilim Dalı

Malzeme Mühendisliği Programı

Tez Danışmanı: Prof. Dr. Özgül KELEŞ

KASIM 2024

İbrahim Can TOPAKTAŞ, a M.Sc. student of ITU Graduate School student ID 506201402 successfully defended the thesis/dissertation entitled "DESIGN OF BORON DOPED (NICKEL MANGANESE COBALT CONTAINING) NMC 811 CATHODE ACTIVE MATERIALS", which he prepared after fulfilling the requirements specified in the associated legislations, before the jury whose signatures are below.

Thesis Advisor :	**Prof. Dr. Özgül KELEŞ** Istanbul Technical University	.....
Jury Members :	**Assoc. Prof. Dr. Billur Deniz KARAHAN** Istanbul Technical University	.....
	Dr. Vildan BAYRAM KARAKUŞLU TÜBİTAK RUTE	.....

Date of Submission : 22 October 2024
Date of Defense : 21 November 2024

To my beloved family,

FOREWORD

First of all, I am grateful to my thesis advisor Prof. Dr. Özgül KELEŞ for giving me the opportunity to work in this study and for important contributions not only as an academic but also as a human being during my thesis work. Also, I would like to thank Assoc. Prof. Dr. Billur Deniz KARAHAN for contributions to my thesis with her great knowledge and valuable guidance.

I would like to thank Dr. Arda KOCAMAN for his contributions to the realization of the experiments in the thesis. I would like to thank also to Research Assistant M. Sc. İpek TUNÇ and M. Sc. M. Humza ASHRAF for their support in my laboratory work. Yiğit Bürümlü, Mehmet Yılmaz, Gülgün Zehra Şenyurt, Gizem Burcu Bilgin, Muhammet Safa Sak and Arife Ezgi Oturak my laboratory colleagues, for their support and contributions during experiments.

I also thank İstanbul Medipol University and REMER (Regenerative and Restorative Medicine Research Center) for characterization of materials.

Finally, I would like to express my gratitude to TUBITAK for financial support as a scholarship throughout my thesis. This study is financially supported by TUBITAK under the contract of ILATERA Environmentally Compatible Sustainable Advanced Vehicle Technologies Project no:22AG018) .

November 2024

İbrahim Can TOPAKTAŞ
(Metallurgical and Materials Engineer)

TABLE OF CONTENTS

Page

ABBREVIATIONS

CV	**:** Cyclic Voltammetry
DFT	**:** Density Functional Theory
EV	**:** Electric Vehicles
ICE	**:** Internal Combustion Engine Vehicles
LFP	**:** Lithium Iron Phosphate
NCA	**:** Nickel Cobalt Aluminium Oxide
PE	**:** Polyethylene
PP	**:** Polypropylene
PV	**:** Polyvinyl
SEI	**:** Solid Electrolyte Interface
SEM	**:** Scanning Electron Microscope
TM	**:** Transition Metal
XRD	**:** X-Ray Diffraction
ZEV	**:** Zero Emission Vehicles
ALD	**:** Atomic Layer Deposition

SYMBOLS

^{o}C	**:** Celsius
Å	**:** Angstrom
µm	**:** Micrometer
nm	**:** Nanometer
A	**:** Ampere
V	**:** Voltage
RPM	**:** Round per minute

LIST OF TABLES

Page

LIST OF FIGURES

Page

DESIGN OF BORON DOPED (NICKEL MANGANESE COBALT CONTAINING) NMC 811 CATHODE ACTIVE MATERIALS

SUMMARY

Many countries have announced that they will gradually ban the sale of internal combustion engine vehicles (ICE) between 2025 and 2050 under the zero emission policy, and only zero emission vehicles (ZEV) will be sold in the near future. Nowadays, there are many brands that produce electric vehicles (EV) and they are constantly making new investments. In general, steps are being taken to improve the batteries of electric vehicles, whose biggest problem is range. According to 2023 data, lithium ion batteries have a market volume of $55 billion, and many researchers expect a compound annual growth rate (CAGR) of around 20% by 2032.

Although lithium had been utilized previously in 1980, Goodenough was the first to employ a transition metal as a cathode active material in a layered (2D) structure, $LiCoO_2$ (LCO). Then, because LCO batteries did not function at high charging rates and had a safety issue at high temperatures, due to the close ionic diameter of the Ni^{2+} ion and the Li^+ ion, they were replaced by $LiNiO_2$ (LNO) chemistry. When lithium leaves the cathode during charging, the Ni^{2+} ion fills the lithium gaps, closing the passageway of lithium. It made diffusion difficult and caused loss of capacity in the battery. Later, $LiMnO_2$ (LMO) replaced LCO as it was economically convenient and environmentally friendly. LMO, which preserved its structure well especially at high temperatures, experienced capacity loss as a result of long cycles. Then, alternatively $LiFePO_4$ (LFP) was utilized as cathode active material due to its environmentally friendly behavior, and high electrochemical stability at 3.5V. Later, while the specific capacity was increased by doping Ni into the LCOs, Al is added into the structure to stabilize it. $Ni_{0.8}Co_{0.15}Al_{0.05}$ (NCA) structure offers high electrochemical performance, however, its use is restricted in some places due to security problems.

NMC contains nickel, manganese and cobalt. It has been studied extensively because it offers high energy and power densities. NMC cathodes were produced in different compositions such as NMC333, NMC532, NMC622, NMC811 to optimize the capacity and the cycle life. The studies reveal that increasing Ni content in chemistry, increases the capacity of the cell but causes several problems such as chemical instability in the structures hence weak capacity retention over cycles.

Today, while NMC cathode active materials can be produced with many techniques, co-precipitation method stands forward as it enables to fabricate particles with narrow particle-size distribution, high tap density with spherical morphology. The process consists of two steps: precipitation and calcination.

The morphology, the structure and size of the powders obtained from the co-precipitation method are greatly affected by precipitation (pH, mixing temperature, ions concentration, mixing duration and environment) as well as calcination parameters (temperature, duration, $LiOH/M(OH)_2$ ratio, partial oxygen pressure).

Therefore, in order to fabricate 5-15 micrometer sized, spherical shaped NMC811 powders via coprecipitation researchers have realized many optimization studies in the past. NMC811 suffers from low initial coulombic efficiency and capacity retention over long cycling. Structural, morphological and chemical analyses reveal that 'cation mixing', phase transformation in cycling, microcracking and hence oxygen evolution from the structure are the main problems encountered in the use of NMC811.

Cation mixing is the electrochemical transformation of the crystal structure from the layered state to the rock-salt phase during the operation of the battery. Cation mixing occurs when the low-valence metal ions (Ni^{2+}) migrate to the Li^{+} ion layer and replace the Li^{+} ions. Due to the low difference between the ionic diameters of Ni^{2+} (0.69Å) and Li^{+} (0.76Å) ions diameters among Ni^{2+}, Co^{2+} and Mn^{2+} ions, the probability of Li^{+} ions being in the cation mixing with Ni^{2+} is higher than others. Cation mixing is not only formed during the synthesis of the material but can also be formed during the use of the battery, by redox reactions. Cation mixing (Ni^{2+}/Li^{+}) causes the system to be unstable thermodynamically and Ni reaches Ni^{2+} from high valence to low valence, causing Li and O to separate from the system, resulting in the loss of these elements and ultimately performance losses in the battery. The oxygen release from the structure can lead to safety problems since organic electrolyte systems are generally used.

Structural analysis shows that NMC811 follows various phase transformation in cycling: from hexagonal to monoclinic (H1-M), from monoclinic to hexagonal (M-H2) and from hexagonal to a hexagonal structure with different lattice parameters (H2-H3). Electrochemically, the transformation from H2 to H3 phase between 4.15-4.2 V causes shrinkage around 3.7% in the c-direction in the hexagonal lattice and as a result, mechanical strain in the cathode active material, this strain causes micro cracks in the structure and leads to a decrease in cycle performance.

While one of the ways to eliminate these obstacles is to add Li and O to the structure or to make a surface coating to stabilize the electrode/electrolyte interface, another solution is to control these transformations by doping the structure.

Use of boron in doping becomes prominent as boron has high polarizing power due to its 3+ valence and small radius (0.098 nm.) and has strong and short bond length with oxygen leading to preventing oxygen release. Literature review reveals that two different strategies may be used to dop boron in the NMC chemistry. One is to doping boron in coprecipitation and the other is doping boron during calcination. The mechanism behind boron doping to the NMC structure during coprecipitation is that the (003) surface energy of the hydroxide is reduced compared to the {104} surfaces, thus providing the formation of primary particles oriented radially in this direction leading to the elongation of the crystallites in rod and needle shapes. Here in, the amount of boron doping is known to be crucial in the crystallization as B^{3+} cation may position in tetrahedral and octahedral sites (CN = 4 for 0.11 Å and CN = 6 for 0.27 Å) due to their small ionic radius. While the B^{3+} ion positioned in the octahedral sites will cause the cell to shrinkage in the c direction due to its small ionic radius compared to the TM ions but the B^{3+} ion positioned in the tetrahedral sites in the Li layer will cause expansion in the a and c direction. Moreover, the boron doping in calcination with lithium hydroxide reduces the lithium ions in the structure and prevents the development in the (003) direction, thus preventing the formation of the desired layered structure. The chemistry and amount of boron doping are quite effective in the performance of NMC 811.

In NMC structures, by-products such as Li_3BO_3, $LiBO_2$, $Li_2B_4O_7$ are obtained as a result of the heat treatment of boron source with LiOH. It is observed that the formation of these by-products increases the cation mixing in the structure as the lithium consumption. Li-rich heat treatments are preferred in boron doping studies.

In this study, a investigation is realized to investigate the effect of boron doping on NMC811 electrochemical performance. By adding boron in the coprecipitation and calcination steps of the cathode active material production process, the hypothesis put forth here is to examine the impact of the different characteristics of the B-doped NMC811 material on the electrochemical performance. No doping applied precursor named as 'NMC811OH' and boron-doped NMC811 named as 'NMC811OH1B' were successfully synthesized by co-precipitation method. NMC811OH and NMC811OH1B secondary particles with a size of approximately 10-15 μm and a spherical structure were produced. Galvanostatic tests reveal that NMC811 cathode active material without boron doping and calcined in air atmosphere (named as NMC811OH-air) delivers 160 mAh/g first charge capacity at C/10 and after 100 cycles at C/3 and C capacity retention are found to be 78% and 88% respectively, NMC811 cathode active material without boron doping and calcined in oxygen atmosphere so called NMC811OH-Ox delivers 203 mAh/g first charge capacity at C/10 and after 100 cycles at C/3 and C capacity retention are found to be 96.4% and 94.7% respectively. NMC811 cathode active material with boron doping (H_3BO_3) during co-precipitation and calcined in oxygen atmosphere named as NMC811OH1B-Ox delivers 188 mAh/g first charge capacity at C/10 and after 100 cycles at C/3 and C capacity retention are found to be 88% and 92% respectively and NMC811OH is mixed with LiOH and boron source (H_3BO_3) during calcination so called NMC811OH-Ox1B delivers 156 mAh/g first charge capacity at C/10 and after 100 cycles at C/3 and C capacity retention are found to be 88% and 89.67% respectively.

I(003)/(104) ratio (inverse relationship with cation mixing) are found to be 1.22, 1.24, 1.22 and 1.17 for NMC811OH-air, named as NMC811OH-Ox, NMC811OH1B-Ox and NMC811OH-Ox1B. In all conditions calcined particles are sustained their spherical particle morphology and sizes being in the range of 10-15 μm. The galvanostatic performance shows that 1% H_3BO_3 doping during coprecipitation was insufficient to improve capacity retention compared to no doped NMC811OH.

To further study the interaction of CAM with Li, potentiostatic cyclic voltammetry test is applied. For each electrode, peaks related to H1-M, M-H2 and H2-H3 transformations are noted, as expected. A right shift was detected in the H2-H3 peak in boron doped samples, but after 4 cycles, the loss in capacity peak intensity was found to be greater than the no doped sample in an oxygen environment and was associated with the oxygen loss in the structure and the capacity loss in cycle tests. The findings of this work highlights the importance of firstly Li/TM amount for boron source mixed with lithium hydroxide in calcination causing lithium deficiency caused by by-products or coating on the surface leading to cation mixing, poor charge-discharge capacity, capacity retention and high impedance. Boron doped via co-precipitation NMC811 sample have showed better electrochemical performance caused by better secondary particle morphology but 1% H_3BO_3 doping during coprecipitation is insufficient to improve capacity retention compared to undoped NMC811 sample. In the calcination processes carried out in oxygen and air, higher capacity was obtained due to the denser and more oriented primary particle structure with the presence of an oxygen-rich environment and better capacity retention due to the pore distribution in the internal structure and particle orientation.

BOR KATKILANMIŞ (NİKEL MANGAN KOBALT İÇEREN) NMC811 KATOT AKTİF MALZEMELERİNİN TASARIMI

ÖZET

Günümüzde birçok ülke sıfır emisyon poliçesi altında 2025-2050 dönemleri arasında kademeli olarak içten yanmalı motorlu araçların (ICE) satışını yasaklayıp sadece sıfır emisyon araçları (ZEV) satışı gerçekleştirmeyi planlamaktadır. Bu nedenle pek çok otomobil üreticisi filolarına yeni tasarım elektrikli araçları (EV) katmak için sürekli yatırım yapıyorlar. Bu yatırımlar ise genel olarak en büyük problemleri menzil olan elektrikli araçların bataryalarını geliştirmeye yönelik adımların atılmasına da zemin hazırlıyor. 2023 yılının verilerine göre lityum iyon bataryaların dünyadaki pazar büyüklüğü 55 milyar $ ve 2032 yılına birçok araştırmacı bu alanda yaklaşık %20 bileşik yıllık büyüme hızı (CAGR) bekliyor.

Lityum tarihi incelendiğinde 1980 yılından önce lityum kullanılmış olsa da Goodenough, katot aktif malzemesi olarak katmanlı (2D) bir yapıda geçiş metali içeren $LiCoO_2$ (LCO)'yi kullanan ilk kişiydi. Bu lityum iyon pillerinin geliştirilmesinde önemli bir noktaydı ve lityum iyon pillerinin önünü açtı. Daha sonrasında, LCO pillerin yüksek şarj hızlarında çalışmaması ve Ni^{2+} iyonunun Li^{+} iyonu ile benzer iyonik çapları nedeniyle yüksek sıcaklıklarda güvenlik sorununa sebep olduğu için yerini $LiNiO_2$ (LNO) kimyasına bırakmıştır. Lityum şarj sırasında katodu terk ettiğinde, Ni^{2+} iyonu lityum boşluklarını doldurarak lityumun geçiş yolunu kapatır. Bu, difüzyonu zorlaştırır ve pilde kapasite kaybına neden olur. Daha sonra, ekonomik olarak uygun ve çevre dostu olduğu için $LiMnO_2$ (LMO) LCO'nun yerini aldı. Özellikle yüksek sıcaklıklarda yapısını iyi koruyan LMO, uzun çevrimler sonucunda kapasite kaybı problemi yaşadı. Alternatif olarak sonrasında, çevre dostu davranışı olan ve 3,5 V'da yüksek elektrokimyasal kararlılığı nedeniyle katot aktif malzemesi olarak $LiFePO_4$ (LFP) kullanıldı. Daha sonra, LCO'lara Ni katkısı yapılarak özgül kapasite artırılırken, yapıya stabilize etmek için Al eklendi. $Ni_{0.8}Co_{0.15}Al_{0.}$ (NCA) yapısı yüksek elektrokimyasal performans sunar, ancak güvenlik sorunları nedeniyle bazı yerlerde kullanımı kısıtlanmıştır.

En güncel ve popüler NMC nikel, manganez ve kobalt içerir. Yüksek enerji ve güç yoğunlukları sunduğu için kapsamlı bir şekilde incelenmiştir. Kapasiteyi ve çevrim ömrünü optimize etmek için NMC333, NMC532, NMC622, NMC811 gibi farklı bileşimlerde NMC katotları üretilmiştir. Çalışmalar, kimyada Ni içeriğinin artırılmasının hücrenin kapasitesini artırdığını ancak yapılarda kimyasal kararsızlık ve dolayısıyla çevrimler boyunca zayıf kapasite kapasite gibi çeşitli sorunlara neden olduğunu ortaya koymaktadır.

Günümüzde, NMC katot aktif malzemeleri birçok teknikle üretilebilirken, birlikte çöktürme yöntemi dar parçacık boyutu dağılımına, küresel morfolojiye sahip yüksek tap yoğunluğuna sahip parçacıklar üretmeyi mümkün kıldığı için öne çıkmaktadır. Sürecin pratik olarak büyük miktarlarda toz üretmeyi mümkün kılması da

yatırımcıların dikkatini çekmektedir. Süreç iki adımdan oluşmaktadır: birlikte çöktürme ve kalsinasyon.

Birlikte çöktürme yöntemiyle elde edilen tozların morfolojisi, yapısı ve boyutu, çökelme (pH, karıştırma sıcaklığı, iyon konsantrasyonu, karıştırma süresi ve ortam) ve kalsinasyon parametrelerinden (sıcaklık, süre, $LiOH/M(OH)_2$ oranı, kısmi oksijen basıncı) büyük ölçüde etkilenmektedir.

Bu nedenle, 5-15 mikron boyutunda, küresel şekilli NMC811 tozlarını birlikte çöktürme yoluyla üretmek için araştırmacılar geçmişte birçok optimizasyon çalışması gerçekleştirmiştir. Bulguları, NMC811'in uzun çevrim boyunca düşük başlangıç kolomb verimliliği ve kapasite tutma sorunu yaşadığını ortaya koymaktadır. Yapısal, morfolojik ve kimyasal analizler, NMC811 kullanımında karşılaşılan başlıca sorunların 'katyon karışımı', çevrimler sırasında faz dönüşümü, mikro çatlaklar ve dolayısıyla yapıdan oksijen çıkışı olduğunu ortaya koymaktadır.

Katyon karışımı, pilin çalışması sırasında kristal yapının katmanlı durumdan kaya-tuzu (rock-salt) fazına elektrokimyasal dönüşümüdür. Katyon karışımı, düşük değerlikli metal iyonlarının (Ni^{2+}), Li^+ iyon tabakasına göç etmesi ve Li+ iyonlarının yerini almasıyla meydana gelir. Ni^{2+}, Co^{2+} ve Mn^{2+} iyonları arasında Ni^{2+} (0,69Å) ve Li^+ (0,76Å) iyon çapları arasındaki farkın düşük olması nedeniyle, Li^+ iyonlarının Ni^{2+} ile katyon karışımında olma olasılığı diğerlerinden daha yüksektir. Katyon karışımı sadece malzemenin sentezi sırasında oluşmaz, aynı zamanda redoks reaksiyonları ile akünün kullanımı sırasında da oluşabilir. Katyon karışımı (Ni^{2+}/Li^+), sistemin termodinamik olarak kararsız olmasına neden olur ve Ni, Ni^{2+}'ye yüksek değerlikten düşük değerliğe ulaşarak Li ve O'nun sistemden Li_2O ve O_2 olarak ayrılmasına neden olur, bu elementlerin kaybına ve sonuçta pilde performans kayıplarına yol açar. Genellikle organik elektrolit sistemleri kullanıldığından yapıdan oksijen salınımı güvenlik sorunlarına yol açabilmektedir.

Yapısal analiz, NMC811'in çevrimler sonucunda çeşitli faz dönüşümlerini izlediğini göstermektedir: Hekzagonalden monokliniğe (H1-M), monoklinikten hekzagonale (M-H2) ve hekzagonalden farklı kafes parametrelerine sahip hekzagonal bir yapıya (H2-H3) dönüşüm gerçekleşir. Elektrokimyasal olarak, H2'den H3 fazına 4,15-4,2 V arasındaki dönüşüm, hekzagonal kafeste c yönünde yaklaşık %3,7 oranında büzülmeye ve bunun sonucunda katot aktif malzemesinde mekanik gerilmeye neden olur, bu gerilme yapıda mikro çatlaklara neden olur ve çevrim performansında azalmaya yol açar.

Bu problemleri ortadan kaldırmanın yollarından biri yapıya Li ve O eklemek veya elektrot/elektrolit arayüzünü stabilize edecek bir yüzey kaplaması yapmak iken, bir diğer çözüm yolu da yapıya katkılama yaparak bu dönüşümleri kontrol altına almaktır.

Borun katkılama yöntemiyle kullanımı, borun 3+ değerlikli ve küçük yarıçaplı (0,098 nm) olması nedeniyle yüksek polarize edici güce sahip olmasına ve oksijenle güçlü ve kısa bağ uzunluğuna sahip olması ve oksijen salınımını engellemesi nedeniyle öne çıkmaktadır. Literatür taramasına göre, NMC kimyasında borun katkılanması için iki farklı stratejinin kullanılabileceğini ortaya koymaktadır. Biri, birlikte çöktürmeyle borun katkılanması, diğeri ise kalsinasyon sırasında borun katkılanmasıdır. Birlikte çöktürme sırasında NMC yapısına bor katkısının arkasındaki mekanizma, hidroksitin (003) yüzey enerjisinin {104} yüzeylerine kıyasla azalması ve böylece bu yönde radyal olarak yönlendirilmiş birincil parçacıkların oluşmasını sağlayarak kristalitlerin çubuk ve iğne şeklinde uzamasına yol açmasıdır. Burada, bor katkılama miktarının kristalleşmede kritik olduğu bilinmektedir çünkü B^{3+} katyonu küçük iyonik yarıçapları

nedeniyle tetrahedral ve oktahedral bölgelerde (0.11 Å için CN = 4 ve 0.27 Å için CN = 6) konumlanabilir. Oktahedral bölgelerde konumlanan B^{3+} iyonu TM iyonlarına kıyasla küçük iyonik yarıçapı nedeniyle hücrenin c yönünde büzülmesine neden olurken, Li tabakasındaki tetrahedral bölgelerde konumlanan B^{3+} iyonu a ve c yönünde genişlemeye neden olacaktır. Dahası, lityum hidroksit ile kalsinasyon sırasında bor katkılaması yapıdaki lityum iyonlarını azaltır ve (003) yönünde gelişmeyi önleyerek istenen katmanlı yapının oluşmasını engeller. Bor katkılamasının kimyası ve miktarı NMC 811'in performansında oldukça etkilidir.

NMC yapılarda, bor kaynağının lityum hidroksit ile ısıl işlemi sonucunda Li_3BO_3, LiBO, $Li_2B_4O_7$ gibi yan ürünler elde edilir. Bu yan ürünlerin oluşumunun, NMC katmanlı yapının lityumu tükendikçe yapıdaki katyon karışımını artırdığı görülmektedir. Yapıya eklenen bor miktarının artmasıyla yapıdaki lityum eksikliği artmakta ve yapıdaki katyon karışımı artmaktadır. Bor katkılama çalışmalarında Li açısından zengin ısıl işlemler tercih edilmektedir.

Bu çalışmada, bor katkılamasının NMC811 elektrokimyasal performansı üzerindeki etkisini araştırmak için kapsamlı bir araştırma gerçekleştirilmiştir. Katot aktif malzeme üretim sürecinin birlikte çöktürme ve kalsinasyon adımlarında ayrı ayrı borun eklenmesiyle, burada ortaya atılan hipotez, B-katkılanmış NMC811 malzemesinin farklı özelliklerinin elektrokimyasal performans üzerindeki etkisini incelemektir. Katkılanmamış (‘NMC811OH’ olarak adlandırılmıştır) ve bor katkılı NMC811 (‘NMC811OH1B’ olarak adlandırılmıştır) öncülleri birlikte çöktürme yöntemi ile başarıyla sentezlenmiştir. Yaklaşık 10-15 µm boyutunda ve küresel bir yapıya sahip NMC811OH ve NMC811OH1B ikincil parçacıkları üretilmiştir. Galvanostatik testler sonucunda, katkısız NMC811 katot aktif malzemesinin hava ortamında kalsine edilerek (NMC811OH-Air olarak adlandırılır) C/10'da 160 mAsa/g ilk şarj kapasitesi sağladığını ve C/3'te ve C akım hızlarında 100 döngüden sonra kapasitesinin sırasıyla %78 ve %88 miktarda koruduğu, katkısız NMC811 katot aktif malzemesinin oksijen ortamında kalsine edilerek (NMC811OH-Ox olarak adlandırılır) C/10'da 203 mAsa/g ilk şarj kapasitesi sağladığını C/3'te ve C akım hızlarında 100 döngüden sonra kapasitesinin sırasıyla sırasıyla %96,4 ve %94,7 oranda kapasitesini koruduğu, birlikte çöltürme sırasında bor (H_3BO_3) katkılanmış NMC811 katot aktif malzemesinin oksijen ortamında kalsine edilerek (NMC811OH1B-Ox olarak adlandırılır) C/10’da 188 mAsa/g ilk şarj kapasitesi vermiştir ve C/3'te ve C akım hızlarında 100 döngüden sonra kapasitesinin sırasıyla %88 ve %92 olduğu ve NMC811OH numunesinin kalsinasyon sırasında LiOH ve bor kaynağı (H_3BO_3) ile eş zamanlı olarak karıştırıldığında elde edilen numune (NMC811OH-Ox1B olarak adlandırılır) C/10'da 156 mAsa/g ilk şarj kapasitesi vermiş olup ve C/3'te ve C akım hızlarında 100 döngüden sonra %88 ve %89,67 kapasite korunumu sağlamıştır.. Daha sonra I(003)/(104) oranının (katyon karıştırma ile ters ilişkili) NMC811OH-Air, NMC811OH-Ox, NMC811OH1B-Ox sırasıyla 1,22, 1,24, 1,22 ve 1,17 olduğu görülmüştür. Tüm koşullarda kalsine edilmiş parçacıklar 10-15 µm'lik küresel parçacıklar elde edilir. Galvanostatik performans, birlikte çöktürme sırasında %1 H_3BO_3 katkısını, katkılanmımış NMC811'e kıyasla kapasite tutmayı iyileştirmek için yetersiz olduğunu ancak kalsinasyon numunesinde karıştırılmış bor katkılı üretilenden daha iyi performans gösterdiğini göstermiştir.

Katot aktif malzemesinin Li ile etkileşimini daha fazla incelemek için potansiyostatik döngüsel voltametri testi uygulandı. Her elektrot için beklendiği gibi H1-M, M-H2 ve H2-H3 dönüşümleriyle ilgili pikler not edildi. Bu çalışmanın bulguları, öncelikle kalsinasyonda lityum hidroksit ile karıştırılan bor kaynağı için Li/TM miktarının

önemini vurgular ve lityum eksikliğine, dolayısıyla katyon karışımına ve zayıf elektrokimyasal performansa yol açan istenmeyen ikincil parçacık morfolojisinin oluşumuna neden olur. İkinci olarak, birlikte çöktürme sırasında %1 H_3BO_3 katkısının NMC811 malzemesinin kapasite korunum için yetersiz olduğu görülmüştür.

CAM'ın Li ile etkileşimini daha ileri düzeyde incelemek için potansiyostatik döngüsel voltametri testi uygulanır. Her numune için beklendiği gibi H1-M, M-H2 ve H2-H3 dönüşümleriyle ilgili pikler not edildi. Bor katkılı numunelerde H2-H3 piklerde sağa kayma tespit edildi, ancak 4 çevrimden sonra kapasite pik şiddendeki kaybın oksijen ortamında katkısız numuneye göre daha büyük olduğu ve yapıdaki oksijen kaybı ve çevrim testlerindeki kapasite kaybıyla ilişkili olduğu bulundu. Bu çalışmanın bulguları şunları vurgulamaktadır; kalsinasyonda lityum hidroksit ile karıştırılan bor kaynağı için öncelikle Li/TM miktarına bağlı olarak oluşabilecek yan ürünler veya yapı yüzeyinin kaplanması nedeniyle lityum eksikliğine yol açarak katyon karışımına, zayıf şarj-deşarj kapasitesine, kapasite kaybına neden olmaktadır. Birlikte çöktürme yoluyla bor katkılanmış NMC811 numunesi, daha iyi ikincil parçacık morfolojisi nedeniyle daha iyi elektrokimyasal performans göstermiştir; ancak birlikte çöktürme sırasında %1 H_3BO_3 katkılanması, katkısız NMC811 numunesine kıyasla kapasite kaybına iyileştirmek için yetersizdir. Oksijen ve havada gerçekleştirilen kalsinasyonlarda, oksijence zengin ortamda üretilen numunede birincil parçacık yapısının daha yoğun ve daha yönelimli olması nedeniyle daha yüksek kapasite, iç yapıdaki gözenek dağılımı ve partikül yönelimi nedeniyle ise daha iyi kapasite korunumu elde edilmiştir Katot aktif malzemelerinin oluşum mekanizmalarına ve yapı ile ilgili elektrokimyasal davranışlarına olan etkilerini incelemek için ileri analizlere ihtiyaç vardır.

1. INTRODUCTION

Efficient storage and conversion of energy is one of the biggest issues of today. Even if renewable energy sources such as solar energy, wind turbines, geothermal, hydrothermal, and biomass are preferred instead of energy produced from energy sources that cause high carbon emissions such as oil and natural gas, their high costs, low efficiency and the need for suitable environmental conditions for their operation are still problematic. On the other hand, storing and transporting the energy produced are issues that need to be taken into consideration. Battery technologies are important for storage and transportation of energy.

Battery is simply an electrochemical cell in which stored chemical energy is converted into electrical energy. Looking at the history of the battery, the first battery was named "Baghdad Battery" or also known as "Partian Battery" approximately 2000 years ago [1]. Although this battery is not accepted by some sources, it is assumed to have 1.1-2 V range and consists of an iron rod, a copper cylinder, and vinegar as an electrolyte in a clay jar, as seen in Figure 1.1. [1,2].

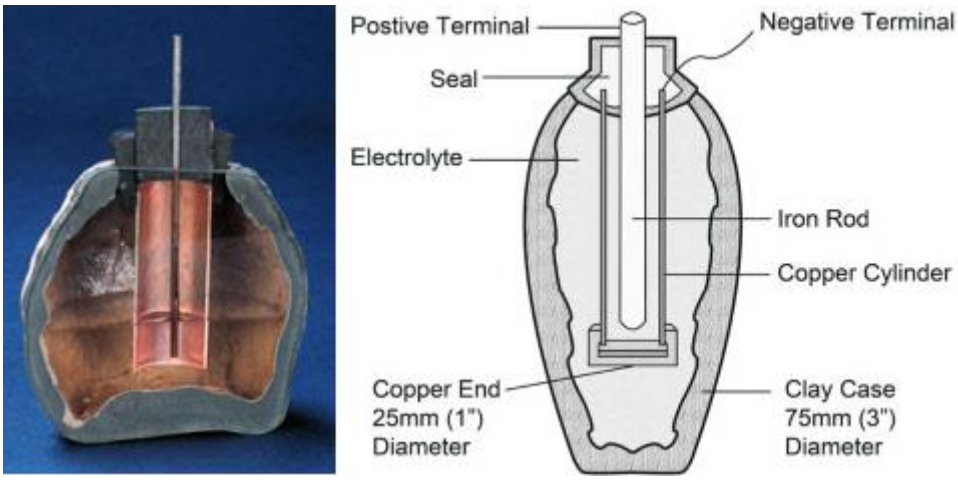

Figure 1.1 : The first battery in history - Partian Battery schematic [2].

In the early 1800s, Luigi Galvani, with whom Italian Alessandro Volta have, suggested that when a frog's legs have touched to metallic wires, legs have moved by passing electricity through the nerves, producing electricity. Alessandro Volta has suggested that it was due to the different properties of the different metal rods in the legs. Later,

in his study, Alessandro Volta has seen that there was a continuous current between two plates made of copper or silver on one side and zinc on the other, separated by cardboard in a container filled with salt water, and this was later called ‘the voltaic pile’. It is considered to be the first battery having 1.1 V [3,4].

All batteries produced until 1859 by Frenchman Gaston Plante were non-rechargeable. Using 10% sulfuric acid solution as an electrolyte along with lead electrodes, Gaston Plante produced a 2 V battery cell [5]. Additionally, the 12 V battery have been produced by connecting 6 battery cells together in a battery pack [6]. Developments in rechargeable batteries have continued and, a nickel-cadmium battery is produced by Swedish Waldemar Junger in 1899 and the nickel-iron battery is produced by Thomas Edison in 1900 [7,8].

Although these batteries have been utilized in many applications, they have had advantages and disadvantages. Lead-acid batteries have low energy density, inefficiency in electrochemical properties, and are prone to have leakage. Nickel-Cadmium batteries have low power, leakage and memory effect [9]. Developments of other sectors lead to a search for new materials for batteries providing light, electrochemically efficient, safe and long cycle life design.

Among alternatives, lithium being the lightest metal was seen to be a suitable element thanks to its high electrochemical properties relative to its weight. At first, lithium has been added to the electrolyte and improvements seen in battery performance [10]. Then, different chemistries of anodes and cathodes have been tested. Until 1978, batteries designed utilizing lithium were primary batteries. Thanks to the layered structure of TiS_2 Wittingham in 1978 has designed a cathode where , Li^+ ions are reversibly stored back in the layered structure of the cathode paving the way for rechargeability for lithium-ion batteries. However, the use of highly reactive lithium as an electrode safety problems [10].

In 1980, Goodenough have invented $LiCoO_2$ cathode material, opening a new perspective to science and technology for today's lithium-ion batteries. In 1991, SONY became the first company to commercialize lithium-ion batteries [11].

Today, batteries are simply classified into two;primary and secondary. Primary batteries are disposable, electrochemical reactions are irreversible and batteries can not be recharged after their use. Examples for primary batteries are alkaline batteries,

lithium primary batteries, zinc air batteries, ant etc. Secondary batteries, unlike primary batteries, are rechargeable batteries. Since the ΔG of the reactions is negative when the battery is being discharged, chemical energy is converted to electrical energy. However, external energy is needed to charge the battery due to ΔG being positive. Pb-acid, Ni-Cd and lithium-ion batteries are examples of secondary or rechargeable batteries [12].

2. LITERATURE

2.1 Lithium Ion Batteries

Lithium ion batteries are used in many household products such as cameras, laptops, flashlights etc., due to their high specific energy [14]. In recent years, many countries have set targets considering the sustainable future of humanity. They have climate policies, therefore they have made plans for 2025-2050s having the zero-emission vehicles (ZEV) in transportation rather than internal combustion engine vehicles (ICE) [15-17]. In order to fulfill these policies many automotive companies have begun to invest heavily in the development of the technologies of EV devices havingLi-ion batteries (Volkwagen, Hyundai, Tesla…) [18]. Figure 2.1 shows the percentage of current and future electric vehicle sales to total vehicle sales and the percentage of usage between 2018 and 2030. The assumptions made on the sales of EV will be 25-50% of total sales by 2030 and also the electric vehicle usage ratio is expected to be between 4% and 8% of the total vehicle usage in 2030 [19]. Li-ion battery market will have a value of around $55 billion in 2023. This value is expected to grow 18% annually until 2032 [19-22].

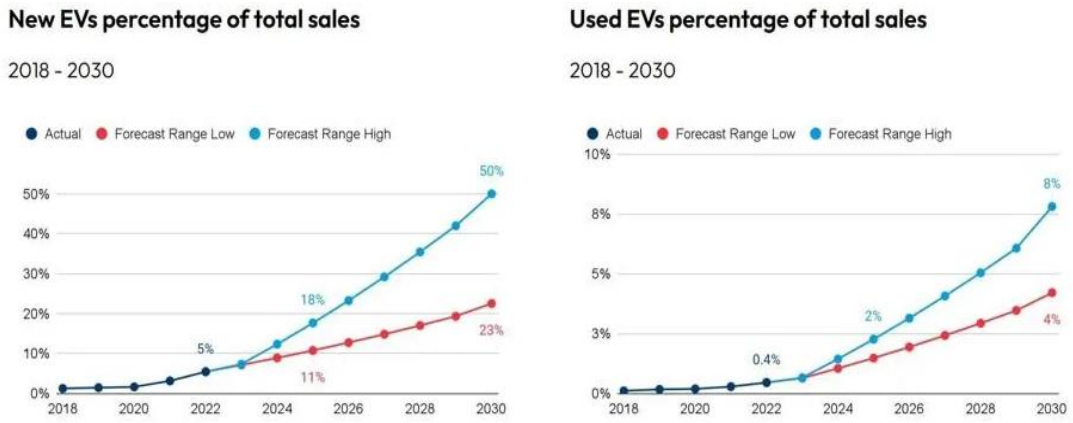

Figure 2.1 : Expectation of EV Sales Growth [19].

Table 2.1 : Zero emissions plans of some countries [15-17].

Estimated date	100% EV	ICE ban
2025	• Norway	
2030	• Iceland • Austria • Netherlands • Israel • Ukraine • United States (50%)	• Japan
2035	• United Kingdom (LDV) • Canada (LDV) • European Union • China	• Chile • United States
2040	• United Kingdom (HDV) • Canada (HDV)	• Argentina
2045	• Chile	
2050	• Mexico • Costa Rica	

2.2 Lithium Ion Battery Working Principle

Lithium ion cells mainly consist of four parts: anode, cathode, electrolyte and separator. In charging Li^+ ions move from the cathode structure through the electrolyte and are stored in the anode structure. During charge, de lithium ions move from cathode to anode (Figure 2.2) [23].

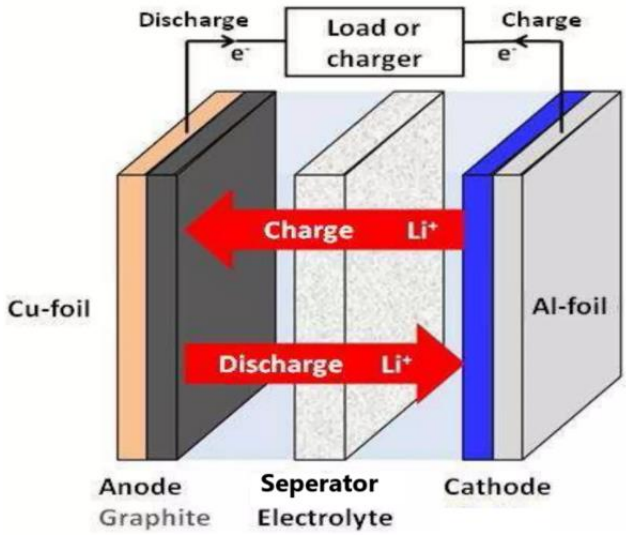

Figure 2.2 : Li-ion cell structure [23].

2.2.1 Anode

The first design requirement for an anode material is having a structure to host Li ions at a reasonably low electrochemical potential versus Li/Li^+, having low volumetric change during cycling, high ionic and electronic conductivity, low cost, low toxicity and high abundance. Graphite is ideally suited for an anode material among others; silicon, tin, lithium titanate, and etc.

Graphite has planar hexagonal networks of carbon atoms (honeycombs) with two different crystalline forms : hexagonal (2H) and rhombohedral (3R). With Van der Waals bonds among layers and having an interplanar distance of 3.36 A, it allows Li^+ to intercalate [24]. It has a theoretical capacity of 372 mAh/g as a result of Li^+ incorporation into graphitic carbon to form LiC_6 reversibly.

Silicon is a high capacity alternative that can store up to ten times more energy than graphite. However, its use is limited by significant challenges such as volume expansion (up to 300%) during charging leading to fracture and loss of battery contact [25]. Although, lithium titanate anodes provide fast charging capabilities and long cycle lifes, has lower energy density than silicon and graphites so less common from graphite [26].

2.2.2 Separator

The separator is a porous and permeable membrane located between the electrodes and in the electrolyte solution to prevent short circuits by preventing physical contact between the cathode and anode in the Li-ion cell. Separators must have high ionic conductivity for Li^+ ion migration between electrodes during charge and discharge cycles with low electronic conductivity for minimizing unwanted electron flow lead to short circuit, having sufficient mechanical resistance enables them to resist stresses that may occur during installation into the separator cell, high chemical and electrochemical stability in electrolyte and high thermal stability to over heating during charge/discharge for battery problems [27].

In commercially available lithium-ion batteries polyolefin based materials such as polyethylene (PE) and polypropylene (PV) have been commonly used. These materials can be used as a single layer, or as multiple layers, such as PE/PP or PP/PE/PP. [28].

Multilayer structures add thickness to the separator, the increase in mechanical resistance with increasing thickness and the decrease in the possibility of short circuit between the anode and cathode so increase the safety of the battery, but increasing thickness reduces the impedance. [28-29].

2.2.3 Electrolyte

Electrolytes are mostly liquid and act as a connection between an anode and a cathode, allowing a conductive path for Li^+ during charging and discharging. Same as separator, electrolyte must have high ionic conductivity facilitating ion mobility and low electrochemical conductivity for the efficiency of a battery. In general, lithium-containing salts such as $LiPF_6$, $LiBF_4$ or $LiClO_4$ have a structure dissolved in carbonate-based organic solvents. Electrolytes can be found in solid or liquid forms. Electrolyte also must be stable over wide voltage (0-5 V) and temperature ranges, do not react with other elements in a cell, and tend not to form by-products. Accessibility and economic suitability are another important issue [30-31].

Liquid electrolytes, the solution of a single ion salt as well as the solution of more than one ion salt in the same solution, have been studied as an innovative structure in recent years. It has been observed that this multi-ion salt structure increases the stability of the electrolyte and also increases its performance. Electrolytes that can be used in a gel form contribute positively to structural stability, just like a multi-ion salt structure, while also increasing electrolyte performance. In addition, solid electrolytes have begun to be studied. Although they seem like a safer choice because they do not leak, their low ionic conductivity and mechanical brittleness constitute a disadvantage compared to liquid electrolytes [30-32].

2.2.4 Cathode

Cathodes are the positive electrodes and store Li in their structures. In general, due to the fact that anode materials provide higher capacity, studies in Li-ion batteries in recent years have mainly focussed on cathode materials. One of the design criteria was to increase lithium ion mobility during charge-discharge, this motivates researchers to design and produce cathode materials that give high energy and power densities and to positively improve reliability, cost and cycleability of the cell [33]. While the layer-structured $LiCoO_2$ transition metal cathode materials produced by Goodenough in 1980 began to be used, over time, $LiMn_2O_4$ from the spinel LiM_2O_4 family and

$LiFePO_4$ structures from the $LiMPO_4$ family with an olivine structure were produced and commercialized [33]. Crystal structure of different cathode materials are given in Figure 2.3. Due to the safety problems of the $LiCoO_2$ structure, its toxicity, and its inability to provide the specific capacity it offers in theory, new chemistries such as NCA and NMC structures are used today with element doping [34]. This has paved the way for innovative chemistries and designs for cathode active material.

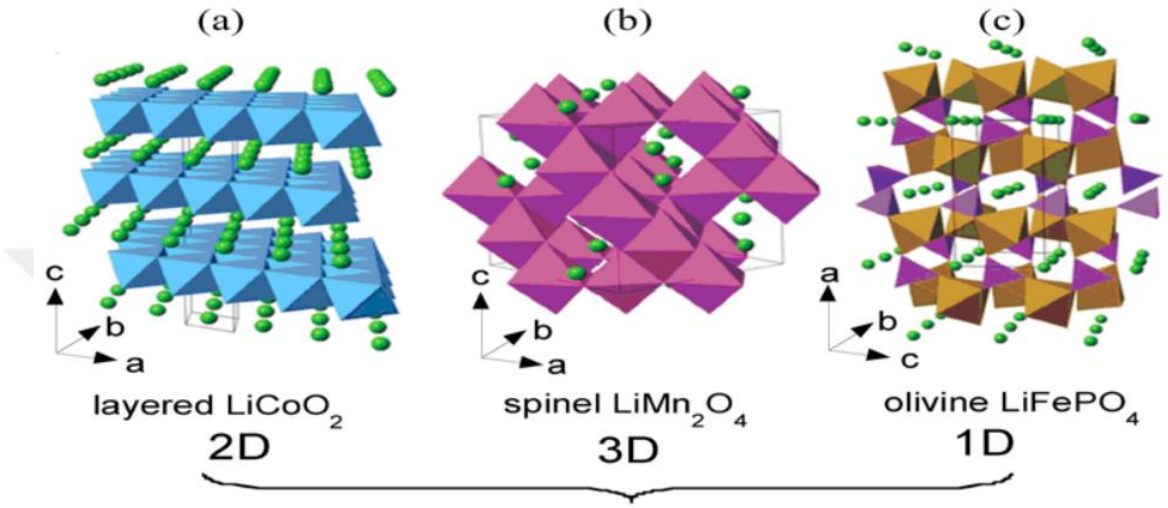

Figure 2.3 : Crystal structure of different cathode materials [33].

2.2.4.1 LCO

LCO is the first commercialized Li-ion battery type. LCO is a member of the space group R3m family of the α-$NaFeO_2$ structure and located in Li 3a and cobalt 3b sites (different [111] planes) in the octahedral structure, and the oxygens are in a tightly packed (ccp) structure. It has an ABC-ABC stack structure arranged in the form of Li-O-Co (Figure 2.4). During discharge, with the migration of lithium to the cathode, Co^{3+} turns into Co^{3+} -> Co^{2+} + Co^{4+} to ensure the ionic balance in the structure. When more than 50% of lithium is de-interclinated, the cathode structure changes from hexagonal to monoclinic [35]. This provides a capacity in the range of 130-140 mAh/g, compared to the theoretical capacity of 280 mAh/g in the 3-4.2 V potential range, causing a large capacity loss [36]. Although they have high specific energy, their specific power is low due to their low discharge current, so they may cause overheating problems in the battery in cases of rapid charge and discharge [37]. LCO is suitable for devices that do not require high power load such as cameras, laptops etc. Furthermore, cobalt is toxic and expensive, which limits its use.

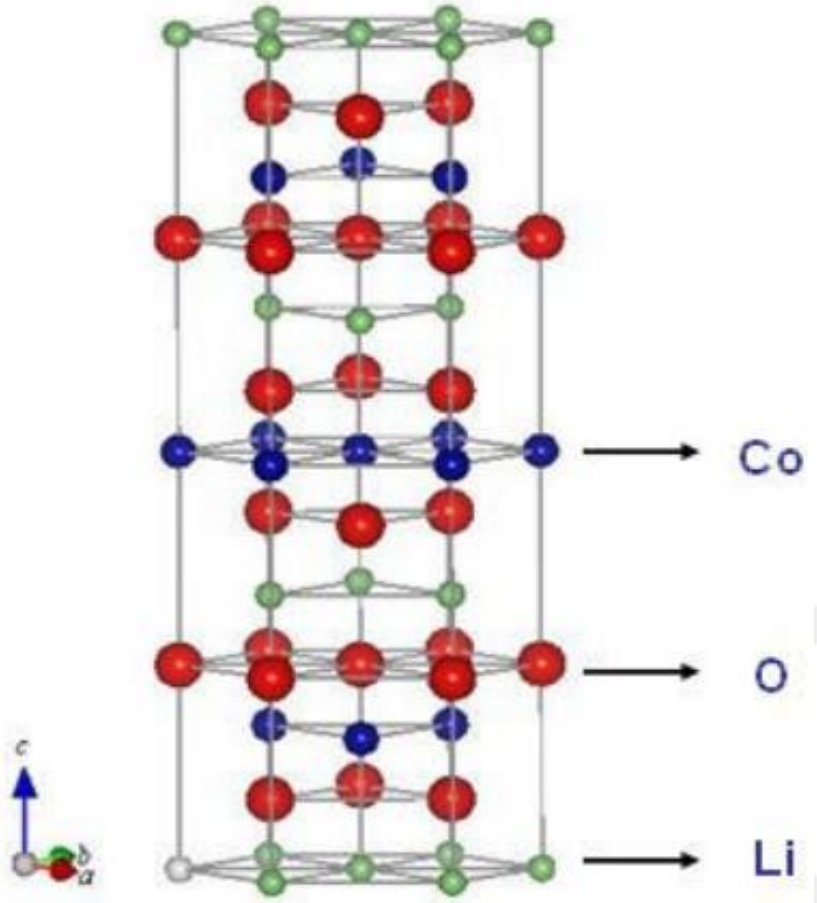

Figure 2.4 : LCO crystal structure [38].

2.2.4.2 LMO

LMO, which emerged as an alternative to LCO, had some advantages over LCO. LMO is cheaper than LCO, safer due to its higher thermal resistance, and rather environmentally friendly since the Mn atom is not as toxic as Co [39]. In theory, the specific discharge capacity is 296 mAh/g, while the theoretical charge capacity is 148 mAh/g. LMO, which has a close cubic package (ccp) structure (Figure 2.5) from the Fd3m space group, turns from Mn^{3+} structure into Mn^{4+} and Mn^{2+} level to balance it due to the Jahn-Teller effect [40]. As a result of the reaction of Mn^{2+} ion with $LiPF_6$ salt, structure deterioration occurs at the cathode and the cycle life of a cell decreases [41]. This causes a transformation from the layered structure to the spinel structure, which limits its rate capacity. Although it is preferred because it is suitable for high temperatures.

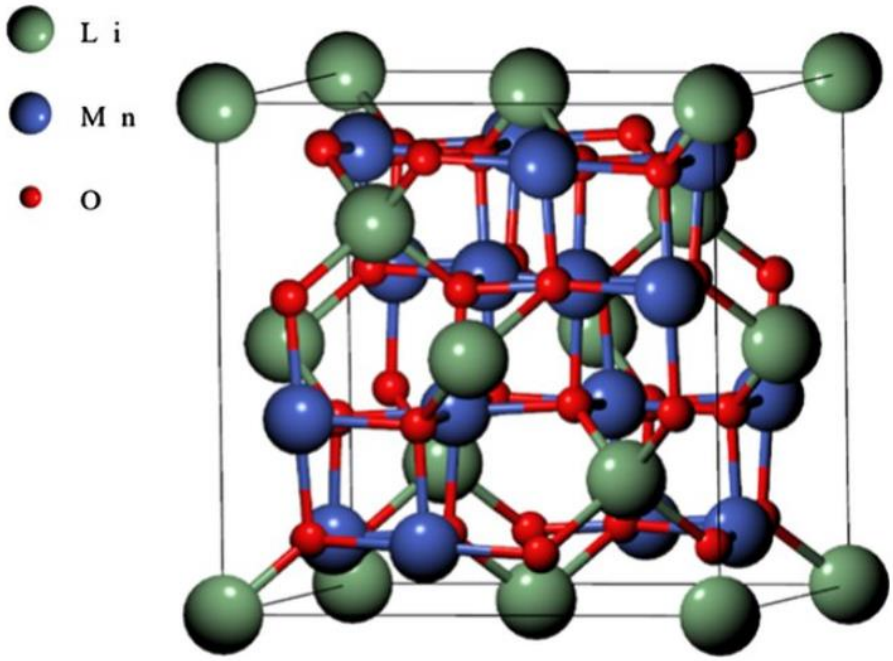

Figure 2.5 : LMO crystal structure [42].

2.2.4.3 LFP

LFP has an olivine structure. The fact that the Fe^{3+}/Fe^{4+} conversion is stable at 3.5V and that $LiFePO_4$ and $FePO_4$ are from the same space group keeps volume expansion to a minimum while providing excellent capacity retention and safety. On the other hand, due to the elements they contain, raw materials are accessible, cheap and have low toxicity [43-45].

Unlike other cathode materials, this cathode material requires an extra modification because it has low electronic conductivity due to its structure. The most common method used to increase electronic conductivity is coating its surface with carbon and/or doping it with other elements such as S, Co and Mn [45,46]. In addition, reducing the particle size to nano level is also studied to improve the cycle performance.

The lithiation mechanism continues until the interface area of this structure, which is assumed to be caused by movement between two phases, falls below the critical surface area over time. They show low specific energy due to a lithiation mechanism that changes over time and depends on the restricted surface area [46,47]. LFP crystal structure is given in Figure 2.6

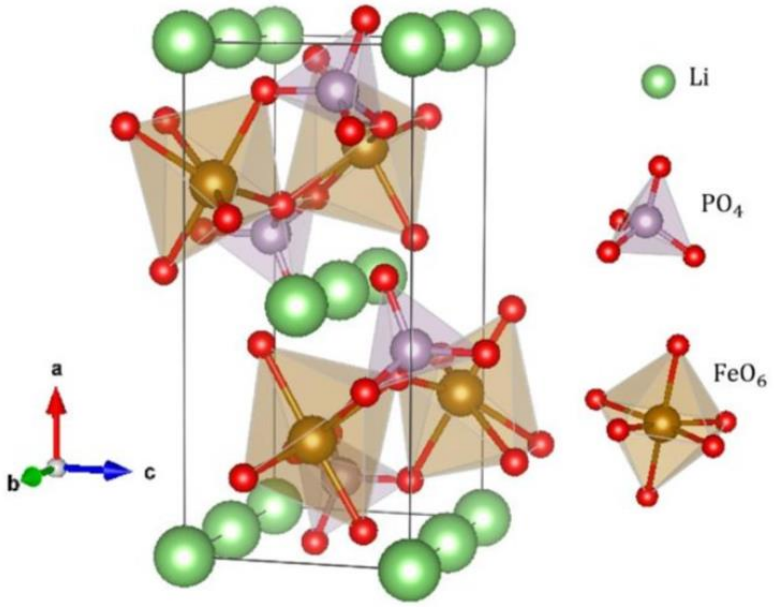

Figure 2.6 : LFP crystal structure [48].

2.2.4.4 NCA

Although LNO ($LiNiO_2$), another member of the LMO_2 family, has started to be used instead of LCO due to its cheapness and high theoretical capacity (275 mAh/g), it replaces Ni^{3+} with Li^+ ions due to the conversion of Ni^{2+} ions to Ni^{4+} ions, which maintain the ionic balance at the cathode during charging. Ni in the lithium layer prevents and slows down lithium migration [49]. This causes capacity loss as a result of long cycles. Afterwards, cathode materials mixed with nickel and cobalt were tried. While Ni provides high specific capacity, Co limits Ni's cation mixing. Over time, a third element, Al, began to be added. While the Al element reduces undesirable phase transformations in the structure as in Co, it improves its thermal resistance as in Mn with the structural improvements provided by Al can alleviate problems such as lithium residues that can lead to thermal runaway, thus reducing the decomposition of transition metals and improving thermal resistance problems, thus reducing capacity loss [10,50]. Generally, the Al content does not exceed 10% in the structure because high Al content causes electrochemical inactivity and reduces specific energy in the structure. Today's $LiNi_{0.8}Co_{1.5}Al_{0.05}$ is a commercialized cathode material. Its sensitivity to high temperature and humidity may cause safety problems [51-53]. NCA crystal structure is given in Figure 2.7

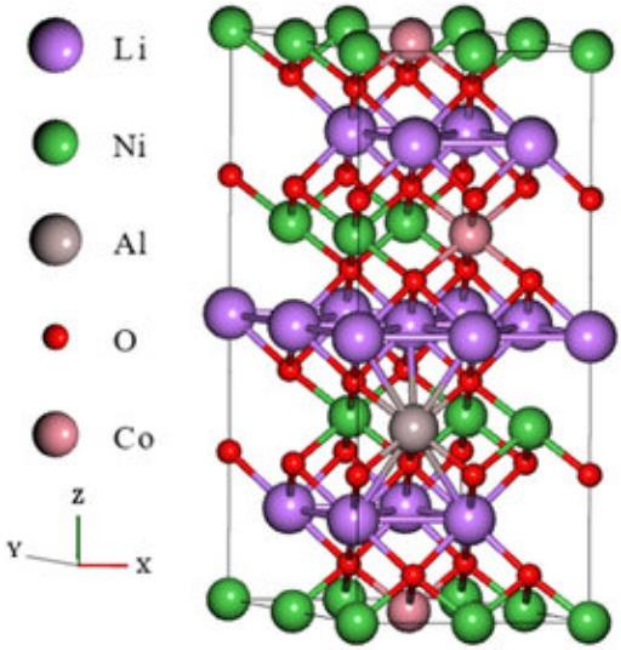

Figure 2.7 : NCA crystal structure [54].

2.3 NMC

NMC is one of the most widely used cathode materials today and is expected to be used even more in the future due to their high energy density, good power output, long cycle life, and improved safety features. Its structure is similar to $LiNiO_2$ and is its Mn and Co doped form (Figure 2.8). Its layer structure is α-$NaFeO_2$ and it is a member of the a $R\bar{3}m$ space group family. It repeats the O3 structure and repeats in the [001] direction as O-Li-O-TM-O-Li-TM-O (Figure 2.9) [55,56].

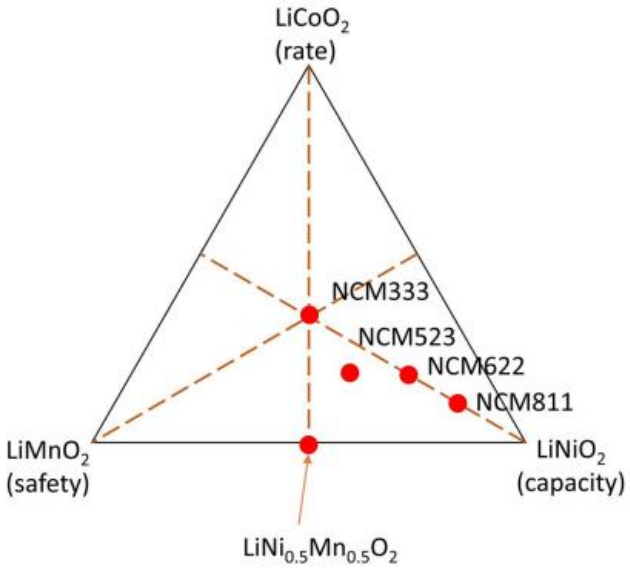

Figure 2.8 : Phase diagram of the ternary system between LNO, LCO and LMO [57].

Manganese always gets the value 4^+, that is, it does not change its valence value during charging and discharging and does not contribute to the capacity (polarizes around 4.5 V) [58]. The fixed valence stabilizes the structure, increases thermal stability, especially at high temperatures, and increases the safety of the NMC structure by preventing overheating during charging and discharging [58-60]. With the presence of the Mn, the strongest TM-TM bonds in the TM layer are provided by Mn^{4+} [58]. The cobalt normally takes the value 3+ in the structure, but can be oxidized to Co^{4+} above 4.4 V. While the Co^{+4} adds a small specific capacity, the Co^{3+} protects the cathode from corrosion and stabilizes the structure, providing longer cycle lives. Since its contribution as Co^{3+} to the structure is greater, the cut-off voltage value of NMC cathodes does not exceed 4.3V [59]. Additionally, the Co^{+4} structure may react with electrolyte, which reduces cycle life. The nickel element provides high specific capacity and energy density to the structure. During delithiation, the oxidation of Ni^{2+} to Ni^{3+} above 3.6 V and from Ni^{3+} to Ni^{4+} above 3.9 V occur depending on Li^+ amount [59,61].

$$\text{Cathode reaction : } LiNiMnCoO_2 \leftrightarrow xLi^+ + xe^- + Li_{1-x}NiMnCoO_2 \quad (2.1)$$

$$\text{Anode reaction : } 6C + xe^- + xLi^+ \leftrightarrow Li_xC_6 \quad (2.2)$$

$$\text{Overall reaction : } LiNiMnCoO_2 + 6C \leftrightarrow LiC_6 + NiMnCoO_2 \quad (2.3)$$

Since cobalt is a toxic element the trend is towards the production of cobalt-low, nickel-rich cathodes (Ni>0.6) with the specific capacity that the nickel element provides to the structure [62,63]. Due to the decreasing Mn and Co in the structure in response to the increasing Ni content, the structure shows poor thermal stability and capacity retention (see Figure 2.10) [46, 64].

As the amount of lithium in the cathode decreases during charging and discharging, H1 (hexagonal) -> M (monoclinic) -> H2 (hexagonal) and H3 (hexagonal c/a ratio is different) transformations occur, respectively. With the irreversible H2-H3 phase transformation, oxygen atoms released from the cathode may react with the electrolyte and form the undesirable spinel and rock-salt structure [66]. Shrinkage may occur in the c-axis and microstrains may occur due to volume change, causing microcracks in the cathode. It is assumed that with some element doping, the reversibility of the H2-H3 phase can be increased and the cycling resistance of the structure can be increased [67-68].

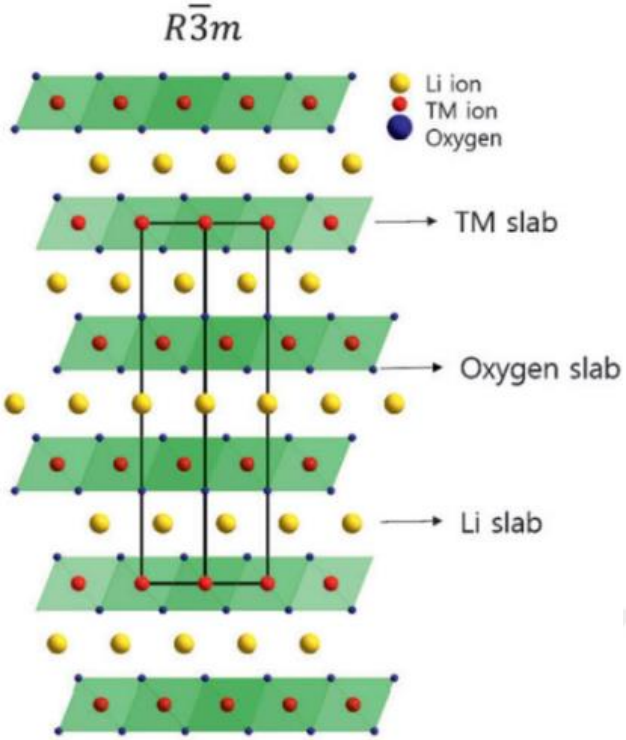

Figure 2.9 : NMC crystal structure [65].

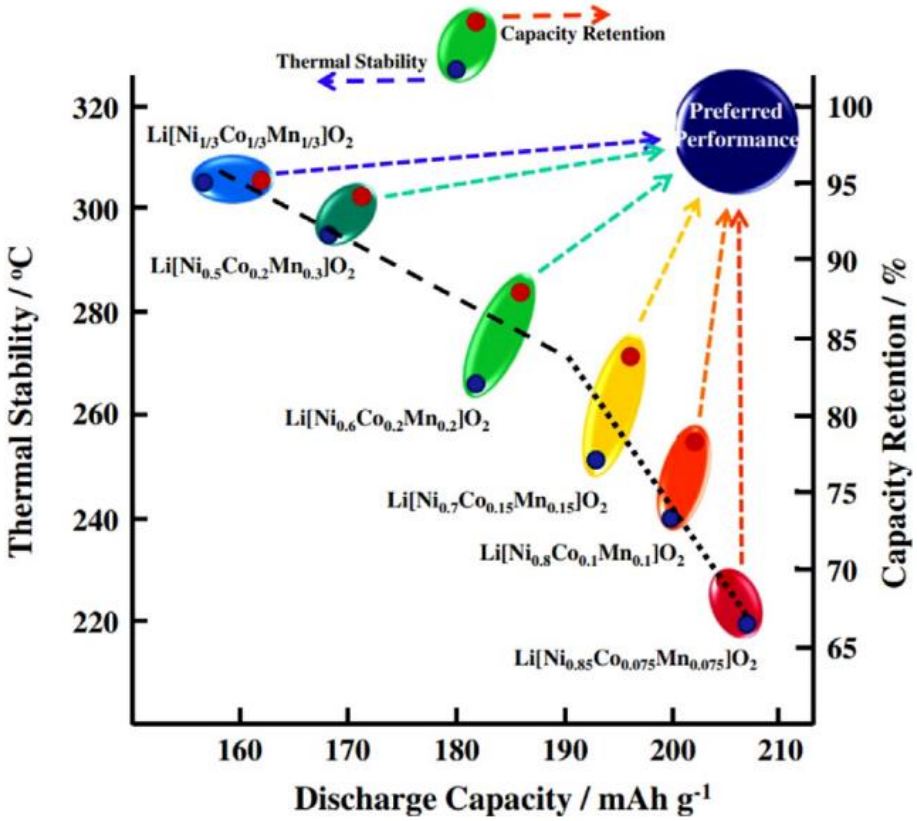

Figure 2.10 : Ni ratio in the structure [65].

After LCO gave low discharge capacity in theory, LNCO structure was formed by adding nickel to the structure. Ni provided capacity increase but LNCO also had

stability problems. A more stable structure was obtained by adding Mn to the structure. From the structure with stereometrically equal Ni, Mn and Co, the amount of Ni was continuously increased in the structure to increase the capacity. NMC111, NMC532, NMC622 and NMC811 structures emerged respectively.

The biggest suffer in Ni-rich cathodes is cation mixing. Due to the close ionic radius of Ni^{2+} (0.69 Å) ions and Li^{+} ions, Ni (0.76 Å) ions penetrate into Li layers. Ni is mixed into the Li layers, makes delithiation difficult and causes the structure to give poor electrochemical performance. [70,71]

General cation mixing detection techniques are given in Table 2.2. Among the methods, powder diffraction XRD and NPD (Neutron Powder Difraction) methods are the most widely used methods in terms of both accessibility and ease of application [72]. While the XRD peaks in NMC materials include TM atoms in the (003) plane, the peak in the (104) plane contains both TM and Li [72]. The intensity ratio of these peaks, I(003)/I(104), is associated with cation mixing . When cation mixing occurs, the I(003) peaking intensity decreases. When the I(003)/I(104) ratio is greater than 1.2, it is considered that the cation mixture is low. Additionally, the separation of (108)/(110) peaks indicates the low cation mixing. The fact that the (006)/(012) pair is separate from each other is related to the crystallinity of the structure [64,74,75]. In Figure 2.11, Relationship between I(003)/I(104) ratio and cation mixture, prepared for NMC811 shown graphically (The cation mixing ratio varies linearly between 0-10 and 1.44 for $I_{(003)}/I_{(104)}$ ratio) [73].

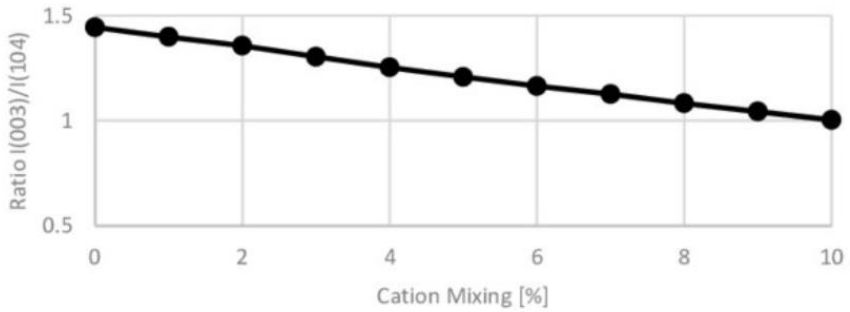

Figure 2.11 : Relationship between $I_{(003)}/I_{(104)}$ ratio and cation mixture, prepared for NMC811 [73].

NMC structures show good hexagonal ordering, resulting in good electrochemical performance. Hexagonal ordering The R-factor is calculated from the ratio ($R=(I_{(006)}+I_{(102)})/I_{(101)}$. Low R value means high hexagonal ordering [74].

Table 2.2 : Cation mixing detecting techniques [72].

Powder diffraction	Electron Microscopy	Other
• XRD	• HADDF STEM	• NMR
• NPD	• ABF STEM	• PDF

When the Ni ratio is very high (Ni≥80%) or the improperly formed crystal structure, the Ni^{2+} valence value shifts to the Ni^{3+} valence due to the regional insufficiency of Co and Mn in the structure (TM-TM bonds made by Ni^{3+} are weaker than Ni^{2+}) [63]. While it causes bond weakening in the structure, it may cause the formation of Mn and Co clusters. These clusters cause phase distortion for future cycles. Cation mixing can occur not only during the production phase, but also after long cycles during electrochemical testing of the battery [76].

2.3.1 NMC production techniques

There are various methods to produce NMC based particles to be used in batteries. These are sol-gel, solid state, combustion, spray pyrolysis, hydrothermal and coprecipitation. The characteristic structure of the powders that can be obtained may vary depending on the process.

2.3.1.1 Sol-gel

The sol-gel method is one of the most common methods used in NMC production. In this method, the solution is prepared from lithium and metal alkoxides by mixing appropriate temperatures and a colloidal solution is formed over time after a series of hydrolysis reactions. This solution condenses over time and takes the form of a network-shaped gel with polymerization. Then, the drying process is carried out to obtain solid particles [77].

2.3.1.2 Solid state

It is a simple method used to synthesize particles for cathode active NMC materials, thanks to its short process steps compared to other methods. However, it is important to note that the particles for Ni, Co and Mn are previously synthesized by other processes. After mixing transition metal salts or oxides homogeneously with lithium, a calcination/sintering process is applied, and a new layered NMC structure is formed by the resettlement of metal ions through diffusion. Although this method is easy, it is less preferable due to its low efficiency [78].

2.3.1.3 Combustion

It is another simple method to produce NMC, in terms of its process structure and shortness is combustion However, the process needs high temperature and safety concerns exist for larger productions. The metal oxides to be used are mixed homogeneously with a flammable substance and ignition is carried out. The process takes place at temperatures between 100-400 ^{o}C depending on fuel type. At low temperature, the crystal nucleation mechanism dominates crystal growth, resulting in exothermic reactions. With increasing temperature, crystal growth becomes more dominant than nucleation and particles become larger and precursor powders are obtained. Afterwards, it is mixed with lithium and calcined to obtain cathode active material [79,80].

2.3.1.4 Spray pyrolysis

Spray pyrolysis is a method used in commercialized production on a macro scale due to its high production rate, but its production is limited on a laboratory scale due to the expensive equipment and difficulty of access. Spray pyrolysis involves mixing water-soluble transition metal and lithium salts in a stoichiometric ratio and passing them through a fine nozzle. The mixed solution is carried through a nozzle by ultrasonic vibrations or a carrier gas such as air, and by hitting a preheated surface up to 1000 ^{o}C, it instantly evaporates and particles are obtained by reactions, respectively, by dissolving salts [81,82].

2.3.1.5 Hydrothermal

Hydrothermal methods are facile methods used in the production of particles having high crystallinity in an aqueous environment via metal salts in a closed container using parameters such as temperature, pressure and pH. The fact that it takes place in a closed container may create disadvantages for large commercial production [83,84].

2.3.1.6 Co-precipitation

Co-precipitation is a process performed to collect composite metal hydroxides in a particle using different salt solutions. It is the most used process to produce NMC today. The main reason for this is that the morphology of the particles obtained at the end of the process is rather easy to control and particles with high tap density can be produced [85]. This method is basically a process to obtain desired particle size,

particle size distribution, surface morphology and a smooth crystal structure in a reactor with appropriate pH, temperature and mixing rate, and etc. [86].

Particles so-called precursors are obtained, starting with the controlled feeding of metal salts, a precipitating agent that helps precipitate these salts in the form of hydroxide, and a chelating agent that controls particle morphology. The precipitation environment determines the chemistry of the precursors. Among the most commonly used NMC precipitation methods are carbonate, oxalate and hydroxide co-precipitation methods. Although the hydroxide precipitation method, unlike other methods, requires an inert environment to precipitate in a basic environment and prevent impurities, it is more effective than others thanks to the ability to produce particles with higher tap density, narrow particle size distribution and low cost of the production. [70]. During precipitation with hydroxide, N_2 gas is continuously supplied to a reactor. This process eliminates air and oxygen in the reactor, minimizing the possibility of impurity formation in the precursors.. In order to provide the appropriate reaction temperature, the reactor is heated by rotating hot water from the bottom of the reactor or between the walls. The medium is mixed with impellers to aim for a homogeneous solution throughout the reactor. The latest precursors have the structure of $Ni_xMn_yC_z(OH)_2$ (x+y+z=1).

In order to obtain a proper crystal structure for co-precipitation, metal salts should have as close solubilities in solution as possible. The metal salt with lower solubility will cause supersaturation and affect the particle structure to be formed, and its electrochemical properties [87-88].

In the co-precipitation process, the first nucleation starts and nuclei form grow to form primary particles, and their aggregation creates secondary particles .

$$TM^{2+}(aq) + nNH_3 \rightarrow [TM(NH_3)_n]^{2+}(aq) \quad (2.4)$$

$$[TM(NH_3)_n]^{2+}(aq) + 2OH^- \leftrightarrow TM(OH)_2(s) + nNH_3 \quad (2.5)$$

$$General\ reaction: \quad TM^{2+} + 2OH^- \leftrightarrow TM(OH)_2 \quad (2.6)$$

For nucleation to occur, the system, namely the solution, must be in a supersaturated state. After the supersaturated state is achieved, a nucleus must first be formed in order for a solid to form from the solution [89]. The formation of the nucleus is related to the free energy changes in the solution. Depending on the free energy in the solution,

ΔG must be negative for nucleus formation. The equation for the nucleus formation of the solution ΔG is given in Equation 2.7. [92].

$$\Delta G = \Delta G_{bulk} + \Delta G_{interface} + \Delta G_{others} \quad (2.7)$$

ΔG_{bulk} is the free energy difference related to the volume in the solution, $\Delta G_{interface}$ is related to the energy change of the interfaces in the solution and ΔG_{others} is related to the free energy of the other components in the solution [90]. In order for ΔG to be negative, the solution must be in a supersaturation state and in this case, the bulk contribution (ΔG_{bulk}) related to solids is always negative. In contrast, the ΔG interface is always positive. ΔG_{bulk} and $\Delta G_{interface}$ energies may change depending on the shape of the particles to be formed. For the formation of the first nucleus, the most suitable for ΔG_{bulk} and $\Delta G_{interface}$ is that the particle is close to spherical due to the surface area and volume ratio. If the particle shape is spherical, ΔG_{bulk} will be $4\pi r^3/3$, while $\Delta G_{interface}$ will be $4\pi r^2$ [91]. The r* to be formed indicates the critical radius of nucleation. The relation between critical radius of nucleation and free energies is shown in Figure 2.12.

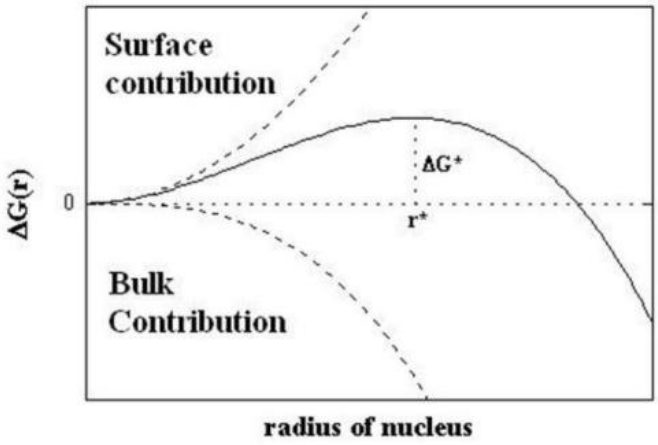

Figure 2.12 : Relation between critical radius of nucleation and free energies [91].

In the co-precipitation system, some of the TM ions that first enter the solution tend to form $TM(OH)_2$ due to the Le Chatelier Principle originating from the high free OH- ion in the solution (Equation 2.6). The remaining free TM ions react with the chelate and form $[TM(NH_3)_n]^{2+}$ complexes (Equation 2.4). The supersaturation state that occurs initially due to the decreasing TM ions in the medium decreases and Equation 2.6 slows down. Due to the high saturation at the beginning, the first nucleus formation occurs rapidly. Concentration – time relationship in precipitation is given in Figure 2.13.

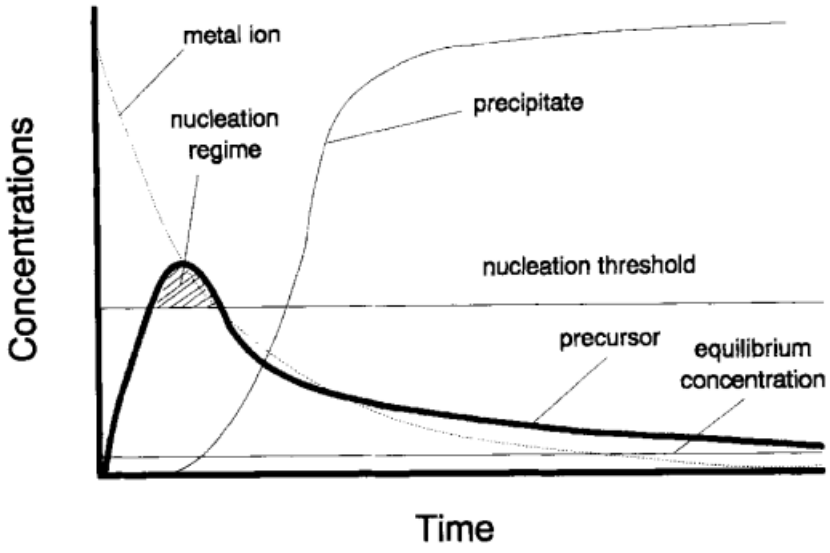

Figure 2.13 : Concentration – time relationship in precipitation [91].

The first nuclei formed are single crystals. During growth, multiple single crystals can aggregate to form larger structures. These small nuclei tend to grow in size to reduce their total energy [92]. On the other hand, during mixing of the reactor, small particles experience what is called Brownian motion, where particles collide randomly and stick together. As particle size increases, laminar flow within the reactor becomes more effective [93].

Apart from this effect, the surface charge of the precipitated particles can cause the surfaces of the precipitates to be positive or negative depending on the pH condition. In the co-precipitation together with OH-, the particle surfaces become negative. The ammonia complex, which retains the TM ions, is attracted by the unsaturated metal hydroxyl crystals and releases the TM ions to be predominant on the surface with high surface energy (Equation 2.5). This process is called surface adsorption and is the general mechanism of particle growth during co-precipitation [94]. Anisotropic growth occurs due to the difference in surface energies of the crystals. These polycrystalline structures can also be called primary particles. Afterwards, the primary particles combine and aggregate (Figure 2.14 a). These aggregated primary particles are called secondary particles. While the secondary particles continue to grow and agglomerate with the primary particles, they begin to take the form of spheres in order to reduce their total energy (Figure 2.14 b). Particle growth may also proceed by a phenomenon called Ostwald Ripening. Ostwald ripening is the dissolution of small particles in solution and their consumption by larger particles to reduce the surface-

volume ratio [95]. For a softer surface, dissolution and recrystallization occur and are related to the Kelvin Equation. While the convex surfaces on the surface tend to dissolve, the part where the particles interact with each other is concave (pL < 0), the solubility of these regions is low and the dissolved particles accumulate on this surface and recrystallize (Figure 2.14 c). In addition, the interfacial tension between the particles and the solution can be reduced by the chelator agents. Chelator agents are effective in developing a smoother surface [96].

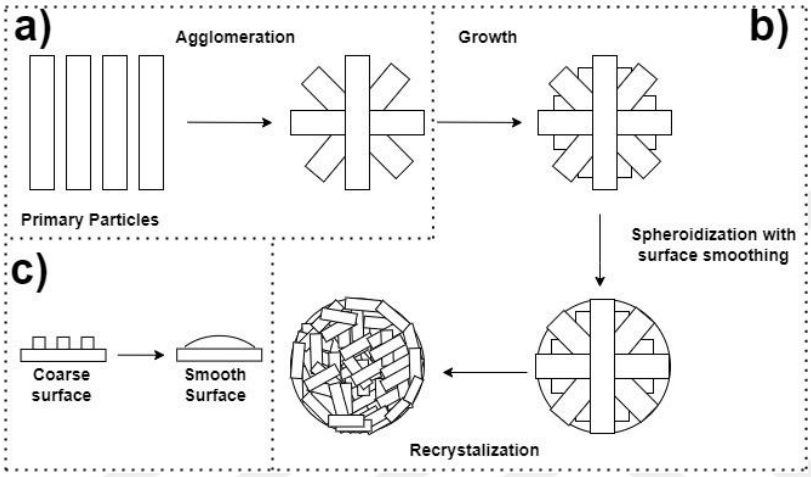

Figure 2.14 : Precursor development during coprecipitation a) primary particle agglomeration b) secondary particle formation c) dissolution and recrystallization of sharp surfaces.

In NMC precursor perspectives, Feng et al. [98] took samples from the $Ni_{1/3}Mn_{1/3}Co_{1/3}(OH)_2$ precursor produced by the co-precipitation process during different precipitation stages and performed XRD analysis. When the peak area-time graph was examined, it was seen that the slope of the (101) plane was the largest among the (100), (101) and (102) planes. Yang et al. [97] examined the time-dependent single crystal dimensions of the $Ni_{1/3}Mn_{1/3}Co_{1/3}(OH)_2$ precursor in a similar study. As a result of the study, the slope of the (101) plane was obtained the largest in a similar way. They also calculated the surface energies of the planes by DFT study (Figure 2.15). The results showed that the surface energy of the (101) plane was the lowest. This causes the NMC precursor to grow anisotropically in the fastest (001) direction. In addition, the electronegativity value of each surface in the crystal is different. Surfaces with high electronegativity values will be more willing to attract positively charged ions. This supports anisotropic growth in a certain direction due to the different electronegativity values on the surfaces [94]. In NMC structures, the electronegativity value of the (001) surface is the highest. This increases the probability of NH^{4+} ions

being adsorbed by this surface. With the change in the chelate concentration in the environment, the (001) surface begins to play a more dominant role in the growth of the crystal and anisotropic growth in the [001] direction can be restricted. As a result, the morphology of the structure can be controlled [98]. The reason for the rod-like or needle-like morphology of NMC structures is this anisotropic growth [99].

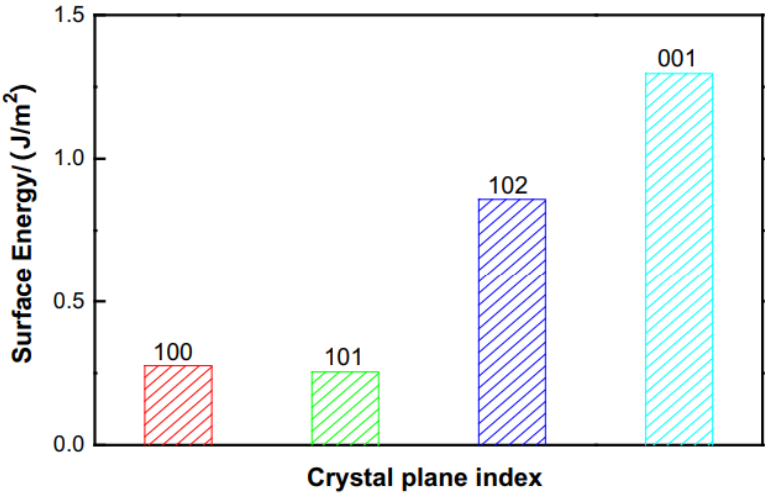

Figure 2.15 : Calculated surface energies of crystal planes [99].

These mechanisms that occur during the co-precipitation process may affect the morphology, size or particle size distribution of the precursor that will be formed by being affected by the environmental conditions.

2.3.2 Parameters affecting co-precipitation

The morphology, distribution, crystallinity and purity of the particles formed as a result of the co-precipitation process will subsequently affect their electrochemical properties. Therefore, changes to the co-precipitation environment will definitely have an impact on the precursors produced.

2.3.2.1 Chelating agent concentration

The chelating agent is one of the most important parameters in ensuring that metal ions are placed in the right spot in the structure, hexagonal ordering is formed properly and the particle surface has as smooth a structure as possible. As the chelating agent concentration increases, the amount of chelate in the precipitation reactor is expected to increase. As the amount of chelate increases, there is more NH_3 in the solution and therefore more metal ion ammonia complexes are formed according to Equation 2.4. Additionally, it is possible that the equation will shift to the left as the amount of NH_3

ions on the right side of the 2nd balance equation increases. This causes $[TM(NH_3)_n]^{2+}$ to be more dominant than $TM(OH)_2$ in the structure. The fact that the particle growth rate is more dominant than the nucleation rate triggers particle growth, while the supersaturation of metal ions decreases in this way. In cases of extremely rapid particle size growth, agglomeration occurs when the particles do not have enough time to form the desired morphology. On the contrary, when the amount of chelator is low, the decrease in the molarity of the fed chelator causes the presence of less NH_3^+ in the environment and therefore creates a high OH^- ion supersaturation state, causing the particles to precipitate. Due to the excess OH^- in the environment, TMOH oxidizes once again in solution, forming the $TMOOH^-$ complex. It can be explained by the fact that many negatively charged particles in the environment will constantly repel each other and the nucleation rate dominates the particle growth rate, and the particles cannot grow and collapse as colloids. For an ideal morphology during co-precipitation, the balance Equation 2.5, which includes NH_3^+ and OH^- ions, is very sensitive. When this balance is achieved, the different precipitation rates of Ni, Mn and Co are tolerated and the metal ions form a regular hexagonal structure and their crystallization increases. Figure 2.16 shows the $Ni_{0.8}Co_{0.1}Mn_{0.1}(OH)_2$ precursors obtained by Ding et al. [101] precursors usuing different chelating agent concentrations.

As the chelating agent concentration increased up to 4 M, it was observed that the spherical structure increased and the surface of the primary particles improved, but at higher values, the spherical structure deteriorated and caused agglomeration. On the other hand, it was observed that a colloid structure was formed at a molarity of 1 and below.

In the co-precipitation synthesis of $Ni_{0.8}Co_{0.1}Mn_{0.1}(OH)_2$ precursors produced through studies in the literature, Park et al [102], Bizotto et al, [103], Skvortsova et al [104], Lipson et al. [105], Amine et al. [106]. obtained spherical particles in the range of 1-5M of NH_4OH , it can be said that it is not the only parameter affecting the spherical morphology.

In NMC811 co-precipitation synthesis at different chelating agent concentrations, Zhu et al. [107] have seen an increase in tap density up to 1.35, reaching 1.95 $g.cm^{-3}$ with increasing molarity and then a decrease has been observed. At the concentration of 0.97 $mol.L^{-1}$, the lowest cation mixture was obtained, 3.944%.

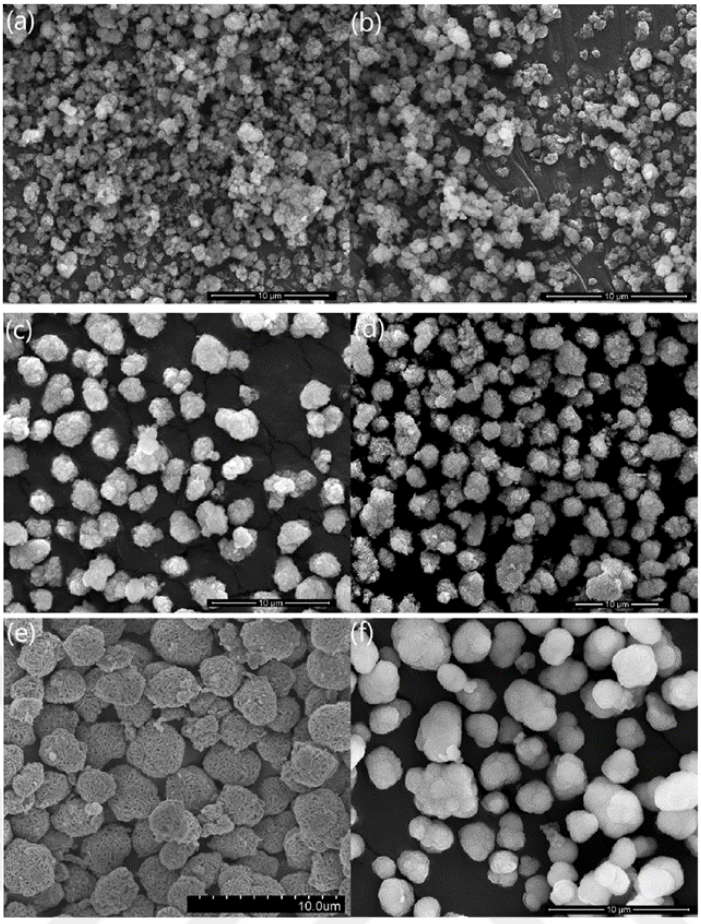

Figure 2.16 : SEM images of $Ni_{0.8}Co_{0.1}Mn_{0.1}(OH)_2$ precursors at different $NH_3.H_2O$ concentrations (a) 0.5 M (b) 1 M (c) 2M (d) 3M (e) 4M (f) 5M (ph = 11.2, 50 ^oC, TM molarity = 2) [101].

Apart from the concentration of the chelating agent, its chemistry is also a factor that will affect the co-precipitation kinetics. There are also different chelation agents other than the commonly used ammonia. The general reactions' (Equation 2.6) forward reaction rate of $M^{2+}_{(aq)}$ ions with $OH^-_{(aq)}$ ions during co-precipitation is k_f and the reverse reaction rate is k_r, and the ratio of these forward and reverse reactions can be expressed as K (Equation 2.8).

$$K = k_f / k_r \tag{2.8}$$

The overall reaction coefficient of co-precipitation can be expressed as Q (Equation 2.9).

$$Q = \frac{1}{[M^{2+}]\,[OH^-]^2} \tag{2.9}$$

This equation can be related to the general metal concentration ratio of the free metal ions in the medium and to the pH due to the relationship between OH^- and pOH. The Q/K ratio reveals the characteristics of the co-precipitation reaction. If the Q/K ratio is

less than 1, the system tends to co-precipitate spontaneously and the tendency to precipitate increases as it moves away from 1. If the Q/K value is greater than 1, the system is in the no supersaturated state and inhomogeneous, irregular particles are formed in the system. As the Q/K value approaches 1 as much as possible, the crystal growth of secondary particles with Ostwald ripening becomes ideal and desirable particle morphology and size occur [108-109].

$$Q/K = \frac{k_r}{[M^{2+}]\,[OH^-]^2\,k_f} \tag{2.10}$$

Lee et al. [112] calculate the Q/K ratio for the metal ions Ni^{2+}, Co^{2+}, and Mn^{2+} at pH = 10.75 in 1M ammonia, EDTA, citric acid, succinic acid concentrations and no chelation agent (Figure 2.17). The Q/K ratio for the ammonia Ni^{2+} ions is by far the closest to 1. While the log(Q/K) ratio is negative for the citric acid, succinic acid, and non-chelating conditions, the system tends to precipitate continuously. In contrast, the log(Q/K) value is positive in the EDTA system by 10. EDTA binds the metal ions so strongly that OH^- does not precipitate. In Ni-rich structures, the reason why it is used as the most common chelating agent in co-precipitation is that it can be carried out with less chelation compared to other chelators except EDTA. On the other hand, in a Mn-Rich structure, citric and succinic acid may be a more suitable chelating agent than ammonia. The similar situation in citric acid and succinic acid is also valid for oxalate root precipitation. In the study conducted by Hou et al. [111], since the bonding strength of the ammonia root with the Mn^{2+} ion is weak in alkaline environments, an ammonia-oxalate mixed chelator showed a better chelating property against the Mn^{2+} ion.

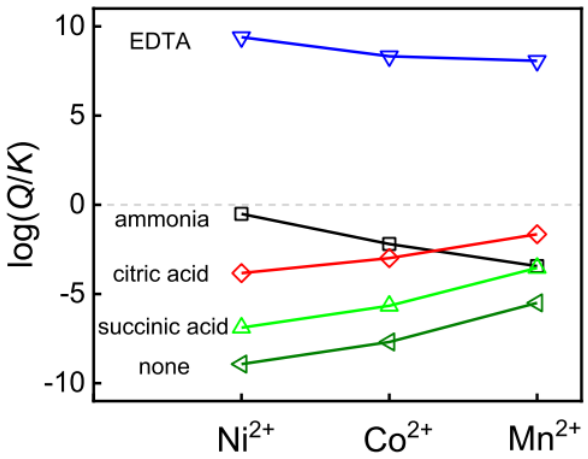

Figure 2.17 : Q/K values of a medium 1M different chelating agents and 2M Ni^{2+}, Co^{2+}, and Mn^{2+} for NMC811 at constant pH = 10.75 [110].

2.3.2.2 pH

pH is one of the vital parameters that affects the performance of the ions present in the environment during co-precipitation. In high pH environments, it is expected that there will be an excess of OH^- ions in the solution. Therefore, it affects the complexes formed by the ions in the environment and the densities of these complexes. As seen in Equation 2.5, increasing the number of OH^- ions on the left side of the equation causes the equilibrium to shift to the right. As the equilibrium shifts to the right, the nucleation rates of the particles become dominant over the particle growth rate. In this situation, the structure tends to precipitate. In cases where pH is high, the particles precipitate before they have the opportunity to correct their surface morphology and grow sufficiently, so the size of the particles produced is smaller than at lower pH [76].

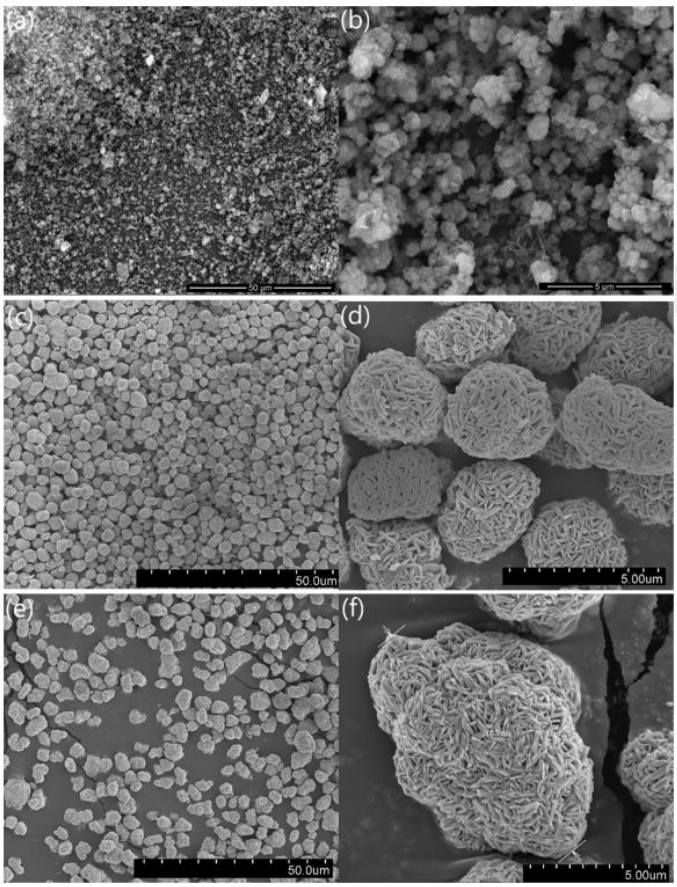

Figure 2.18 : SEM images of precursors $Ni_{0.8}Co_{0.1}Mn_{0.1}(OH)_2$ at different pH (a) (b) 12 (c) (d) 11.2 (e) (f) 10.5 [101].

The SEM images of $Ni_{0.8}Co_{0.1}Mn_{0.1}(OH)_2$ precursors produced at different pH are given in Figure 2.18 [101]. It is seen that the secondary particle size decreases significantly with increasing pH and the colloid structure forms with the negative charge of the particles due to the very high OH^- concentration at pH = 12 . It was

observed that the particle size increased as the pH decreased, but the SEM image taken at pH 11.2 showed that the spherical surface morphology was replaced by irregular polyhedrons. Additionally, increasing pH also reduces primary particle size [111].

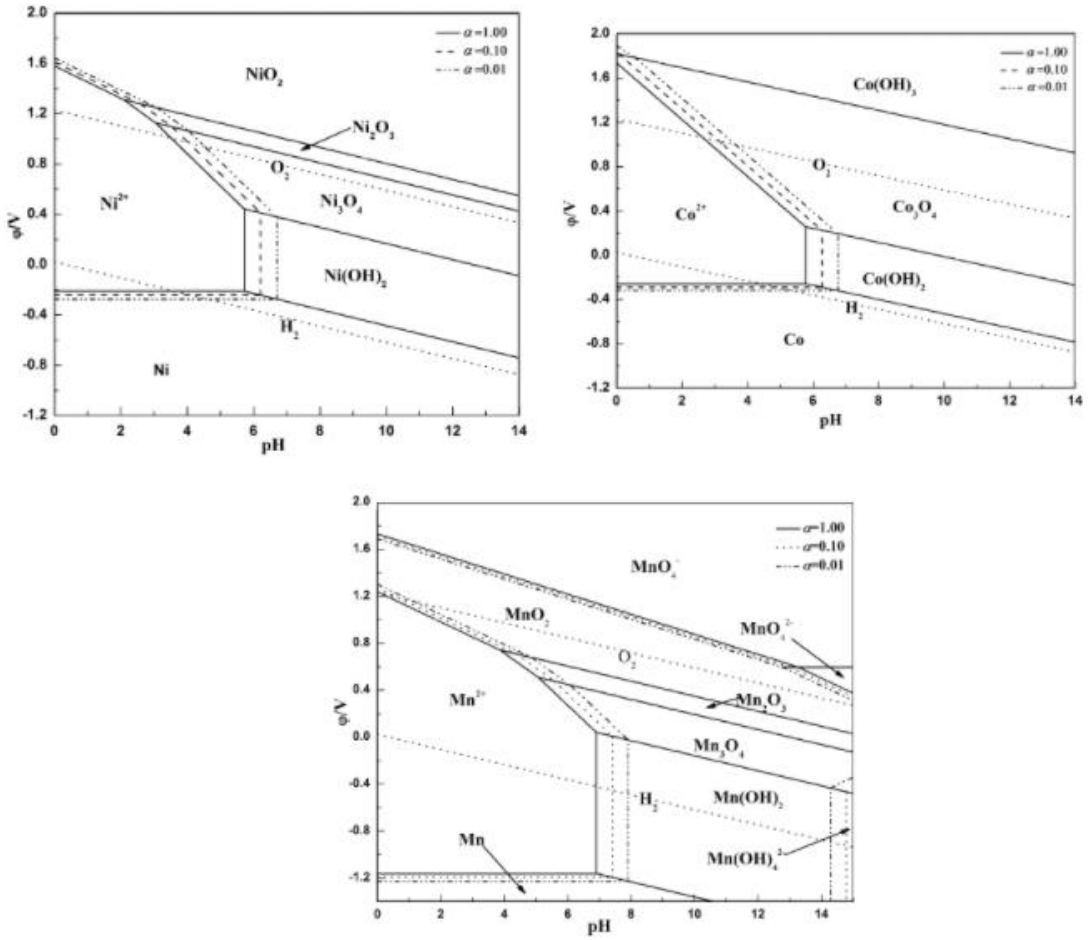

Figure 2.19 : Potential-pH diagrams of nickel, manganese and cobalt [112].

Potential-pH diagrams of nickel, manganese and cobalt are given in Figure 2.19. The area where $Mn(OH)_2$ ion actively precipitates is smaller than Ni and Mn. If the precipitation process is not carried out at the appropriate pH during the co-precipitation process, there is a high probability that undesirable oxide forms of manganese will form. This negatively affects electrochemical performance. Ammonia complexes formed by nickel manganese and cobalt ions at different pHs are given. While Ni can complex with ammonia up to pH 12, Mn and Co can only complex up to pH 10. This is consistent with the experimental results that the optimal pH value is lower for hydroxide containing lower Ni to produce high bulk density, indicating that the pH value studied should increase as the Ni content increases [113].

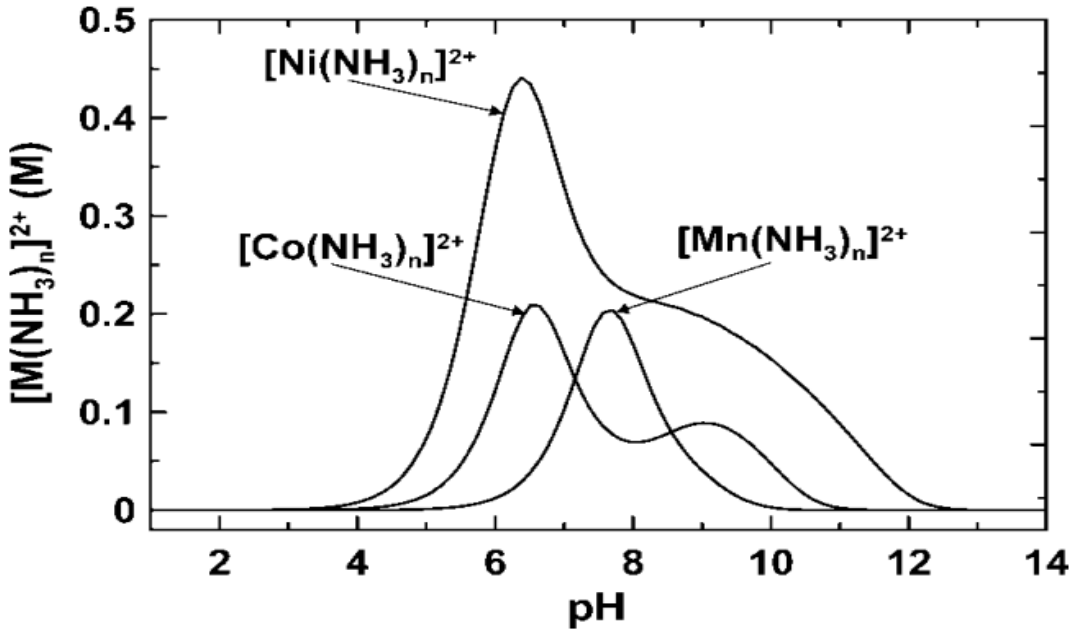

Figure 2.20 : The values of the metal-ammonia complex at different pHs [113].

It was previously stated that the Equation 2.4 is important for the sufficient growth and morphology of the particles, and the Equation 2.5 is important for the precipitation of the particles. Shen et al. [114] [$Ni_{0.6}Co_{0.2}Mn_{0.2}(OH)_2$] stated that a good particle morphology can be obtained if the ratio of metal ammonia complex concentration to OH^- concentration is 3.4. Yang et al. [97] created a figure showing the amount of ammonia that should be used for each pH. With increasing pH, a higher proportion of NH_3 ions must be used to ensure the equilibrium conditions of Equation 2.5, and a higher tap density was obtained at these values. In the light of these studies, the relationship between pH and ammonia concentration cannot be considered strange.

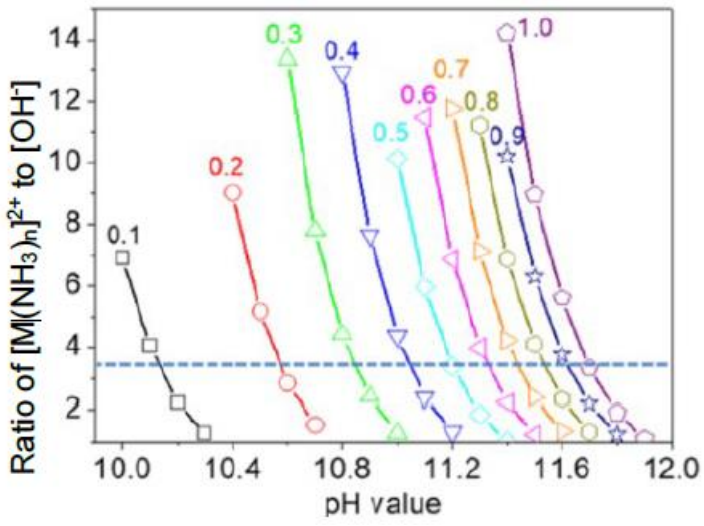

Figure 2.21 : Representation of the [OH^-] ratio of the metal ammonia complex on the pH and NH_3 map [97].

2.3.2.3 Reactor temperature

In co-precipitation reactions, after the precipitation of metal ions, the recrystallization phase, the regulation of the surface morphology of the particles, and the energy needed for the growth of the particles are met by heating the system. While high temperatures provide sufficient energy, increase the reaction rate and crystallinity, they can also cause the formation of undesirable phases [115]. These undesirable phases cause the material to give low electrochemical performance [115]. In the literature, it has been observed that in manganese-containing systems, as the possibility of manganese oxidation increases above 60°C, undesirable manganese hydroxide phases such as MnOH ve Mn_3O_4, MnOOH, $MnO(OH)_2$ are formed [116-129]. SEM images of $Ni_{0.8}Co_{0.1}Mn_{0.1}(OH)_2$ precursors produced by Vu and Lee [116] at different mixing temperatures are given in Figure 2.22. At 50°C, the primary particle surface has a wider and more regular surface compared to 45°C, purity deteriorates in particles produced at temperatures higher than 50°C, and the best electrochemical results are in particles produced at 50°C.

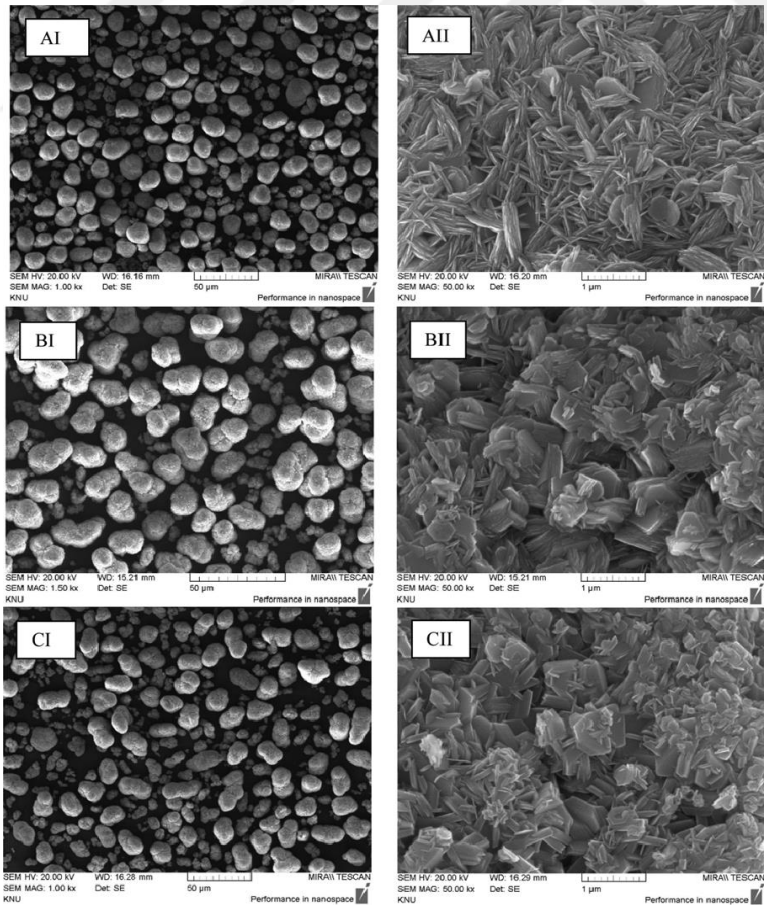

Figure 2.22 : SEM images of $Ni_{0.8}Co_{0.1}Mn_{0.1}(OH)_2$ precursors at different mixing temperatures (a) T = 45 °C (b) T = 50 °C (c) T = 55 °C [116].

The reaction temperature also affects the resulting phases. $Ni(OH)_2$ has two phases: α-$Ni(OH)_2$, which is amorphous and has poorer electrochemical properties, and β-$Ni(OH)_2$, which has higher crystallinity and is more ordered [117]. While there is a tendency to form α-$Ni(OH)_2$ from co-precipitation experiments performed below 50 degrees, the tendency to form β-$Ni(OH)_2$ is higher at higher temperatures [118]. While β-$Ni(OH)_2$ offers the best hexagonal ordering, Xu et al. [119]. It is seen that among the cathode materials with different NMC622 phases, β-Ni contains the best capacity conservation with 91.7% (Figure 2.23).

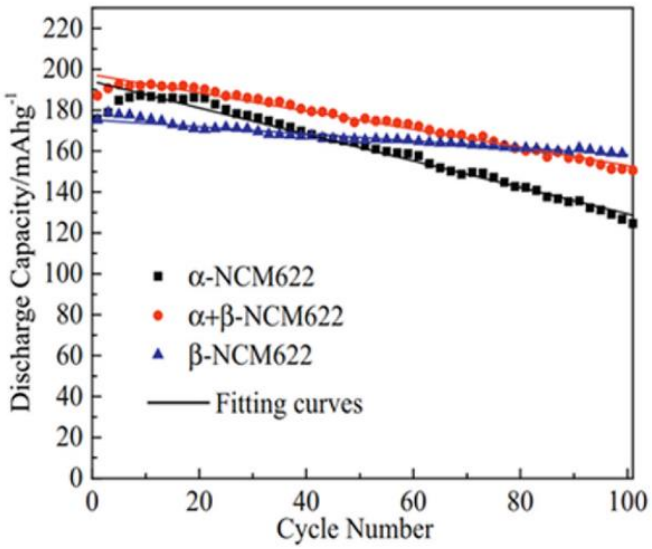

Figure 2.23 : Cycling performances of α-NMC622, β-NMC622 and α+ β-NMC622 [119].

2.3.2.4 Reactor time

Mixing time is one of the parameters that affects the morphology of the particles and therefore the electrochemical properties. Since prolonging the mixing time will provide more energy and time, it is possible for a more uniform hexagonal structure to be formed, but after a certain mixing time, it can be said that it has no effect on particle morphology or may cause negative effects. SEM images of $Ni_{0.8}Co_{0.1}Mn_{0.1}(OH)_2$ precursors (Figure 2.24) produced by Vu and Le [116] at 8, 10 and 12 hours aging times are shown. After increasing 12 hours of aging, it was observed that the size of the primary and secondary particles decreased, the particle size distribution expanded and, accordingly, the tap density decreased. According to Fakhrudin, the aging time should increase with increasing Ni content in the material [120].

2.3.2.5 Mixing

The mixing parameters inside the co-precipitation reactor affect the morphology of the size, and size distribution of particles synthesized. First of all, in order for a homogeneous structure to form, there must be homogeneous mixing inside the tank. In balance Equation 2.5, which is sensitive thanks to homogeneous mixing, it is more likely that particles with the desired properties will be formed if there is a chemically suitable environment (sufficient $NH3^{+}$ and OH^{-} ions in the environment).

The most basic mechanism affecting homogenization in the co-precipitation reactor tank is flow patterns [121]. The formation of single loops or double loops in the tank, depending on the flow pattern, will affect the properties of the particles obtained.

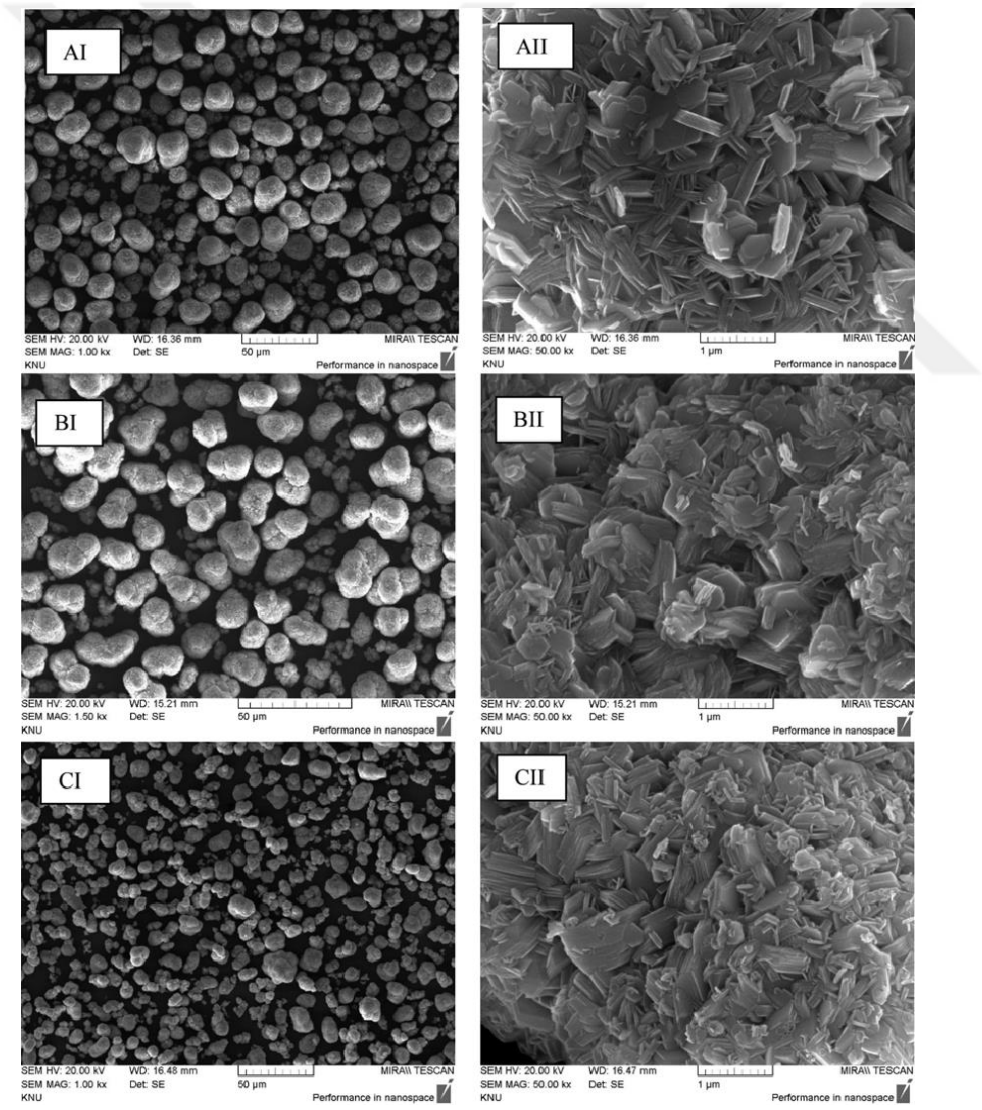

Figure 2.24 : SEM images of $Ni_{0.8}Co_{0.1}Mn_{0.1}(OH)_2$ precursors at different aging times (a) 8 hours (b) 10 hours (c) 12 hours [116].

structure, a single loop is formed throughout the reactor, in systems with double loops or more loops, there is a complex mixing system consisting of smaller loops compared to the single loop [122]. It is known that single loop is a more effective parameter in macro mixing because the concentration difference between regions will be less than in systems with multiloop [123].

Huang et al. [124] and Alpay et al. [125] produced NMC powders with different impellers and parameters and examined their morphology. In their studies, they obtained better electrochemical performance as the final product in the structures where they observed the single loop.

Another effective parameter is mixing speed. As the mixing speed increases, the number of collisions among particles and the reactor increases. Some literature studies show that at low mixing speeds, particles form a structure with agglomerated and large secondary particles that are far from spherical, while as the mixing speed increases, smaller secondary particles with a generally spherical morphology and particles with narrower particle distribution are formed. At extremely high mixing speeds (V>1200 rpm), some studies have shown that microcracks appear on the surfaces of the particles, particles of different sizes are formed, the particle size distribution widens and, accordingly, the tap density decreases [126,127].

2.4 Problems of Ni-rich NMC and Strategies to Improve The Performance of NMC Cathodes

2.4.1 Problems of Ni-rich – NMC

When Li-ion batteries were first commercialized, they consisted of a single type of transition metal atom within a layered structure. Among cathode materials with a 2-layered single atom structure, LCO batteries were the first to be commercialized. The fact that only 50% lithium ion could be withdrawn from the cathode structure during deintercalation caused the theoretical capacity of the cathode to remain at 140 mAh/g in practice, while it was around 280 mAh/g [128]. However, the heating problem at high charging rates paved the way for LMO batteries as an alternative. Although these batteries were both cheaper and provided high temperature resistance compared to LCO, the Jahn-Teller effect caused the separation of the Mn^{3+} structure into Mn^{4+} and Mn^{2+}, the change of the structure from the layered structure to the spinel structure,

limiting the rate capability, and the decrease in the stability of the cathode structure due to the reaction of Mn^{2+} with the electrolyte [129]. Despite the high capacity of LNO batteries, their tendency for cation mixing caused poor performance in capacity preservation. Afterwards, two transition metal ions, LNCO and LNMO, were tested in the layered structure [130]. Thanks to the cobalt atoms in the LNCO structure, the capacity conservation of LNO was improved, but since it is an expensive element, manganese was added instead of cobalt as an alternative and LNMO tests were carried out. LNMO, like LMO, caused irreversible reactions after the cycle and affected the electrochemical performance of the structure [131].

The first NMC experiment containing 3 different transition elements in the TM layer was reported by Liu and coworkers in 1999 [132]. In their study, they synthesized LNO, LNCO and LNMCO structures with different compositions. It was stated that when manganese was added to the $LiNi_xCo_yMn_zO_2$ structure as $0.1 \leq z \leq 0.3$ compared to the LNCO structure, no impurity was observed in the synthesized structure. When XRD analyzes were examined, it was also seen that the $LiNi_{0.7}Co_{0.2}Mn_{0.1}O_2$ structure produced for the first time for z=0.1 gave good capacity and capacity retention. Ohzuku et al. [133] synthesized $LiNi_{0.33}Mn_{0.33}Co_{0.33}O_2$ by spray pyrolysis and obtained initial charge and discharge capacities of 165 mAh/g and 150 mAh/g, respectively, in the range of 2.7-4.2V at 30 ^oC. In addition, in the cycle tests performed at 30 ^oC between 2.5-5V, it showed better capacity retention compared to LCO and $LNi_{0.5}Co_{0.5}O$ structures The positive results of this ternary system in terms of specific capacity, capacity preservation and rate accelerated NMC studies. The fact that Ni atoms increase specific capacity, the research trend from past to present is that the amount of Ni atoms in the structure increases, such as NMC111, NMC424, NCM523, NMC622, NMC811… Although the specific capacity increases with the increasing nickel ratio in the NMC structure, Ni-rich cathodes show some problems.

Ternary Ni-rich structures experience stability problems despite the high specific capacity and energy density they provide. These problems can be generally named as cation mixing, TM dissolution, O_2 release, phase transformations and microcracks.

The cathode structure has a certain positive charge balance. It takes the values of Ni^{2+}, Co^{3+} and Mn^{4+}. While deintercalation, i.e. Li^+ ions separated from the lithium layer during the charging of the cell, change the charge balance in the cathode, polarization occurs in the TM layer to maintain this charge balance. Ni^{2+}- Ni^{3+} occurs at 3.6V, Ni^{3+}-

Ni^{4+} at 4.15V and Co^{3+}- Co^{4+} at 4.3V . In the DFT study of Liang et. al. [134] have examined the TM-TM bond strengths, it was calculated that in the NMC structures with a lower ratio of Ni-rich and nickel, the energy of the bond made by Ni^{3+}, which is largely contained in the Ni-rich (x>0.8) structures, with between Ni^{3+} and Mn^{4+} has weaker bond energies than between Ni^{2+} with Mn^{4+} and Co^{3+}-Mn^{4+} in the structure in the NMC cathode with a lower ratio of nickel. This shows that Ni-rich NMC cathodes may be weaker in maintaining their structural stability . Due to these weak bonds, Ni^{2+} atoms in Ni-rich cathodes are more likely to migrate from the TM layer to the lithium layer by separating the gaps formed by Li^+ ions separated from the structure in the lithium layer during deintercalation, increasing the cation mixing and causing capacity loss due to the difficulty in diffusion of Li^+ ions [135]. In Table 2.3, Noh. et al. [64] have studied NMC cathodes containing different amounts of nickel ($Ni_xMn_yCo_z$; $0.33 \leq x \leq 0.85$) and as it is seen that the I(003)/I(004) ratio decreases with increasing Ni ion in the structure (Table 2.3). While I(003)/I(004)>1.2 indicates a low cation mixture, an increase in this ratio indicates a decrease in cation mixing.

Table 2.3 : Intensity ratio I(003)/I(004) of the different Ni content NMC structures [65].

	$I_{(003)}/I_{(104)}$
$Li[Ni_{1/3}Co_{1/3}Mn_{1/3}]O_2$	1.35
$Li[Ni_{0.5}Co_{0.2}Mn_{0.3}]O_2$	1.32
$Li[Ni_{0.6}Co_{0.2}Mn_{0.2}]O_2$	1.26
$Li[Ni_{0.7}Co_{0.15}Mn_{0.15}]O_2$	1.20
$Li[Ni_{0.8}Co_{0.1}Mn_{0.1}]O_2$	1.19
$Li[Ni_{0.85}Co_{0.075}Mn_{0.075}]O_2$	1.18

During intercalation and deintercalation of layered structures, expansions and contractions occur in lattice parameters. Figure 2.25 shows the change of a and c parameters during deintercalation of a Ni-rich structure. During deintercalation, a continuous contraction is observed in the a direction due to Li^+ ions separated from the structure. On the other hand, while the c parameter narrows until the Li^+ concentration in the cathode structure decreases to 0.8, the contraction in the lithium layer brings the oxygen atoms closer to each other and the oxygen atoms, which tend to repel each other, cause the monoclinic phase transformation, which is more stable than the hexagonal structure. Due to the monoclinic phase transformation, there is an expansion

in the c direction and it continues until the Li^+ concentration reaches 0.4. Then, the monoclinic hexagonal 2 (H2) phase transformation begins. However, the contraction begins again in the c direction. When the Li^+ concentration is 0.25, the 3rd Hexagonal structure (H3) begins to form. With this phase transformation, the contraction of the structure in the c direction intensifies. Large stresses occur in the layered structure [135-136].

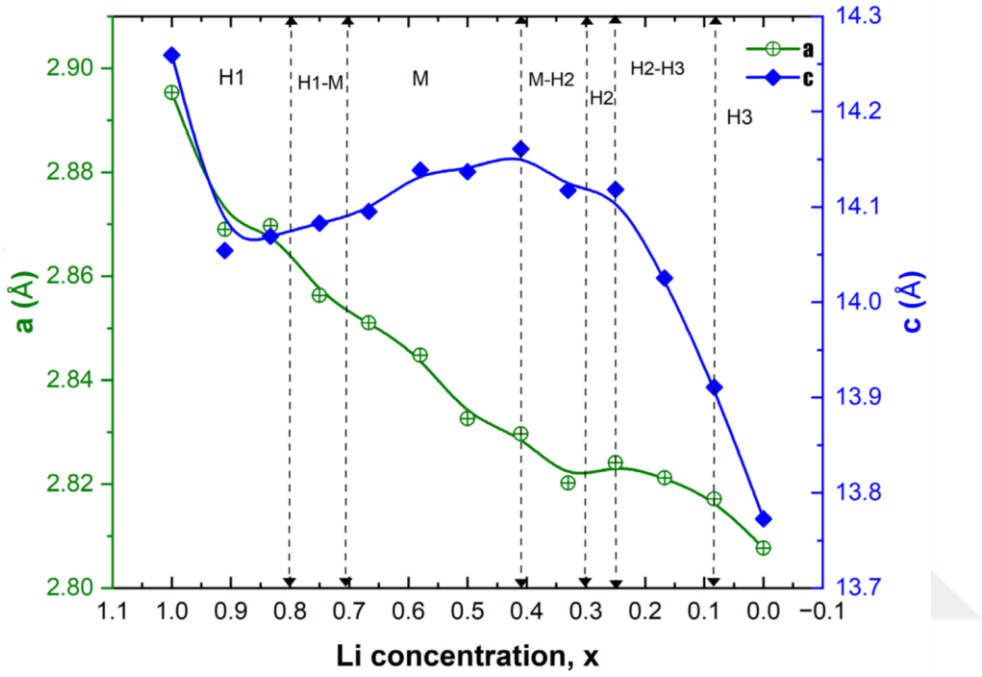

Figure 2.25 : Ni-rich structure changing of a and c parameters during deintercalation [135].

In Ni-rich cathode materials, polarization of nickel atoms occurs in the structure during deintercalation. Ni atoms interact with 6 oxygens in the hexagonal structure and show the NiO_6 octahedral structure. Ni^{2+} and Ni^{4+} have a structure that has a Ni atom in the center and the bond lengths in the 6 oxygen interactions are close to each other [137]. Ni^{3+} structure is subject to a distortion (Jahn-Teller distortion) where the bonds in the z direction (c axis) are elongated due to the geometrical incompatibility with the energy balance in the energy layers. During H2-H3 (Ni^{3+}-Ni^{4+}) polarization, these bonds are momentarily shortened in the c direction [138]. Ryu et. al. [139], graphs showing the change of a and c lattice during the H2-H3 phase transformation while charging NMC cathodes with nickel compositions ranging from 0.6 to 0.95 are given. At 4.15V, the narrowing in the c direction in the H2-H3 phase transformation was -2.6%, -3.7%, -5.6% and -6.9% for x=0.6, x=0.8, x=0.9 and x=0.95, respectively (Figure 2.26). It was observed that the narrowing in the c direction became more severe

with increasing nickel content. In addition, in the cyclic voltammetry tests, while the H2 structure and H2-H3 peak were not observed for x=0.6, it was observed that the H2-H3 peaks became sharper and more severe with increasing nickel content. Jung studied [139] a similar situation and has observed in NMC111, NMC622 and NMC811,. H2-H3 phase change peaks have not been observed in NMC structures other than NMC811 (Figure 2.27).

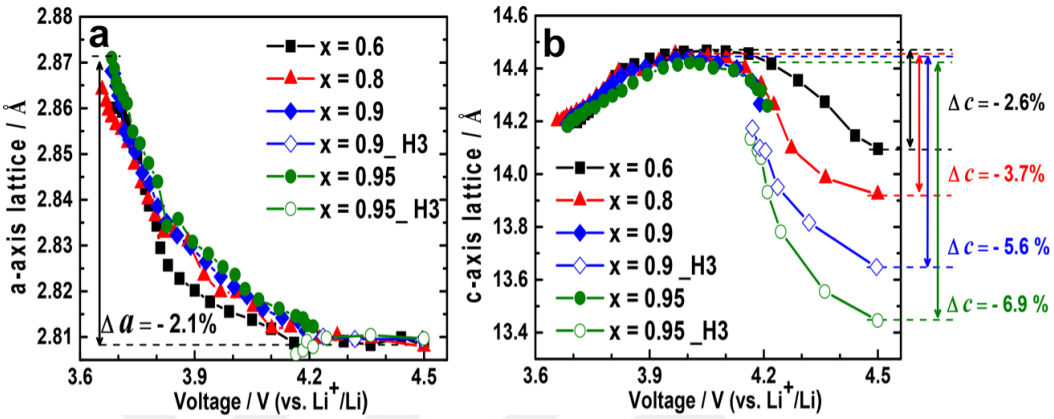

Figure 2.26 : Shrinkage rate of different of Ni-rich NMC cathodes during H2-H3 phase transformation a) a-axis b) c-axis [139].

In Ni-rich NMC structures, the Ni^{3+}/Ni^{2+} ratio is higher than in NMC structures with less nickel. The reason for this is to provide the charge neutrality of Co = 3+ and Mn = 4+. Although the higher Ni^{3+} ratio causes the Ni^{2+} ion ratio to decrease in the Ni^{2+} structure and seems to reduce the cation mixing of Ni^{2+} and Li^{+} ions with similar ionic radii, in fact the high amount of Ni atoms in the structure will provide enough Ni^{2+} ions for the cation mixing [139-110]. Moreover, during deintercalation, Ni^{4+} polarization will be more dominant in the structure. The Ni^{4+} structure is a highly reactive ion and tends to release the oxygen atom in its structure. The tendency for oxygen release in NMC materials is higher on the surface. With the release of oxygen from the surface, from the layered structure to the spinel structure and rock-salt structure. These reactions are irreversible and cause permanent capacity loss in the structure [141-142]. The formation of the rock-salt structure (Figure 2.28 b) from the layered structure (Figure 2.28 a) causes O and Li loss from the structure. The ionic conductivity of the newly formed rock-salt structure is low, and due to its anisotropic structure, Li^{+} diffusion is difficult.

$$3NiO_2 \text{ (layered)} \rightarrow Ni_3O_4 \text{ (spinel)} + 2O \quad (2.11)$$

$$Ni_3O_4 \text{ (spinel)} \rightarrow NiO \text{ (rock-salt)} + 2O \quad (2.12)$$

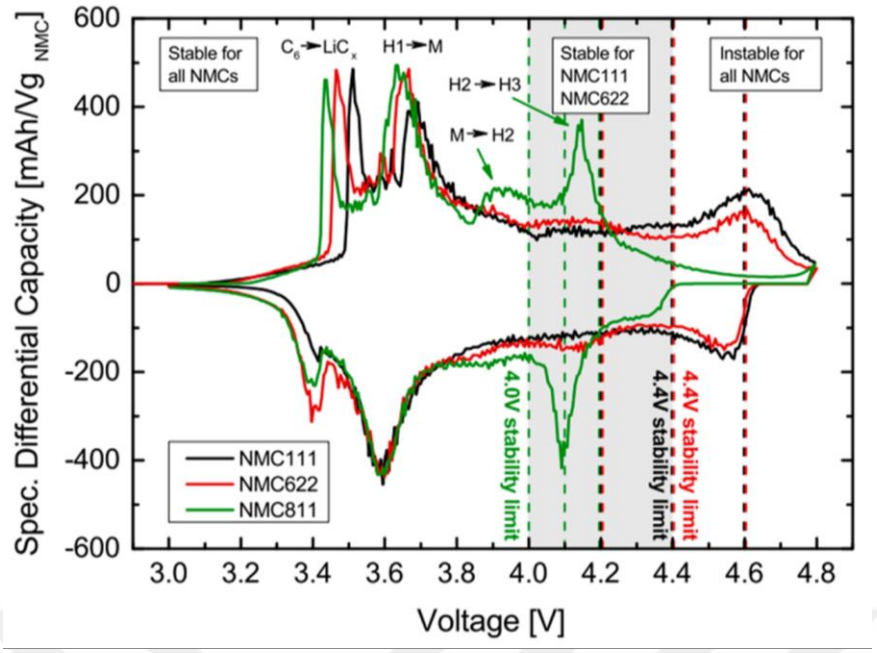

Figure 2.27 : NMC111, NMC622 and NMC811 polarization curves during delithation [139].

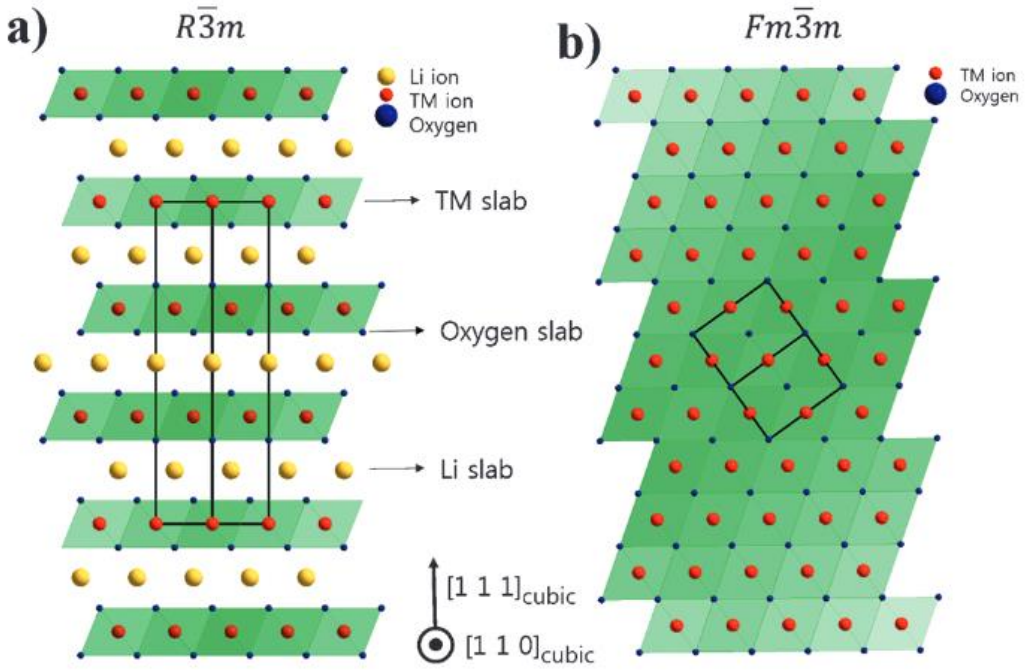

Figure 2.28 : a) Ordered and disordered layered structures a) R$\bar{3}$m structure (NMC layered) and b) Fm$\bar{3}$m structure [143].

Another problem in Ni-rich NMC cathodes is microcracks formed as a result of long cycles. It is known that the instantaneous shape changes of the lattice resulting from the H2-H3 phase transformation during continuous charge and discharge cycles due to oxygen release from the structure and the formation of the rock-salt structure, together with the anisotropic stresses on the primary particles, cause the primary particles to

separate from each other along the grain boundaries and cause microcracks [144-145] These microcracks facilitate the penetration of corrosive electrolyte from the surface and HF in the electrolyte causes the structure to corrode. Since NMC cathodes with a lower nickel content in their composition ($x \leq 0.8$) undergo less volume change in the c axis during the H2-H3 phase transformation, the formation of microcracks is restricted [139] (Figure 2.29).

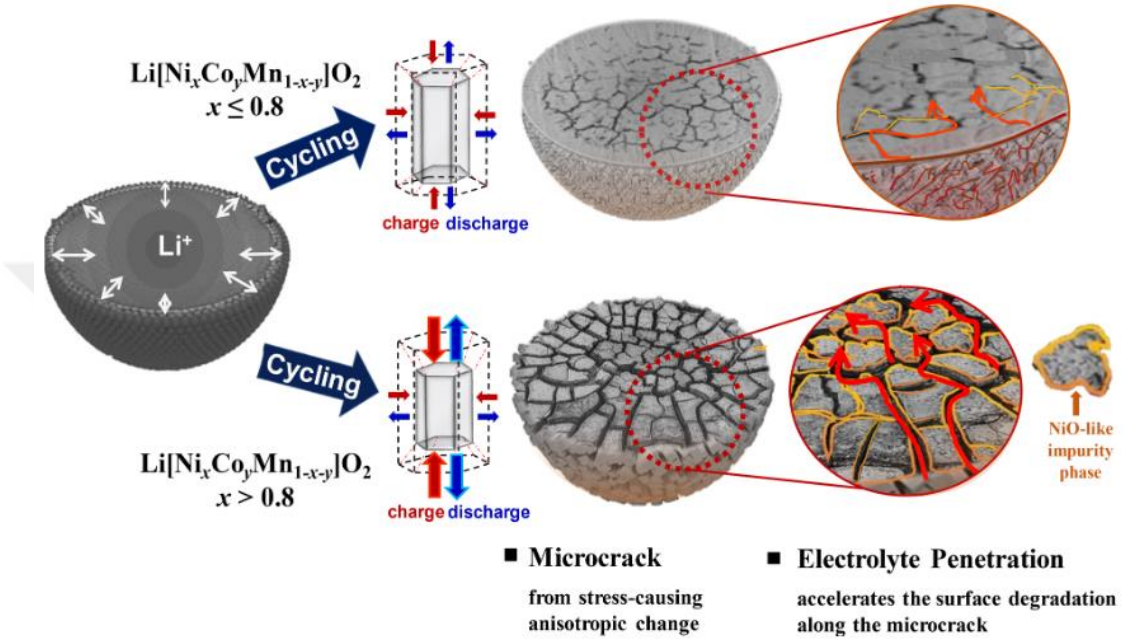

Figure 2.29 : Change in cathode microstructure as a result of long charge/discharge cycles depending on the Ni ratio in the NMC structure [139].

According to Amatucci et al. [146], the capacity loss accelerates at high voltages, especially compared to low voltages, with the partial conversion of Co^{3+} ions into Co^{4+} on the surface of $LiCoO_2$ forming the SEI structure above 4.2V, and the dissolution of TM atoms on the surface [147]. On the other hand, due to the high composition of nickel in Ni-rich cathode materials, the dissolution of Ni^{4+} ions during Ni polarization and the subsequent formation of a thicker SEI structure may cause the surface to become difficult for Li^+ diffusion and a higher Li^+ diffusion impedance to be seen [148].

Ni-rich cathodes due to the chemical instability in structure, have some problems such as formation of microcracks in the structure as a result of long cycles due to stresses occur during the H2-H3 phase transformation, formation of rock-salt structure by releasing oxygen and make difficult lithium diffusion, cathode surface corroded by electrolyte, cation mixing.

2.4.2 Strategies in designing process

2.4.2.1 Process optimizing

Since the production of cathode materials consists of successive process steps, the morphology of the cathode material can be changed and its electrochemical properties can be improved not only during the production of precursor particles but also with improvements in subsequent processes. Therefore, strategies in designing the particles are very important. Strategies could be made on materials composition, process and equipment used in the whole production of NMC cathode active materials.

Morphology and structural design can include the formation of the precursor, lithium mixing, calcination and lamination [71]. Yang et al. [149], synthesized NMC622 precursors at different pH (between 10.5-11.5) and NH_4OH concentrations (between 4-6 M) by co-precipitation method. The precursors produced at low pH and high NH_4OH concentration show higher primary particle orientation (Figure 2.30 c). With increasing pH and decreasing NH_4OH concentration, the orientation of the primary particles of the structure decreases and is completely destroyed (Figure 2.30 d,e). As a result of calcination, the surface morphology of the particle that have good orientation as precursor, is thin and long, while it shows a morphology developed in the (003) direction, while as the orientation decreases, the primary particles begin to agglomerate and a particle morphology developed in the (104) direction is obtained (Figure 2.30 a). While the layered structure developed in the (003) direction forms a structure with wider interlayer gaps for the diffusion of Li^+ ions, on the other hand a structure that is not suitable for Li^+ diffusion is observed in the layered structure developed in the (104) direction (Figure 2.30 b). When the XRD results are examined, it is seen that the I(003)/I(104) ratio decreases with the primary particle orientation decreasing and cation mixing increases. As a result of electrochemical tests, the specific capacity, rate performance and capacity retention of the sample with a better primary particle orientation increase. As a result of the impedance test, it is seen that the Rct value decreases with the better primary particle orientation. The structure gives better specific capacity, rate performance due to the lower activation energy for Li^+ ion diffusion in morphologies with good orientation. In addition, compared to agglomerated primary particles, oriented particles have less segregation between primary particles due to the controlled expansion and contraction of the crystal lattice resulting from H2-H3 phase transformations in long cycles. In less oriented structures

with agglomerated primary particles, segregation occurs, while electrochemical performance decreases due to the rock-salt structure formed more at grain boundaries [150-151].

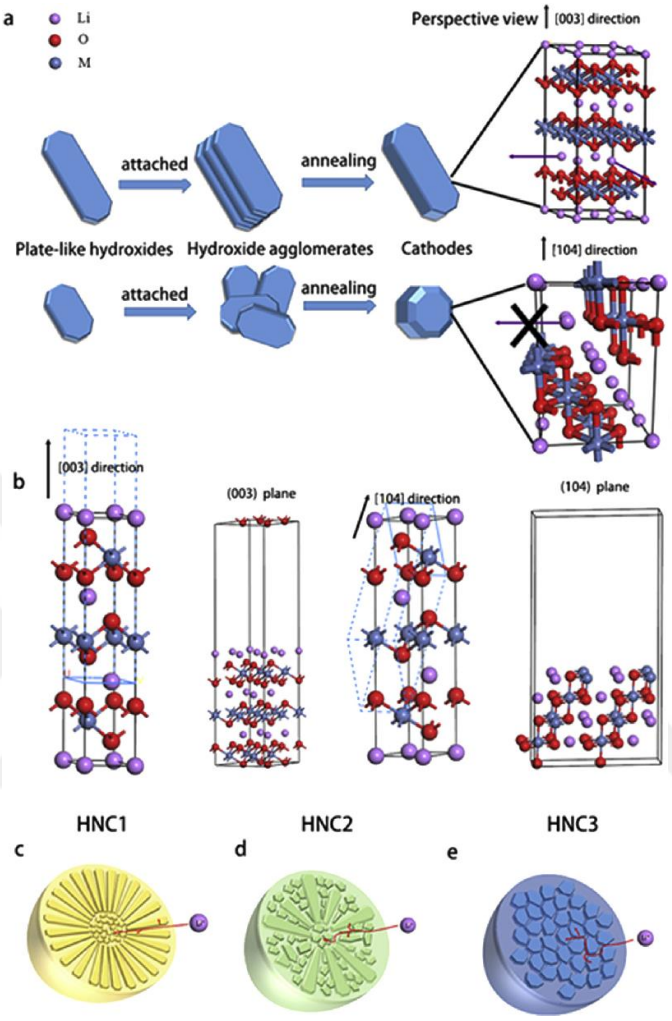

Figure 2.30 : Effect of primary particle morphology on the growth direction of the crystal structure a) (003) and b) crystal structures grown in the (104) plane direction c) Ordered primary particle d) Semi-ordered primary particle e) Disordered primary particle [149].

Calcination parameters also affect final particle morphology. Generally, Ni-rich cathode materials, Ni^{2+} tends to exchange with Li^{+} due to similar ionic radius, while O_2 atmosphere can sufficiently oxidize Ni^{2+} to Ni^{3+}, thus reducing the cation mixing in the active material. Meanwhile, O_2 atmosphere also reduces the formation of oxygen vacancies on the particle surface, resulting in a stabilized layer structure [152]. Therefore, oxygen atmosphere is usually used during the preparation of Ni-rich layered cathode materials to prevent excessive cation mixing in the structure.

Tiozzo et al [153] performs calcination for NMC811 in pure N_2, pure O_2 and pure air environments. Pure air provides the best electrochemical performance thanks to the narrow particle size distribution and less lithium loss during calcination. Kim et al. [154] performs calcination processes in environments where oxygen, nitrogen and argon gases are mixed in different proportions. It gets the best electrochemical results in calcination carried out in a 96 % O_2/4 % Ar environment. Calcination temperature and time also affects final structure. Keeping the temperature and time high may cause unwanted particle size growth and deformations, or keeping it low may cause the structure to show low crystallinity [155].

Using excess lithium source during calcination reduces the electrical conductivity of the remaining lithium residues in the structure and disrupts the energy balance on the cathode surface, thus accelerating the decomposition of the electrolyte on the cathode surface during the charge-discharge cycle [155]. Ronduda et al [156] tried different amounts of Li source during calcination in NMC622. In CV and curve tests containing excess Li, the cathode was exposed to high polarization and caused it to show worse electrochemical properties. Mobarek et. al [157] applies calcination to the Ni-rich cathode using an excess amount of different lithium sources, causing lithium residues to form on the cathode surface and decrease the cathode conductivity.

In lamination, Raju et al [158] mentioned that the cycling performance of single crystal and polycrystal NMC811 cathode materials are affected by calendering at different levels for the NMC811 sample, depending on the amount of porosity contained in the coating.

2.4.2.2 Surface coating

Surface coating process has been utilized to increase the electrochemical performance by coating the surface of the particles and to increase the resistance to loss of capacity, microcrack formation, oxygen release or electrochemical side reactions of the cathode-electrolyte interface [159]. Some of the features that the coating should have are as follows: The chemical stability of the coating should be high so that it does not react with electrolyte. With the high redox potential of the coating, it should be stable by not releasing oxygen on the surface at high voltages while the battery is operating. Coating the cathode surface to a large extent and homogeneously will optimize the

performance during lithium diffusion. Excessive thickness may make Li diffusion difficult, and thin coating may not provide the desired performance [160].

Table 2.4 : Different elements or compounds coating on NMC811.

Cathode material	Coating Material	Coating Method	Rate	Cycle	Initial Capacity (mAh/g)	Capacity Retention (%)
Ni0.8Mn0.1Co0.1	$ZnAl_2O_4$	Coprecipitation	C	100	183.2	83[159]
Ni0.8Mn0.1Co0.1	Ce	Wet coating	C	100	162.1	90[160]
Ni0.8Mn0.1Co0.1	ZrO	Wet coating	C/5	25	179.8	97[161]
Ni0.8Mn0.1Co0.1	WO_3	Wet coating	C	100	184.2	97.1[162]
Ni0.8Mn0.1Co0.1	$LiAlO_2$	Wet coating	C	100	181	93.9[163]
Ni0.8Mn0.1Co0.1	Li_2ZrO_3	Wet coating	C	100	179	98[164]
Ni0.8Mn0.1Co0.1	$Li_4Ti_5O_{12}$	Wet coating	C	100	155	85[165]
Ni0.8Mn0.1Co0.1	V_2O_5	Wet coating	2C	100	171	87.8[166]
Ni0.8Mn0.1Co0.1	MoO_3	Dry coating	C	100	182.2	94.8[167]
Ni0.8Mn0.1Co0.1	$LiInO_2$	Wet coating	C	100	186.1	92.7[168]
Ni0.8Mn0.1Co0.1	$LiYO_2$	Dry coating	C/2	100	189.4	98.4[169]
Ni0.8Mn0.1Co0.1	SnO_2	Dry coating	C	50	170.5	88.2[170]
Ni0.8Mn0.1Co0.1	SiO_2	Wet coating	C	100	181.1	92.8[171]
Ni0.8Mn0.1Co0.1	LiF	ALD	C	100	154	85[172]

2.4.2.3 Doping

The main strategy of doping is changing the composition of the cathodes. It is known that there are several chemistries available that give different performance. In the scope of this study, NMC 811 is utilized. However, with a small change in the chemistry can make a big difference.

Doping has been utilized to improve the properties of cathode active materials. Strategy in here is to add small amounts of ionic elements into the structure while preserving the main crystal structure. It basically has a few benefits such as widening the c axis to facilitate the diffusion of Li^+ ions during intercalation/deintercalation of the structure, balancing the ionic valence at the cathode, strengthening the bonds in the structure. Thus, this may lead to a reduction in cation mixing and an increase in electrochemical performances by providing a more stable structure [64]. However, it is necessary to warn that over doping may have adverse effects such as cation mixing [173-174].

Table 2.5 : Different elements doping on NMC811.

Cathode material	Doping Element	Method	Rate	Cycle	Initial Capacity (mAh/g)	Capacity Retention (%)
Ni0.8Mn0.1Co0.1	Fe	Copr.	C/2	100	192.1	93[175]
Ni0.8Mn0.1Co0.1	Ca	Calc.	C	100	188	73.1[176]
Ni0.8Mn0.1Co0.1	Al	Calc.	C/10	100	191	94.4[177]
Ni0.8Mn0.1Co0.1	Ta	Calc.	C/3	100	203	92.6[177]
Ni0.8Mn0.1Co0.1	Mg	Calc.	C/3	100	197	80.7[177]
Ni0.8Mn0.1Co0.1	Si	Calc.	C/3	100	179	81[177]
Ni0.8Mn0.1Co0.1	Zr	Calc.	C/3	100	187.1	85.3[177]
Ni0.8Mn0.1Co0.1	Mo	Calc.	C/20	-	189	- [178]
Ni0.8Mn0.1Co0.1	Ti	Calc.	C/2	100	184	92.1[179]
Ni0.8Mn0.1Co0.1	Mg	Calc.	C/5	100	206.1	97.2[179]
Ni0.8Mn0.1Co0.1	Zr	Copr.	C	100	184	85[180]
Ni0.8Mn0.1Co0.1	Nb	Calc.	C	100	181.6	94.6[181]
Ni0.8Mn0.1Co0.1	Ti	Calc.	C/3	100	188.4	73.9[182]
Ni0.8Mn0.1Co0.1	La	Calc.	C	100	192	95.2[183]
Ni0.8Mn0.1Co0.1	Nb	Calc.	C	100	173.3	96.1[184]

Zha et al [175], by doping NMC811 structure with 3% Fe by co-precipitation method, Co atoms reside in TM layer instead of structure. Fe ion is in both Fe^{2+} and Fe^{3+} states in structure, Ni atoms contain higher Ni^{3+} in structure than in undoped NMC811, indicating that Fe doping tends to decrease cation mixing. According to Rietveld results, it is seen that Fe doped NMC811 structure has lower cation mixing than undoped NMC811. As a result of C/2 cycle tests between 2.8-4.2V, undoped NMC811 and Fe-doped NMC811 reach 80% capacity after 184 and 421 cycles, respectively.

Chen et al. [176], doped NMC811 structure with 6% Ca^{2+} during calcination. Ca^{2+} doped structure reduced the cation mixture from 8.1% to 4.7%. Ca-doped NMC811 provided higher capacity at all rates except initial charge and also provided 73.1% capacity retention in the 2.5-4.5V range after 100 cycles.

Li et al. [177] Al dopes to Ni-rich structures, replacing Mn^{4+} with Al^{3+} ions, and increasing the amount of Ni^{3+} ions in the doped structure, thus decreasing the Ni^{2+}/Li^{+} cation mixing. Some dopants with high valence and strong oxygen bonds such as Ta, W, Mo may prevent the formation of rock-salt structure while reducing oxygen release

from the structure. Due to the high valences of these element-doped structures, the decrease in the Ni^{3+} to Ni^{2+} ratio resulting from charge neutrality may cause cation mixing in the structure and cause capacity loss, but thanks to the strong oxygen bonds they have, they can be tolerated by reducing O_2 release and not forming rock-salt structure[177,178]. Konishi et al. [178] contributes 4% Mo to NMC811 structure in their study. Although doped Mo increases cation mixing and gives lower initial capacity at low temperature, it is seen in the applied DSC analysis that the oxygen release of Mo-doped structure decreases especially at high temperatures compared to undoped NMC811.

In Ni-rich ternary structures, atoms such as Mg, Zn, Ti and Zr are ions with a "pillar effect" that settles on the lithium layer, increases the energy required for the migration of TMs to the Li layer, reduces the cation mixing and facilitates delithiation [177, 179-182].

Some doping elements such as La can improve the cathode interface during charge-discharge and create a more resistant surface against corrosion caused by the electrolyte. Dong et al [183] doped NMC811 structure with La^{3+} the structure doped with 3% La^{3+} at 2.8-4.3V, C/10 rate showed lower initial charge and Coulombic efficiency (203 mAh/g and 192 mAh/g) compared to the undoped structure. In contrast, the structure doped with La^{3+} showed higher capacity retention of 95.2% at 2.8-4.3V 1C 100 cycles, improving the reversibility of the undoped NMC811 structure, which showed 74.25% capacity retention. This is explained by the protective structure of the ($La_2Li_{0.5}Co_{0.5}O_4$) surface formed on the cathode surface. B, Ta, Zr, W dopants can cause the formation of small, regular primary particles that are oriented with each other by reducing the (003) surface energy. This structure prevents microcracks with a more controlled volume expansion and contraction between charge-discharge cycles. It also delays the formation of rock-salt structure [177, 184].

Doping of low-valent atoms to the structure can increase the Ni^{3+} to Ni^{2+} ratio, thus reducing the Ni^{2+}/Li^{+} cation mixing. In addition, doping of B^{3+} to the structure can prevent the mixing of Ni^{2+} ions into the Li layer by the migration of B^{3+} into the tetrahedral voids in the Li layer [185].

Kim et al. [186] doped the NC90 cathode with Al, B, Ta, W elements in their study. In the structures examined after calcination (Figure 2.31), it was seen that the primary particles of the Al-doped NC90 cathode were agglomerated and had an irregular

structure. While the boron-doped structure (003) was seen to have long primary particles that were oriented with the decrease in surface energy, particle size refinement occurred on the oriented structure in the Ta and W-doped structure. Microcrack formation was observed in the Al-doped structure as a result of long cycles. While microcrack formation was not observed in the boron structure, long primary particles caused wide gaps for the rock-salt structure. In the Ta and W-doped structures, a structure that could provide more capacity preservation was obtained with a more uniform distribution of cell voltage during H2-H3 phase transformations and less O_2 release. After 1000 cycles, the capacity retention in pouch cells was 48%, 83%, 90% and 95% in Al, B, W and Ta doped samples, respectively.

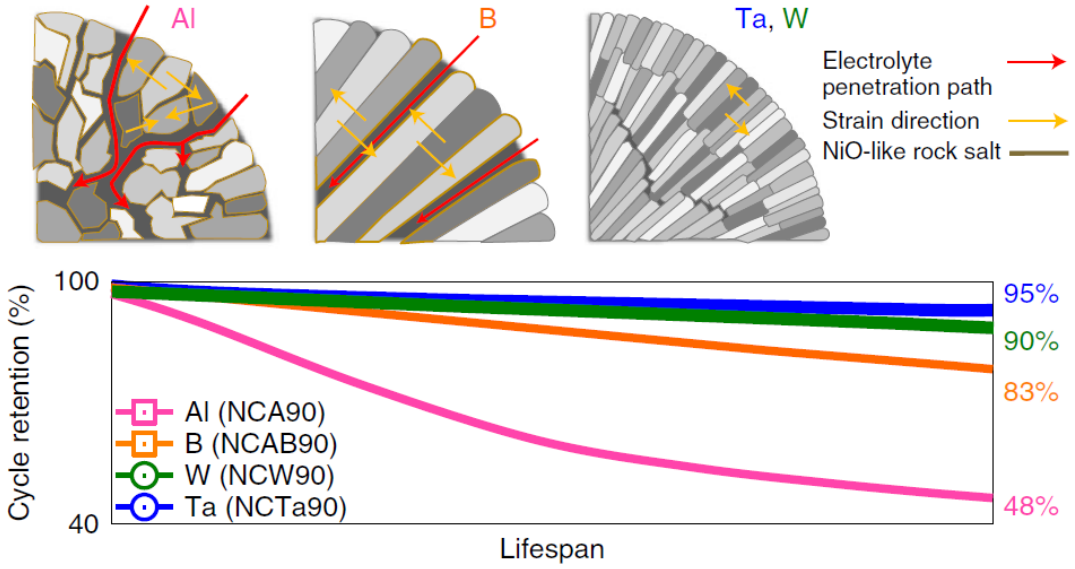

Figure 2.31 : Illustrated cross-sectional images of different doped NC90 cathode and capacity retention of their capacity retention (%) after 1000 cycle [186].

Chen et al. [136], have shown that Ti-doped NMC811 cathodes get a stable R(ct) value after 200 cycles, in the CV test at 2.7-4.5 V, 1% Ti-doped cathode provides the best H2-H3 return and as a result, its most cyclability increases.

Colalongo et al. [187] have doped NMC 811 with 0.1% Zr during co-precipitation and solid state processes. They have seen that the cation mixture decreases in cases of two doping methods. They show 85% and 82% capacity retention, in the sample produced with coprecipitation and solid state respectively, at 1 C rate.

2.4.3 Boron doping

The difference in electronegativity between transition metals (such as Ni, Mn, Co) and oxygen plays a crucial role. A larger difference generally indicates more ionic character. Generally, when the electronegativity difference is greater than 2, this bond is considered to be ionic in character, while when it is less than 1.5, it is considered to be covalent in character [188]. In NMC systems, the electronegativity values for oxygen (3.5) compared to transition metals (e.g., Ni at 1.9, Co at 1.8, Mn at 1.5) suggest that these bonds have significant ionic character due to the substantial electronegativity difference [189].

Ionic bonds can also exhibit covalent bonding properties within themselves. TM-O bonds in NMC materials often display significant covalent character due to hybridization between the transition metal d-orbitals and the oxygen p-orbitals [190]. This covalency affects the stability of the cathode structure and electrochemical performance of the cathode. During the delithiation process, the charge balance within the NMC structure constantly changes with migration Li^+ from the structure and changing in the hybridization of TM-O bonds and oxygen plays a role in charge compensation through redox processes [147].

The polarizing power of cations (the ability to disrupt the electron cloud of the anion with which it will bond) and the polarizability of anions also affect bond character. Transition metal cations, especially when highly charged, exhibit strong polarizing power, which can enhance covalent character by distorting the electron cloud of oxygen [191]. As the ionic diameter of the cation decreases and the balance value of the cation increases, polarizing power of the cation increases. On the other hand, anions with larger diameters and anions that need more electrons to form bonds (electron-rich), are more polarizable. The higher the polarizing power of the cation or the higher the polarization of the anion, the stronger the covalent bond within the ionic bond will be [192].

The electronegativity value of boron is 2.04. It shows slightly higher electronegativity than TM metals. The atomic number of boron is 5 [193]. While it has a small ion diameter compared to TM metals, its charge value being 3+ and its high valence value causing it to exhibit high polarizing power. Boron doping modifies the electronic properties of transition metal-oxygen (TM-O) bonds. The presence of boron increases the ionic character of (TM-O) bonds, thereby reducing their covalency [194]. This can

be explained as follows: Boron, which takes the value of 3^+ in the structure, reduces the charge balance in the NMC layer and increases the Ni^{2+}/Ni^{3+} ratio. Since the Ni^{2+} ion shows more ionic character than Ni^{3+}, it is expected that the Ni ion bonds will be strengthened during cycling. This is important because Ni-O shows stronger covalent bonding compared to other transition metals like Mn and Co so during delithiation, oxygen ions in structure may become unstable with formation [195]. Additionally, the B-O bonds in the structure have higher binding energy than the (TM-O) bonds (~ 809 kJ/mol for B–O, ≤ 381 kJ/mol for Ni–O, ≤ 403 kJ/mol for Mn–O, ≤ 397.4 kJ/mol for Co-O) [196] . This change in the bond character provided by boron stabilizes the oxygen releasing and helps maintain structural integrity during cycling, and preventing capacity retention [197].

With the presence of boron in the NMC structure, it is possible that the boron atom will primarily fit into the empty tetrahedral spaces in the structure due to its low ionic radius and then maybe replace the TM atoms in the structure with the increasing amount of boron. The boron atom sitting on the tetrahedral sites causes an increase in the cell volume and causes an expansion in the c direction (Figure 2.32) [198].

The presence of boron results in a smaller primary particle size, particularly in the c-direction. This event causes the primary particles of the structure to be oriented rod-like or needle-like, considering the (003) surface energy of the boron ions seated on the tetrahedral sites. This phenomenon is linked to thermodynamically reduced surface energy, as smaller particles typically exhibit lower surface energy due to a higher S/V ratio. In this way, particles oriented in a certain direction are formed [199].

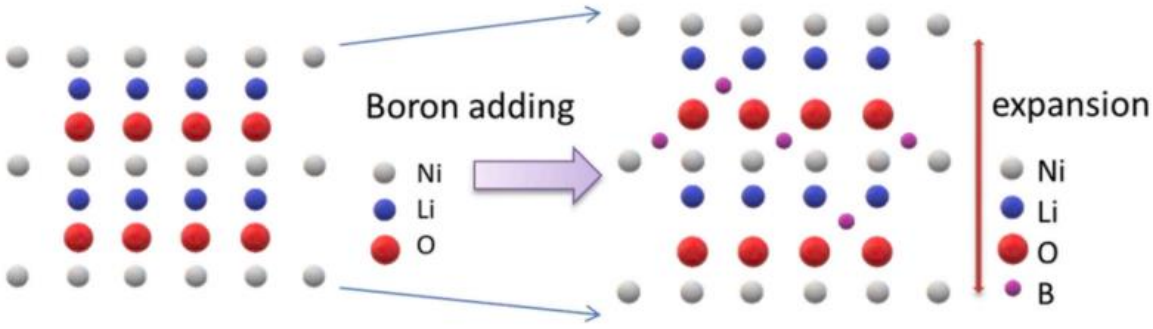

Figure 2.32 : Crystal structure after boron adding [198].

With the addition of boron to the structure, when the secondary particles are viewed cross-sectionally, it is seen that there is a primary particle structure oriented from the surface to the center in the form of a rod (Figure 2.33).

This oriented structure ensures that the high strains that will occur due to the change in the cell volume during the H2-H3 phase transformation in charge/discharge cycles are distributed properly and microcrack formation is prevented. With the decrease in O_2 release in the structure, the formation of the rock-salt structure is delayed, and with the decrease in electrolyte penetration from the surface of the structure thanks to the fine particle surface, the reactions that will occur from the electrolyte TM reaction are prevented and the deterioration of the cathode structure is delayed.

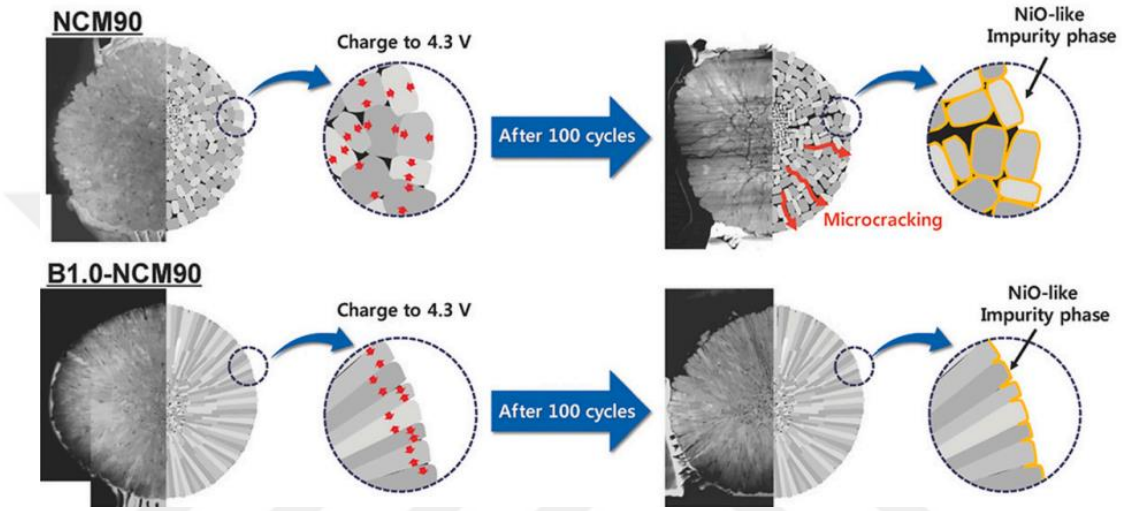

Figure 2.33 : Cross-sectional images of secondary particles during charging stress distributions [197].

In addition, it has been observed in the literature that boron-doped Ni-rich NMC structures have high Li retention after storage, show similar capacity preservation properties at high temperatures (55 ^{o}C) and minimize the increase between charge-discharge voltages as a result of cycles [200, 201].

Due to the low electronic conductivity of boron, its rate capability is limited at high rates. Co doping with other elements can be done to increase its electronic conductivity such as Mo [201].

According to Amalraj [202] in NMC structures, by-products such as Li_3BO_3, $LiBO_2$, $Li_2B_4O_7$ are obtained as a result of the heat treatment of boron with lithium. Since the by-products formed reduce the Li that will form the layered structure, capacity loss and cation mixing are observed due to lithium deficiency in the layered structure. In the study conducted by Skvortsova et al. [104], while adding boron to the NMC811 structure during heat treatment, lower cation mixing and higher capacity retention were obtained in heat treatments where high levels of Li-excess were used compared to

structures where low levels of Li-excess were used. It was also observed that lithium deficiency increased with increasing amounts of boron and these negative effects increased [104,202].

In the literature, the most common methods of boron doping in NMC Ni-rich structures are doping or coating boron during calcination. There is a lack of Ni-rich produced by boron doping with co-precipitation method in the literature and in this study, boron doping was investigated through two hypotheses. The first is to test the effect of boron element on cathode active material chemistry, morphology, structure and electrochemical properties during the production of the precursor by using boron doping during co-precipitation. The second hypothesis is to test the effect of boron element on cathode active material chemistry, morphology, structure and electrochemical properties by adding boron during calcination after the precursor is obtained. In this way, the effect of boron doping made with two separate processes on cathode active material and electrochemical properties has also been compared.

Table 2.6 : Boron doping and coating to Ni cathodes.

Cathode material	Doping Element	Method	Rate	Cycle	Initial Capacity (mAh/g)	Capacity Retention (%)
Ni0.8Mn0.1Co0.1	B	Coating	C	100	178	96 [104]
Ni0.8Mn0.1Co0.1 ($MCl_2 - NMCC_2H_4$)	B	Coprecipitation	C/2	100	179.8	97[198]
Ni0.9Mn0.05Co0.05	B	Doping	C/2	100	230	91[199]
Ni0.94Co0.06	B	Wet coating	C/3	100	226	84.1[200]
Ni0.90Co0.10	B-Mo	Doping	C	100	193,1	90[201]
Ni0.85Mn0.05Co0.1	B	Coating	C/10	100	187.1	94.2[202]
Ni0.84Mn0.06Co0.10	B	Doping	C/2	50	186.4	93.1[203]
Ni0.93Mn0.04Co0.03	B	Coating	C	150	191.1	78.5[204]
Ni0.6Mn0.2Co0.2	B	Doping	C	100	178	68.8[205]
Ni0.6Mn0.2Co0.2	B-Mg	Doping	C	100	178	84.8[205]
Ni0.6Mn0.2Co0.2	B	Doping	C	50	176.3	96.1[206]
Ni0.87Co0.09Mn0.04	B	Coating	C/2	100	193	92[207]
Ni0.83Co0.05Mn0.12	B	Doping	C/2	100	182	89.4[208]
Ni0.8Mn0.1Co0.1	B	Doping	C/2	100	197	87.4[209]

3. EXPERIMENTAL

The process flow chart of the study is given in Figure 3.1. First, the solution of undoped and boron-doped NMC811OH precursors produced in the co-precipitation process was filtered, washed and dried. Active materials were synthesized by mixing LiOH with different calcination parameters into precursors. X-ray diffraction analysis and Scanning Electron Microscope were performed for both precursors and active materials. The slurry of the produced active materials was prepared, laminated and punched electrodes produced. Then, CR2032 half cells were produced and different electrochemical tests were applied.

3.1 Co-precipitation

A specially designed 1.5 L CSTR with double impellers was used for co-precipitation. Hydroxide precipitation method was selected as the co-precipitation method, sulfates of TM materials as metal salt, NH_4OH as chelating agent and NaOH as precipitating agent. For the synthesis of undoped $Ni_{0.8}Co_{0.1}Mn_{0.1}(OH)_2$, 2M solutions in DI water were prepared containing $NiSO_4.6H_2O$, $MnSO_4.H_2O$ and $CoSO_4.7H_2O$ at 80%, 10% and 10% mol, respectively. For the co-precipitation method in which boron doped, H_3BO_3 was used as boron additive to the structure and was added to the solution containing TM solutions the B:(Ni+Mn+Co) 1:100 mol ratio. with pH 11.2-11.4 at 55 ^oC. The NH_4OH solution to be used for feeding was prepared and was fed into the continuous stirred tank reactor (CSTR) with a TM:NH_4OH ratio of 2:1 throughout the experiment. NaOH was prepared as the precipitating agent and its feeding was closed when the pH was 11.2-11.4., NaOH solution was automatically fed into the CSTR. The entire feeding system was made by peristaltic pumps. Before the feeding process started inside the CSTR system, the solution was purged with N_2 gas. The mixing speed was 800 rpm throughout the experiments in around 30 h.

After the co-precipitation process, the precursor solutions were filtered and each solution was washed. The wet precursor powders were dried in a vacuum environment at 110 ^oC overnight.

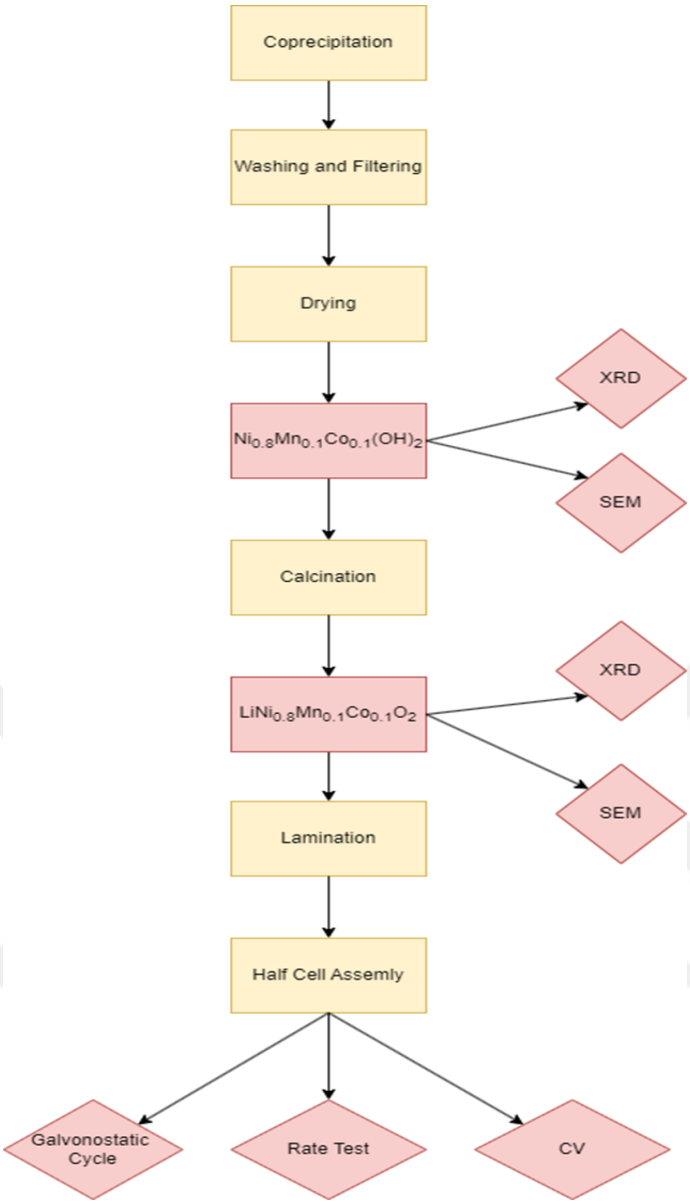

Figure 3.1 : Flowchart of experimental study.

3.2 Calcination

In Table 3.1 four different calcination processes were applied to the precursors produced by the co-precipitation method. First, the precursors were ground in an agate mortar for 10 min. Then, the precursor and 3% excess $LiOH.H_2O$ were mixed in the Thinky for 20 min at 1200 rpm. Mixed samples were placed in crucibles. Heat treatment in the air was done in the oxygen atmosphere. Heat treatment started at room temperature and increased to 450 ^oC with 2 ^oC/min heating ramp and stayed at this temperature for 4 h and then increased to 750 ^oC with 2 ^oC/min heating ramp and stayed at this temperature for 12 hours. After the heat treatment was completed, the furnaces were left to natural cooling.

Table 3.1 : Calcination parameters.

Sample	Boron Doping in co-precipitation processs (%)	LiOH:TM	H_3BO_3 (%)	1st Tem. (C)	Time (h)	2nd Tem. (C)	Time (h)	Heating Ramp (C/min.)	Atmosphere
NMC811OH-Air			-						Air
NMC811OH-Ox	-		-						
NMC811OH-OxB1		1.03	1%	450	4 h	750	12h	2 °C/min	O_2
NMC811OHB1-Ox	1%		-						

3.3 Slurry Preparation and Lamination

Slurry was prepared with an active material/carbon black/PVDF ratio of 80:10:10 using Thinky. Slurries coated on an aluminum foil using a doctor blade. After the laminated foils were dried at 70 ^{o}C for 2 h, they were rolled to 40 µm.

The electrodes were assembled as CR2032 half coin cells in a glovebox having an argon atmosphere. The CR2032 half cell structure is given in Figure 3.2.

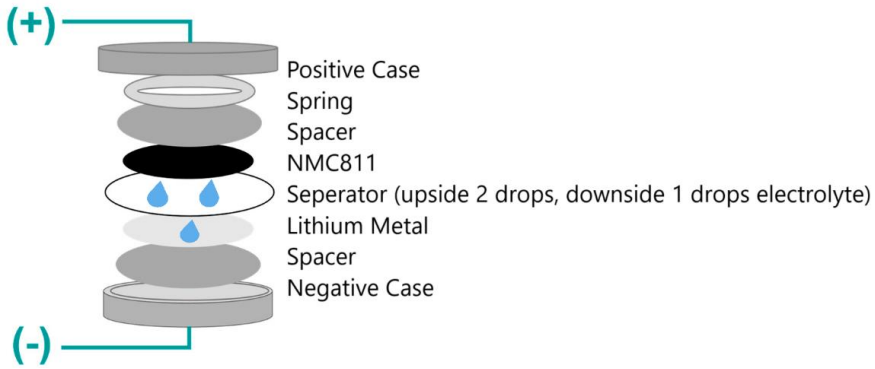

Figure 3.2 : CR2032 half cell structure.

3.4 Characterization

3.4.1 X-Ray diffraction analysis

X-Ray diffraction patterns were obtained between 0^{o}-90^{o} with a scan rate of 2^{o}/min using Cu-Kα as a source (λ = 1.54 Å). Then, Rietveld analysis was performed with 20% ZnO mixture of powders with scan rate of 1^{o}/min and analysed on TOPAS 64 software on database PDF-4+. From the XRD results, the peak positions of the powders, cation mixing, and lattice parameters were obtained.

3.4.2 Scanning electron microscopy analysis

The morphologies and particle size of powders were observed by using Zeiss Gemini 500 scanning electron microscope.

3.4.3 Electrochemical tests

3.4.3.1 Galvanostatic cycle test

Galvanostatic cycle test was performed between 2.7-4.3V on 3 cycle C/10, 100 cycle C/3 and 100 cycle C rates at 20 ^{o}C respectively.

3.4.3.2 Rate capability test

Rate capability tests were performed and rates are shown Table 3.2. The tests performed between 2.7-4.3V at 20 ºC.

Table 3.2 : Rate capability test parameters.

Rate	**C/10**	**C/5**	**C/3**	**C/5**	**C**	**C/5**	**2C**	**C/5**	**5C**	**C/10**
Cycle	5	5	5	2	5	2	5	2	5	5

3.4.3.3 Cyclic voltammetry test (CV)

Cyclic voltammetry test were performed for 4 cycles between 3-4.3V at 20 ºC with scan rate is 0.1 mV/s

4. RESULTS AND DISCUSSION

4.1 Structural, Morphological, and Compositional Analyses Results

NMC811OH (no doping in co-precipitation) and NMC811OH1B (1% B doping in co-precipitation) precursors were successfully produced by the co-precipitation method (Figure 4.1). The precursors of NMC811OH and NMC811OH1B samples obtained as a result of co-precipitation experiments are given in Figures 4.1 a-b. The secondary particle size distribution of the two precursors are 10-15 μm with a spherical shape. In Figure 4.1 c, NMC811OH-Air primary particles are composed of dense plate like morphology (Figure 4.1 a-d). However, the primary particles of NMC811OH1B have fiber like morphology instead of plates (see Figures 4.1 e-f). Boron doping in co-precipitation changed the primary particle morphology of precursors due to changing the growth plane.

SEM images of NMC811OH precursors calcined in both air and O_2 rich atmospheres are given in Figures 4.2 a-d. In Figure 4.2 a-b, NMC811OH-Air and NMC811OH-Ox have approximately around 10-15 μm size and spherical shape secondary particles. Calcination atmospheres have not made significant differences in secondary particles' spherical morphology. However, the primary particles of the precursor calcined in oxygen atmosphere (NMC811OH-Ox) are smaller, more regular and dense unlike the primary particles of the sample calcined in air (NMC811OH-Air) which are agglomerated and have larger sizes, with irregular and hollow morphology in Figure 4-2 c-d. In Ni-rich cathodes, when growth is dominated by the (003) plane, the primary particles tend to be small, thin and regular. However, when growth is dominated by the (104) plane, round and agglomerated primary particle structures are formed. Smaller and regular primary particle structures generally have shorter lithium diffusion pathways and higher charge-discharge rates [74]. In addition, calcination in oxygen deficient environments may increase cation mixing in structure leading to worse electrochemical performance [122].

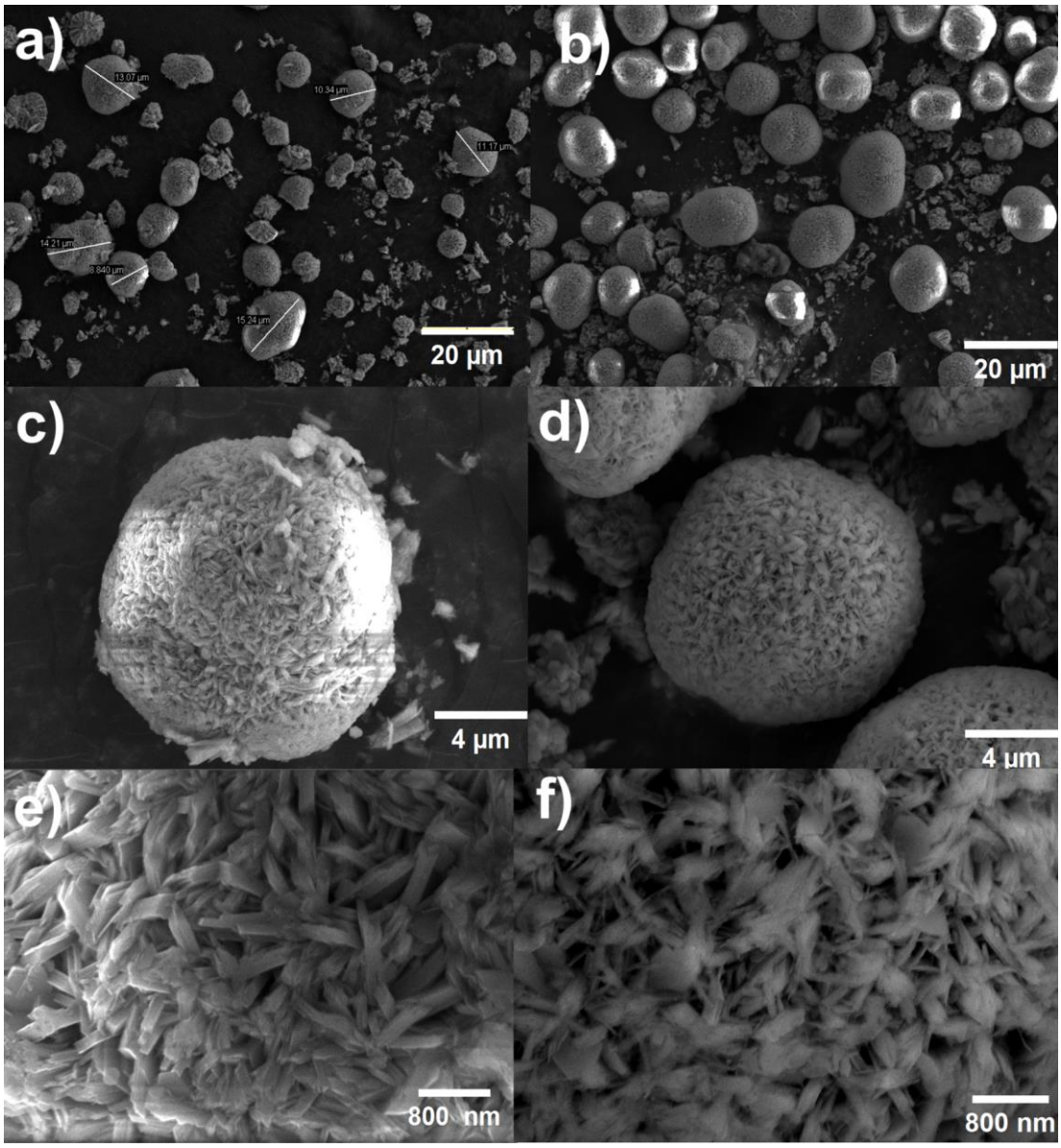

Figure 4.1 : SEM images of precursors at different magnification a) NMC811OH secondary particles, b) NMC811OHB1 boron doped secondary particles c) One NMC811OH secondary particle d) One boron doped NMC811OHB1 secondary particle e) NMC811OH primer particles f) NMC811OHB1 boron doped primer particles.

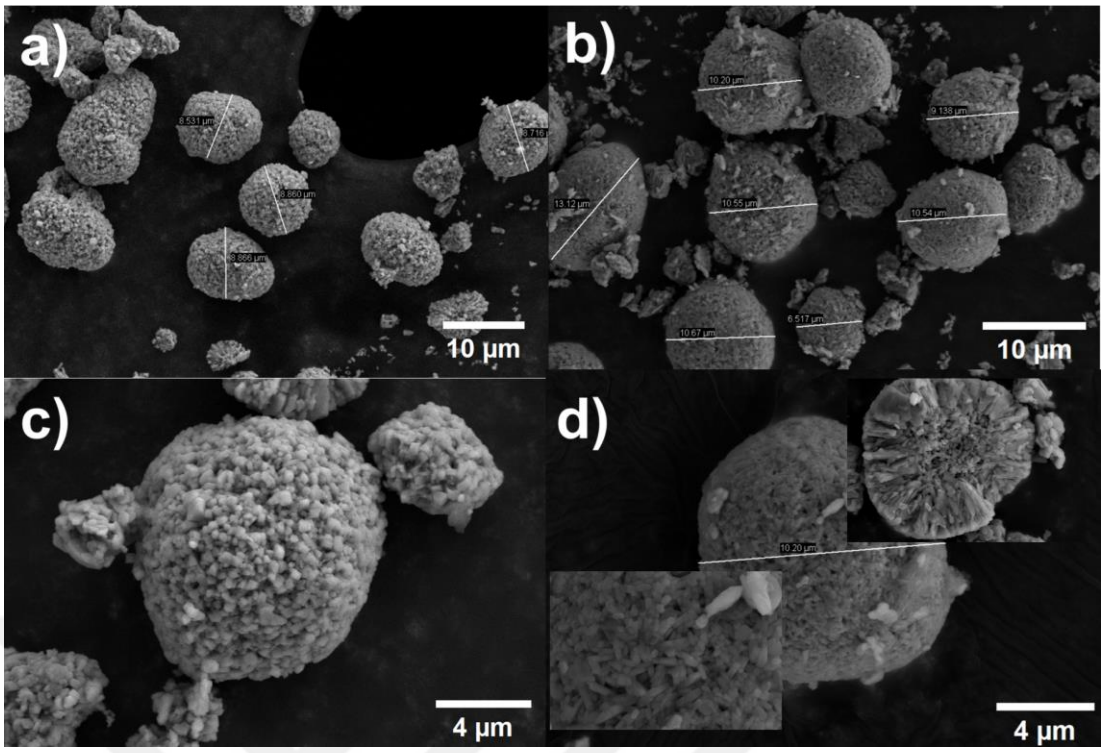

Figure 4.2 : SEM images of calcined undoped samples on different atmosphere at different magnifications a) NMC811OH-Air secondary particles, b) NMC811OH-Ox secondary particles, c) NMC811OH-Air secondary particles d) One NMC811OH-Ox secondary particle, and cross-section and primer particles.

SEM images of boron-doped samples during co- precipitation (NMC811B1-Ox) and after coprecipitation (NMC811b1OH-OxB1) and calcined in the oxygen atmosphere are given in Figures 4.3 a-f. In Figure 4.3 a-b, NMC811OHB1-Ox and NMC811OH-OxB1 have approximately around 10-15 µm size and spherical shape secondary particles. In Figure 4.3 c, there are two type of secondary particle morphology in sample NMC811OxB1. Skvortsova et. al [104] stated that reactions (4.1) and (4.2) occur simultaneously during the calcination of H_3BO_3 and $LiOH.H_2O$.

$$Ni_{0.8}Mn_{0.1}Co_{0.1}(OH)_2 + LiOH.H_20 + H_3BO_3 + O_2 \rightarrow Li[Ni_{0.8}Mn_{0.1}Co_{0.1}]_{1-x}B_xO_2 + H_2O \quad (4.1)$$

$$Ni_{0.8}Mn_{0.1}Co_{0.1}(OH)_2 + LiOH.H_20 + H_3BO_3 + O_2 \rightarrow Li[Ni_{0.8}Mn_{0.1}Co_{0.1}]O_2 + Li_3BO_3 + H_2O \quad (4.2)$$

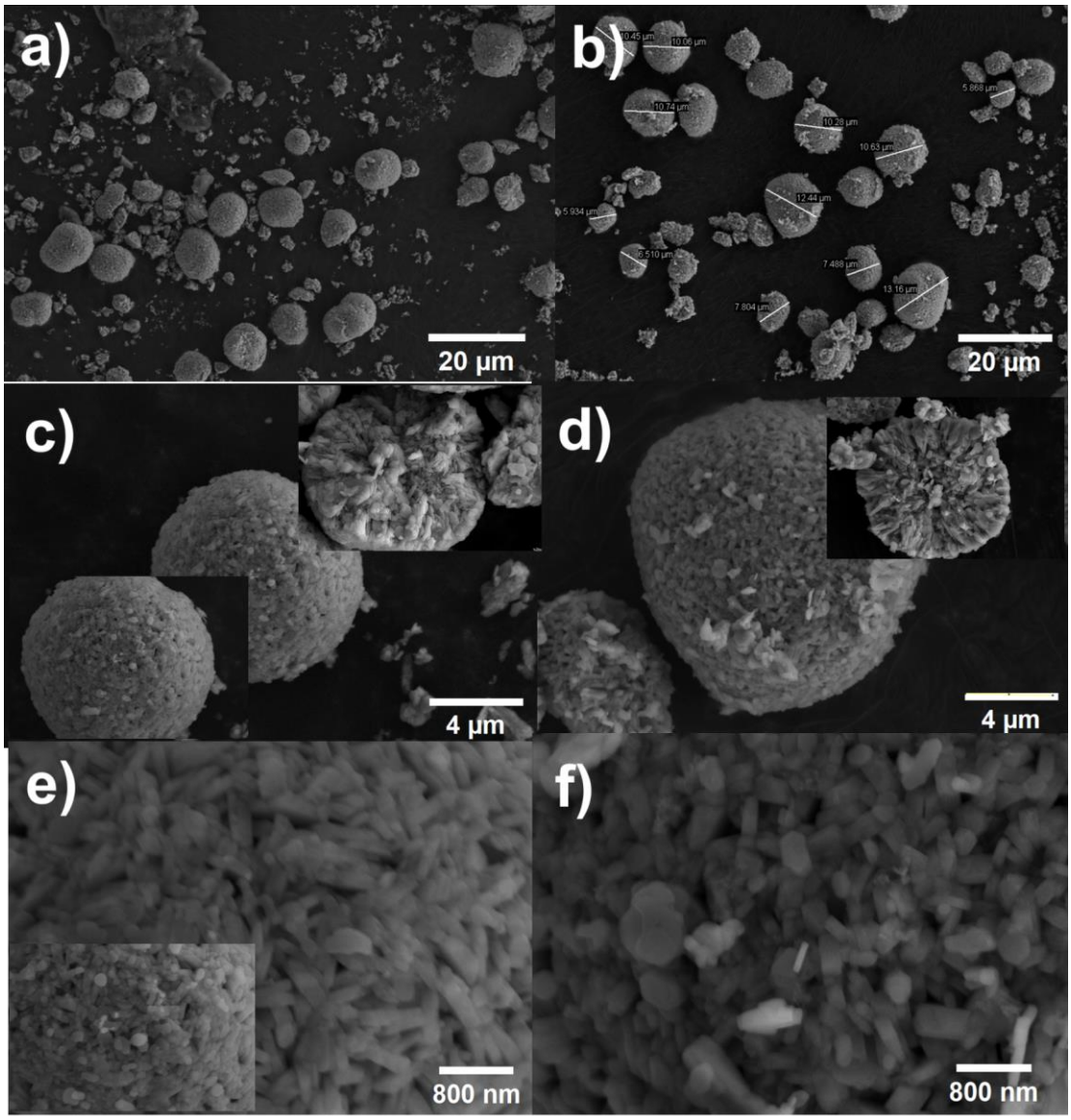

Figure 4.3 : SEM images of boron doped samples during calcination at different magnification a) NMC811OH-OxB1 secondary particles, b) NMC811OHB1-Ox secondary particles, c) Two type NMC811OH-OxB1 seconder particles and cross-section d) One NMC811OHB1-Ox seconder particle and cross-section e) NMC811OH-OxB1 two type primer particles f) NMC811OHB1-Ox primer particles.

Two types reactions may occur during boron doped in calcination; one is Equation. 4. 1 which is desired. The product of this reaction is $Li[Ni_{0.8}Mn_{0.1}Co_{0.1}]_{1-x}B_xO_2$, another one is reaction in Equation. 4.2, in which Li_3BO_3 forms. Inhomogeneous primary particle morphology is obtained. In the literature, Li_3BO_3 structure was formed on the surface in many experiments during the simultaneous calcination of LiOH and boron source [104, 202, 210]. Thin Li_3BO_3 layer increases the ionic conductivity of surface and increase capacity of the battery but increasing thickness increases charge transfer resistance and insufficient excess LiOH, the lack of lithium in the structure prevents the formation of the layered structure causing rock-salt structure. Excess LiOH using

with decreases lithium deficiency with boron doping [104]. Pre heat treatment also remove organic compounds and moisture to decrease the possibility of Li and B by-products [210].

In Figures 4.3 e, particles show different primary particle morphologies which are oriented rod and agglomerated spheres. It is expected that the electrochemical properties will be adversely affected as a result of inhomogeneous calcination. According to Park et al. [192], the rod-like primary particles seen in Figure 4.3 e are the indicators of boron doping into the structure, the energy of the (003) surface decreasing the primary particles tend to enlarge the (003) surface and form oriented rod or needle-like particle structures. In Figure 4.3 d, NMC811OHB1-Ox which is boron doped via co-precipitation sample primary particles are small and irregular (Figure 4.3 f).

NMC811OH-Ox and NMC811OHB1-Ox samples are compared, both show a spherical secondary particle structure of approximately 10-15 μm in size but NMC811OH-Ox's primary particles are a little more oriented and small (Figure. 4.2 d).

1% boron doping may not be sufficient to change the structure of the primary particles during co-precipitation. The differences between samples (NMC811OH-Ox and NMC811OHB1-Ox) could be seen in the cross-sections of secondary particles as well (see Figures 4.2 d and 4.3 d). The outer part of the cross-section surface of NMC811OH-Ox and NMC811OHB1-Ox samples partially reveals radially ordered primary particles. This ordered cross-section primarily reveals the layered structure (space group $R\bar{3}$ m). This structure provides shorter lithium diffusion paths and resilience for stresses resulting from the instantaneous large volume changes of the cell during the H2-H3 phase transformations.. It delays the formation of the rock-salt structure caused by O_2 lose. Moreover, these two particles show rock-salt structure (space group $Fm\bar{3}m$) in the center which restricts the entry and exit of Li^+ ions into the structure. This structure reduces the electronic and ionic conductivity of the cathode and causes a loss of capacity [144]. NMC811OH-Ox has smaller and more pores which affect the cycling performance positively than that of NMC811OHB1-Ox. NMC811OH-OxB1 has larger, anisometric, spherical agglomerated rock-salt primary particles along the particle cross section (see Figure 4.3 c) which results poor electrochemical performance.

XRD graphs of four calcined samples (NMC811OH-Air, NMC811OH-Ox, NMC811OH-OxB1, NMC811OHB1-Ox) are given in Figure 4.4. All peaks in graphs are sharp which means that they are highly crystalline structures. In general, peaks (003) in boron doped NMC structures shift slightly to the left [211]. The boron doped samples' XRD peaks shifted 0.02º and 0.01º in NMC811OH-OxB1 and NMC811OHB1-Ox respectively, indicating minor changes in the lattice structure. The separation of (006)/(012) peaks in all XRD graphs reveals the low cation mixing [74]. Also, the separation of (006)/(012) and (108)/(110) the layered structure is well obtained.

I(003)/I(104) ratio of NMC811OH-Air, NMC811OH-Ox, NMC811OH-OxB1, NMC811OHB1-Ox are calculated as 1.22, 1.24, 1.17 and 1.22, respectively. Since I(003)/I(104) ratio is larger than 1.2, well-ordered structures with the low cation mixing are obtained. It is important to note that the samples calcined in oxygen-rich atmospheres give lower cation mixing than those of the samples calcined in atmospheres. The lower ratio of the NMC811OHB1-Ox sample compared to the NMC811OH-Ox sample may be due to cation mixing. It has been related that boron doping increases cation mixing lead to decreases I(003)/I(104) with increasing to Ni^{2+}/Ni^{3+} [209].

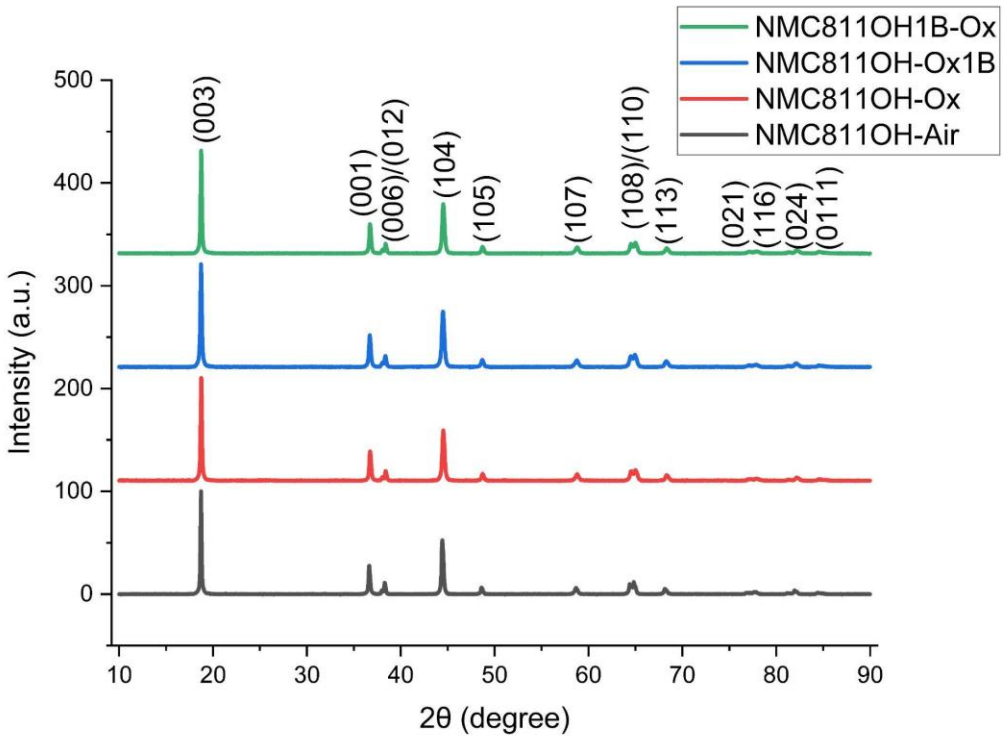

Figure 4.4 : XRD graphs of samples.

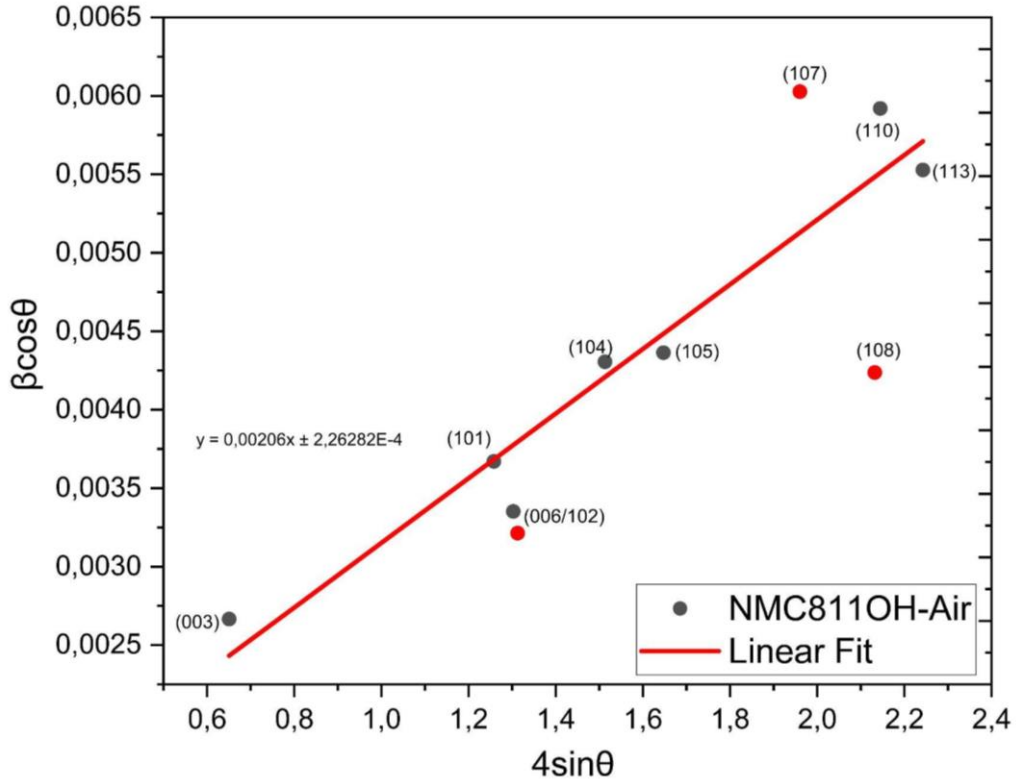

Figure 4.5 : Williamson-Hall plot of NMC811OH-Air.

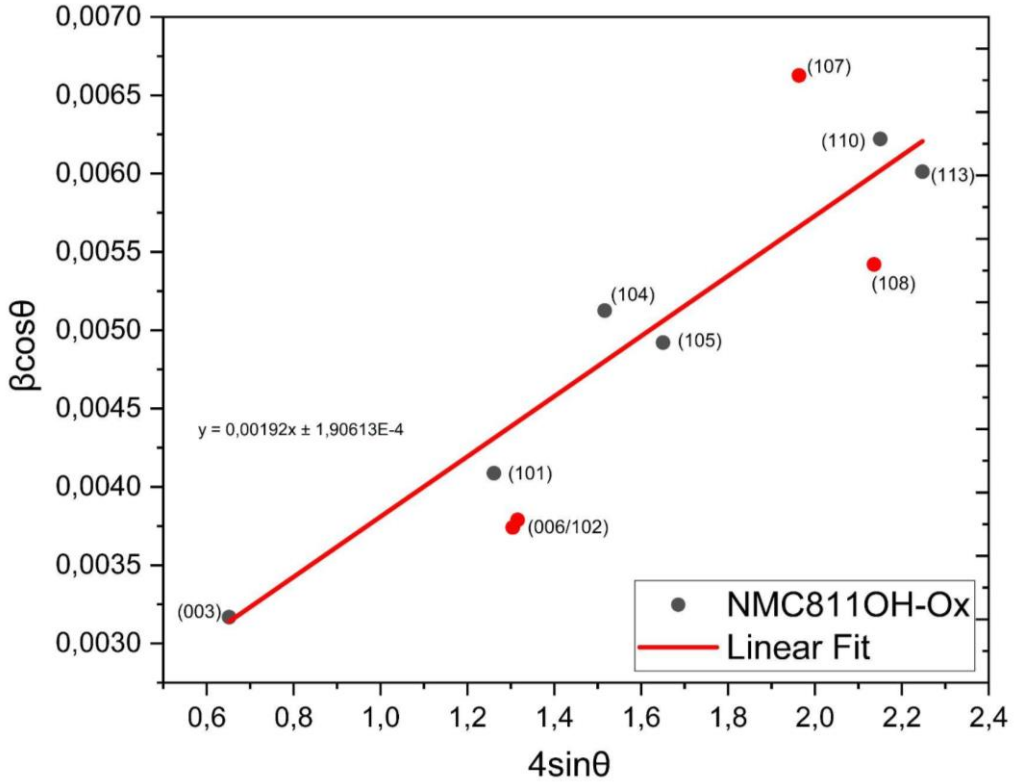

Figure 4.6 : Williamson-Hall plot of NMC811OH-Ox.

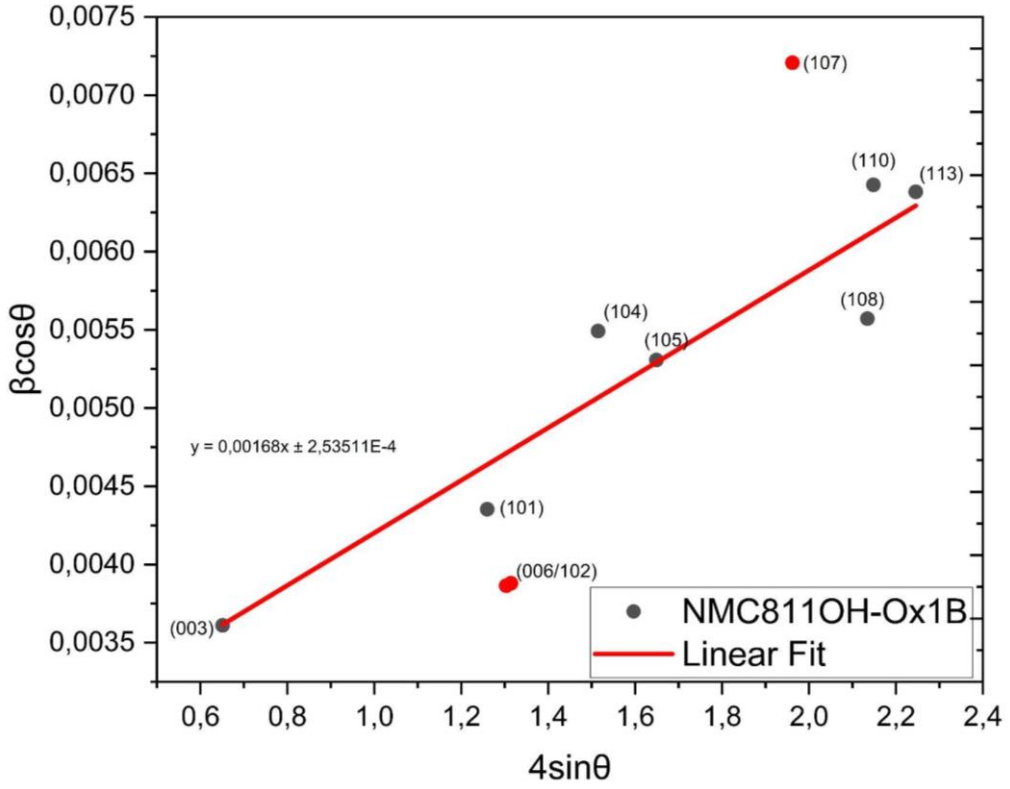

Figure 4.7 : Williamson-Hall plot of NMC811OH-OxB1.

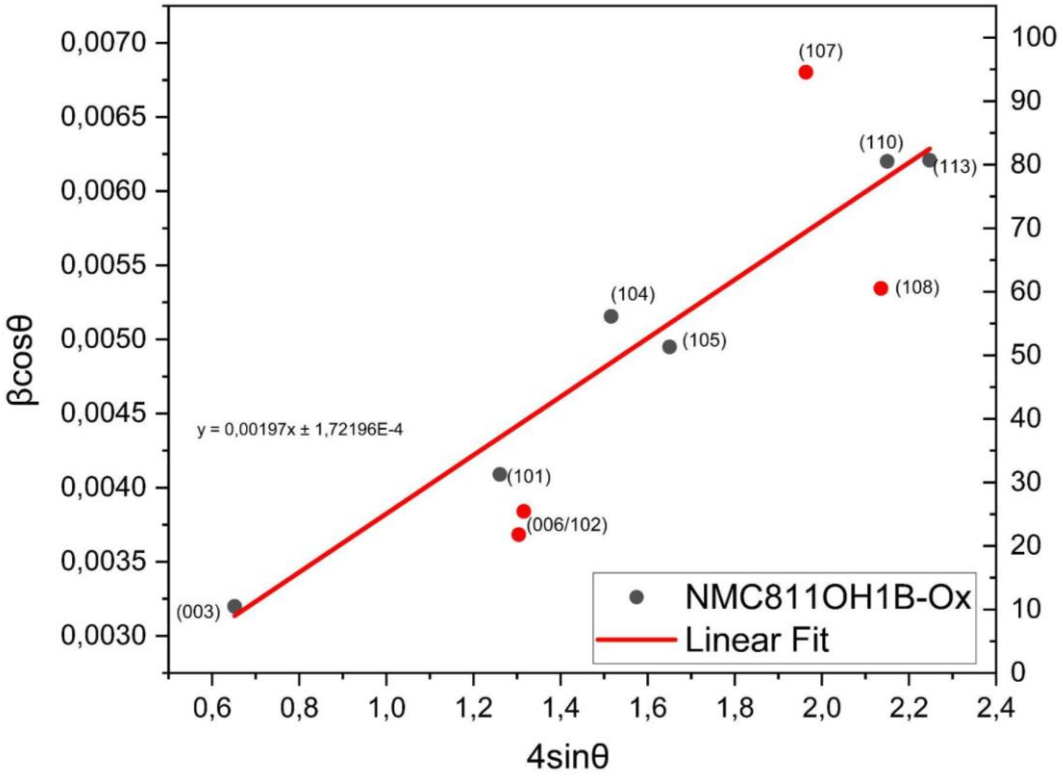

Figure 4.8 : Williamson-Hall plot of NMC811OHB1-Ox.

The Williamson-Hall UDM (uniform deformation model) method is utilized to determine the mean values of crystallite size and lattice strain from XRD data. In this approach, relation between $\beta_{\text{Crystallite size}}$ and $\beta_{\text{Latticestrain}}$ is given Equation 4.3.

$$\beta_{\text{Sample}} = \beta_{\text{Crystallite size}} + \beta_{\text{Latticestrain}} \quad (4.3)$$

$\beta_{\text{Crystallite size}}$ and $\beta_{\text{Latticestrain}}$ are given Equation 4.4 and Equation 4.5 respectively.

$$\beta_{\text{Crystallite size}} = K\lambda/D\cos\theta \quad (4.4)$$

$$\beta_{\text{Lattice strain}} = 4\varepsilon\tan\theta \quad (4.5)$$

Combined equation is;

$$\beta_{\text{Sample}} = K\lambda/D\cos\theta + 4\varepsilon\tan\theta \quad (4.6)$$

The symbols refers to K is a constant shape factor (typically around 0.9 or 0.94), λ is the X-ray wavelength, D is the crystallite size, ϵ is the microstrain, θ is the Bragg angle. Williamson-Hall method is applied and curves of fit gathered from XRD data of the samples are given in Figures 4.6-4.9. The slope of the curve is related to the microstrain and the part where the curve intersects the vertical axis is related to the crystallite size [212]. Calculated crystallite size and microstrain values are given in Table 4.1.

Firstly, the crystallite size NMC811OH-Air is much larger than other samples. In some research [213, 214] in oxygen atmosphere and air atmosphere, increasing calcination temperatures increases crystallite size and primer particles' sizes independant of atmosphere. Li [215] et all, have obtained that as a result of the synthesis of NMC622 containing different Li/TM ratios, the primary particles in the structure grew and the crystallite size increased with the increasing Li/TM ratio. In this study, The Li/TM ratio was 1.03. The crystallite size is found to be 60.59 for NMC811OH-OxB1 which is calcined at 450 ^{o}C for 4 hours and 750 ^{o}C for 12 hours. As stated earlier that during calcination there is a risk of having boron by-product which is forms due to lithium deficiency and result in poor electrochemical performance.

In the case of NMC811OH-OxB1 the crystallite size growth may have decreased due to boron by-product, causing lithium deficiency in the structure. NMC811OHB1-Ox and NMC811OH-Ox samples have almost the same crystallite size of 78.28 and 76.62 nm respectively. NMC811OH-Air sample had the highest crystallite size (132.86 nm) and the highest microstrain ($2.06\text{x}10^{-3}$) . This highest strain may be related to oxygen vacancies in lattice structures leading to distortion of lattice structure caused by air

atmosphere. The lowest microstrain in structure is calculated for NMC811OHB1-Ox sample. The difference in the microstrains obtained for NMC811OH-Air and NMC811OHB1-Ox can be related to low pore distribution and high size in the structure and the orientation of primary particles in NMC811OHB1-Ox sample. Even the lowest value in microstrain, the anisotropic primary particle distribution in the cross-section and the highest cation mixing (lowest I(003)/I(104) ratio) dominates the electrochemical tests. NMC811OHB1-Ox have are calculated almost a little more microstrain value like crystallite size than NMC811OH-Ox.

Table 4.1 : Crystallite Size, microstrain and I(003)/I(104) ratios in the samples.

Sample	Crystallite Size (nm)	Microstrain (ε) x10^{-3}	I(003)/I(104)
NMC811OH-Air	132.86	2.06	1.22
NMC811OH-Ox	76.62	1.92	1.24
NMC811OH-OxB1	60.59	1.68	1.17
NMC811OHB1-Ox	78.28	1.97	1.22

Table 4.2 shows the Rietveld analysis results of the samples calcined at oxygen atmosphere. All sample XRD peaks almost matched PDF-01-088-4075 ($LiNi_{0.8}Mn_{0.1}Co_{0.1}O_2$) with a card no and there is no impurity peak. There are a little shifting on high angle peaks. It is observed that the a-axis, c-axis and cell volume increases with the presence of boron in the structure. The cell expands as the B^{+3} ion is positioned at tetrahedral sites between the Li and NMC layers. With the increasing c/a ratio in the structure, the transfer of Li^+ ions becomes easier by opening the gap between Li and NMC layers, thus improving the transfer of Li ions, increasing the capacity and improving capacity retention with a more stable structure. Although equal amounts of boron were used NMC811OHB1-Ox and NMC811OH-OxB1 samples, NMC811OH-OxB1 shows lower c/a ratio than NMC811OHB1-Ox, it may indicate that the structure is not formed properly despite the boron doping. The formed boron by-product (like Li_3BO_3) may decrease of lithium in the layered structure [104]. Li et al. [214], the structure grew in the a direction with the decreasing Li ratio in the structure leading to the failure of the layered structure to develop well due to lithium deficiency.

Table 4.2 : Rietveld analysis results.

Sample	a	c	c/a	Cell Volume (Å^3)	R_{wp}	Rp	GOF
NMC811OH-Ox	2.867	14.198	4.9523	101.071	5.28	4.10	1.81
NMC811OH-OxB1	2.869	14.204	4.9508	101.252	5.91	4.47	2.02
NMC811OHB1-Ox	2.8671	14.213	4.9540	101.312	7.48	5.43	2.56

4.2 Electrochemical characterization results

4.2.1 Galvanostatic test results

Fabricated cathodes are punched then CR2032 standard half-cells are assembled for their electrochemical assessment, between the cutoff voltages of 2.7-4.3 V.

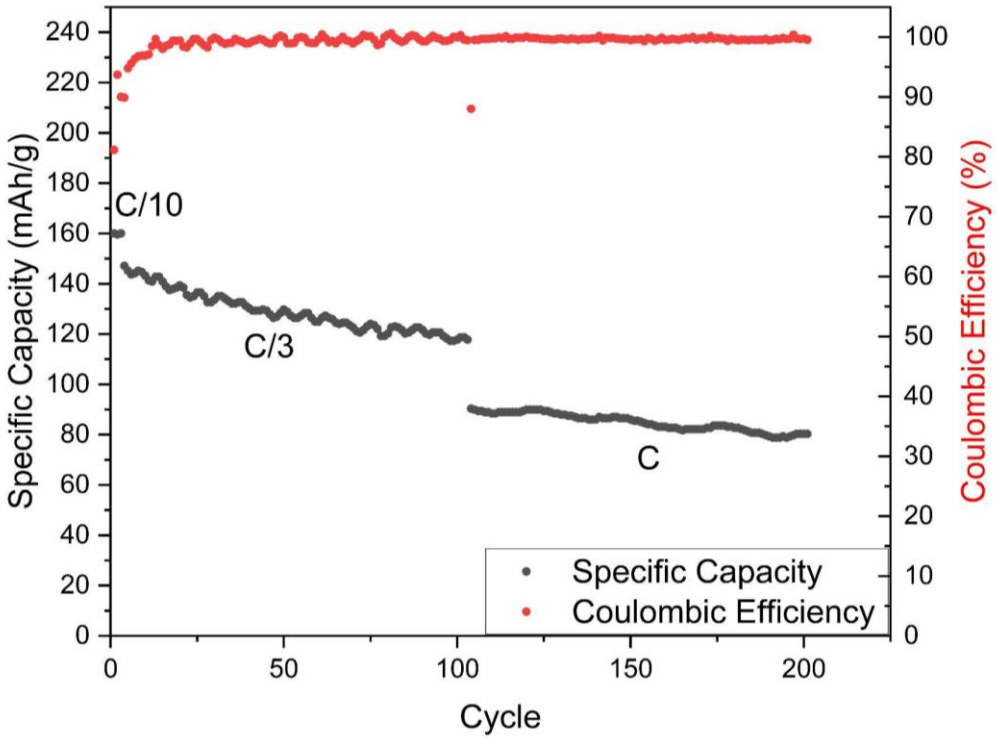

Figure 4.9 : Specific discharge capacity-cycle curve of NMC811OH-Air.

Specific discharge capacity and cycle curves of NMC811OH-Air, NMC811OH-Ox, NMC811OH-OxB1, NMC811OHB1-Ox are shown in Figures 4.9, 4.10, 4.11 and 4.12 respectively. Under a current load of C/10, NMC811OH-Ox sample gave the highest initial discharge capacity of 203 mAh/g. NMC811OHB1-Ox, NMC811OH-OxB1 and NMC811OH-Air deliver 188 mAh/g, 156 mAh/g and 160 mAh/g, respectively. After 3 discharge cycles the capacities are found to be 161 mAh/g, 211 mAh/g, 158 mAh/g, and 191 for NMC811OH-Air, NMC811OH-Ox, NMC811OH-OxB1,

NMC811OHB1-Ox, respectively. Samples NMC811OH-Air and NMC811OH-OxB1 gave similar initial discharge capacities even though they were calcined in different atmospheres.

Amalraj [202] et al. in their research, mixed Ni-Rich cathode active material with LiOH along with 1% boron source. As a result of galvanostatic cycle, it was observed that the capacity of boron doped sample decreased from 212 mAh/g to 189 mAh/g in the first discharge curve. It was stated that such capacity loss may be caused by Li_3BO_3 formation in the structure during calcination. You et al. [210] heat-treathed precursor at 600ºC for 3 hours before starting the calcination process. An improvement in the charge and discharge capacities are noted following pre-heat treatment. The first charge and discharge capacity improved in the results obtained compared to not heat treated sample and better performance obtained after galvanostatic test after boron doping. However, on the surface of cathode material also has boron by-product similarly Amalraj [202]. Skvortsova et al. [104] obtained similar capacities with the undoped sample in the first cycles by using excess lithium source according to the amount of boron in boron doping and used excess Li source to reduce lithium deficiency caused by the formation of Li_3BO_3 structure. Therefore, the lower capacity performance of NMC811OH-OxB1 may be related to the inhomogeneous secondary particle structure of the sample during calcination or the lithium deficiency (Figure 4.12).

Under a current load of C/3 and C, capacity retentions are found to be 78% and 88%, 88% and 92%, 88% and 89.67%, and 96.4% and 94.7% for NMC811OH-Air NMC811OHB1-Ox NMC811OH-OxB1 and NMC811OH-Ox, respectively.

In Figure 4.13, 1st cycle at C/3, dQ/dV-voltage curves of are given NMC811OH-Air, NMC811OH-Ox, NMC811OHB1-Ox and NMC811OH-OxB1. The obtained oxidation peaks in dQ/dV-voltage curves are H1 to M (around 3.75 V), M to H2 (around 4V) and H2 to H3 (around 4.2V) respectively [211]. In dQ/dV-voltage curve, boron doped samples' H1-M peaks are shifted left side and H2-H3 peaks shifted right side due to boron-doped structures expand the c-axis and facilitate the diffusion of lithium ions. Kleiner et al. [196], in the research where NMC811 was boron doped, a similar shift was observed in the dQ/dV-voltage curve in the H1-M peak to the left and in the H2-H3 peak to the right. First H1-M peak of NMC811OH-Air is the sharpest than other samples. The fact that this sample is exposed to air during storage, a very

thin layer of lithium carbonate or hydroxide compounds may form over Ni-rich NMC powder, leaching to increase the polarization of H1-M phase transformation [216, 217].

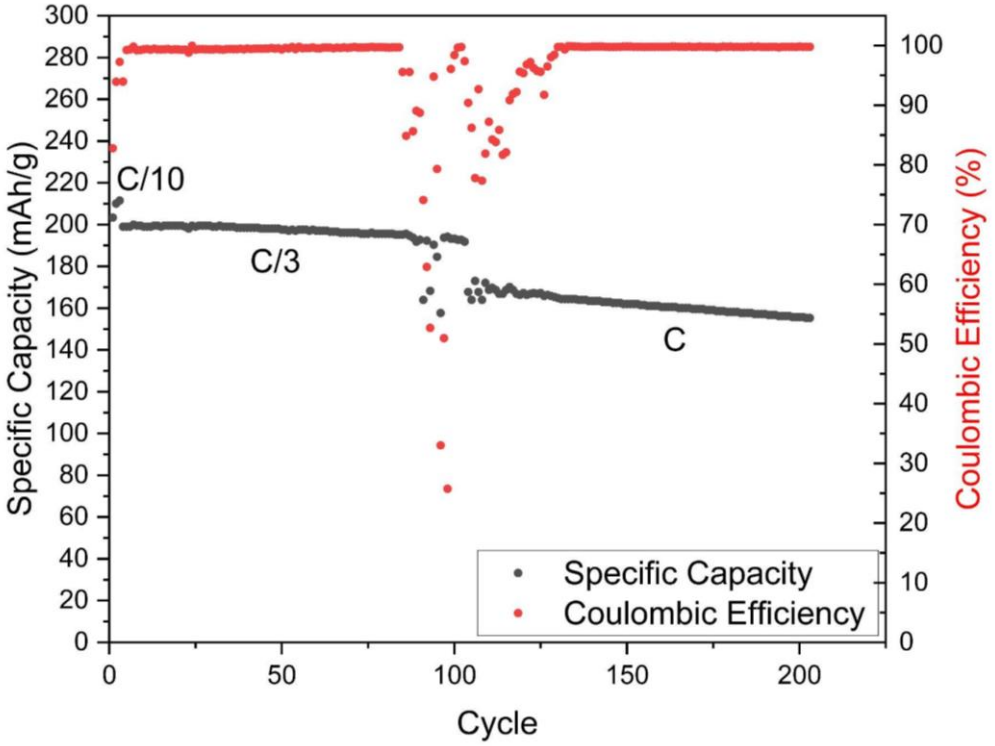

Figure 4.10 : Specific discharge capacity-cycle curve of NMC811OH-Ox.

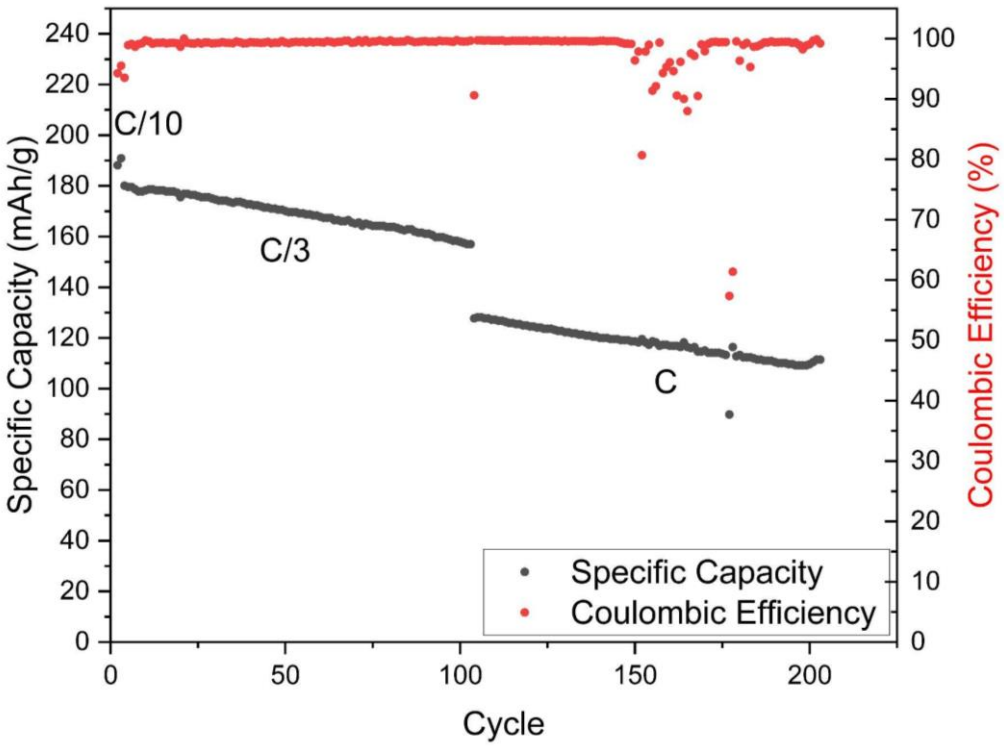

Figure 4.11 : Specific discharge capacity-cycle curve of NMC811OHB1-Ox.

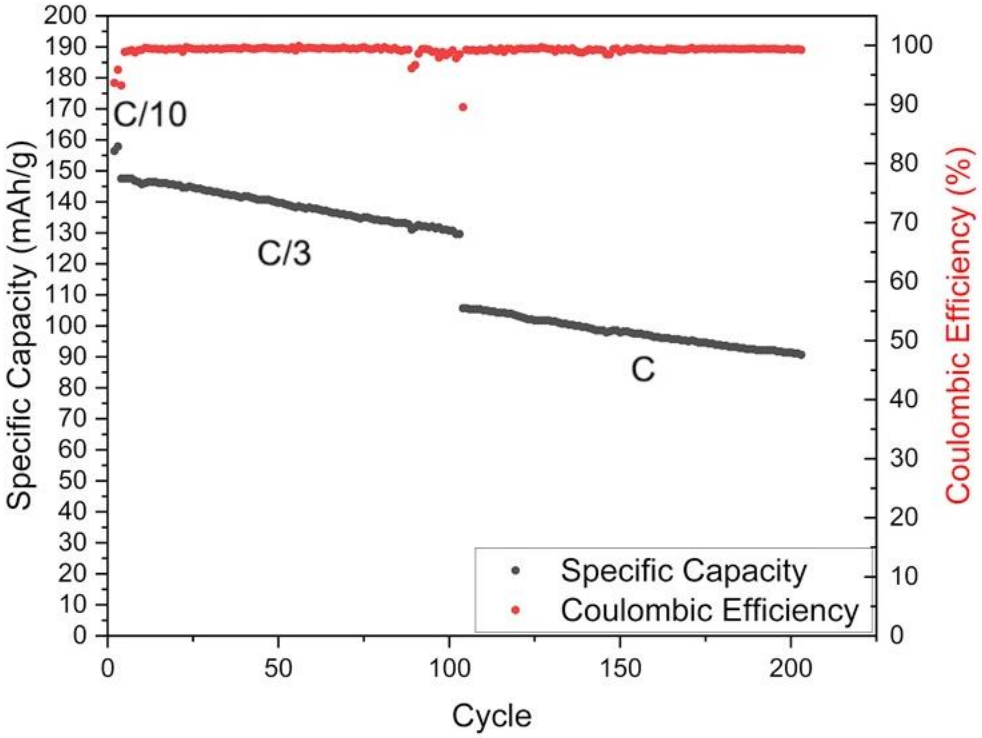

Figure 4.12 : Specific discharge capacity-cycle curve of NMC811OH-OxB1.

After 50 cycle at C/3, dQ/dV-voltage curves of Figures 4.14-4.17 are given NMC811OH-Air, NMC811OH-Ox, NMC811OHB1-Ox, NMC811OH-OxB1, respectively. The intensity of a peak indicates how intense the phase transformation is in that region. The H2-H3 phase transformation region causes the crystal lattice to suddenly shrink in the c direction during charging and expand in the c direction during discharge for Ni-rich cathode active materials, causing the structure to evolve into a rock-salt structure that can release oxygen and irreversibly. In Figure 4.14 NMC811OH-Air sample has showed H2-H3 at 4.2V with 0.41 mAh/Vg in the first cycle. After 50 cycle, H2-H3 peak shifted to 4.24V and with 0.25 mAh/Vg and the peaks has almost disappeared and spread over a wide area and the cathodic oxidation peak almost disappear. It can be mentioned that there is intense oxygen release during H2-H3 phase transformations for NMC811OH-Air sample and high transformation occurs from layered structure to rock-salt structure. In Figure 4.15 NMC811OH-Ox sample have showed H2-H3 at 4.2V with 0.63 mAh/Vg and after 50 cycle only shifted to 4.21 V and reduce to 0.6 mAh/V and the cathodic peaks also have showed almost same peak position and dQ/dV. dQ/dV-voltage curve of NMC811OH-Ox is a proof excellent capacity retention on cycle test at C/3 which may be related to the pore distribution on center and orientation of primary particles along the cross section of the particle as shown in Figure 4.10. In Figure 4.16, NMC811OH1B-Ox sample's first

anodic peak at 4.2 V shifted to 4.22 V and reduced dQ/dV from 0.55 mAh/Vg to 0.45 mAh/Vg and first cathodic peak 4.17 V to 4.13 V after 50 cycle. In Figure 4.17, NMC811OH-Ox1B sample showed first anodic peak at 4.21 V shifted to 4.22 V and reduced dQ/dV from 0.52 mAh/Vg to 0.38 mAh/Vg and first cathodic peak 4.17 V to 4.13 V after 50 cycle similarly NMC811OH1B-Ox sample. Smallest dQ/dV change in the voltage value obtained in NMC811OH-Ox sample after 50 cycle is believed to be attributed to its superior morphogical and structural properties.

To evaluate the rate performances of each cathode, they are tested under different current loads. Rate test (C/10, C/5, C/3, C, 2C, and 5C - 5 cycles for each rate) of samples calcined in an oxygen-rich environment is given in Figure 4.22. At C/10, C/5 and C/3, NMC811OHB1-Ox has higher specific discharge capacity from NMC811OH-Ox. Skvortsova et al. [104] stated that this could be due to the high ionic conductivity of the thin Li_3BO_3 layer formed on the surface of the sample. Although the NMC811OHB1-Ox sample was boron doped for co-precipitation on the surface of NMC811OHB1-Ox Li_3BO_3 may be formed. On the other hand, after 2C rates NMC811OH-Ox shows better performance from NMC811OHB1-Ox. According to Park et al. [199], boron has low electronic conductivity so negatively affects the rate capability at high rates.

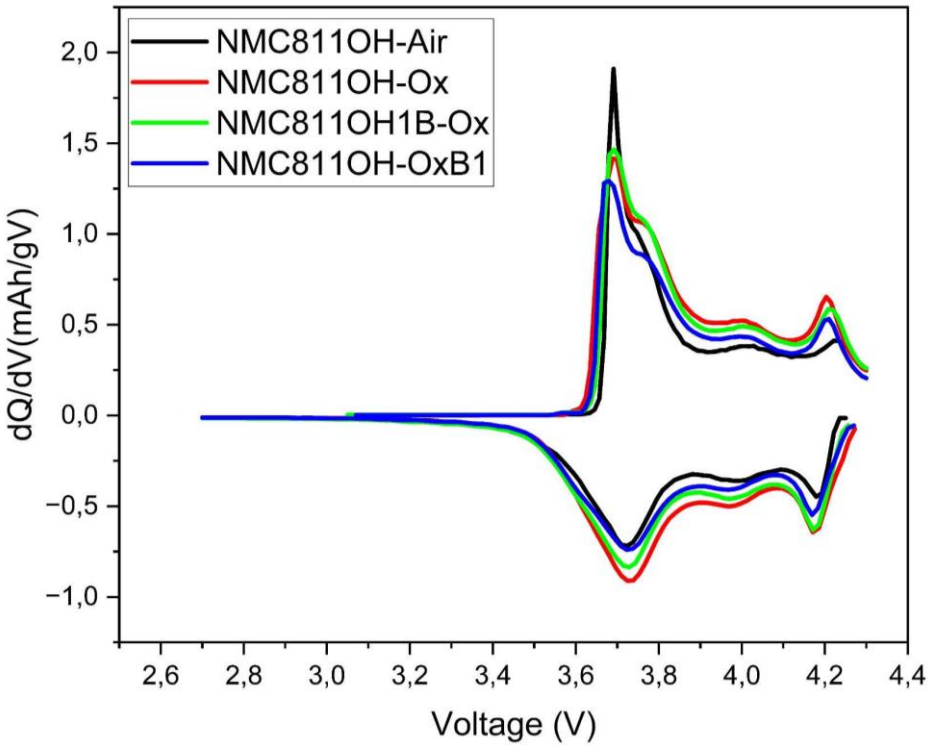

Figure 4.13 : dQ/dV-voltage curves of samples at C/3 rate 1st cycle.

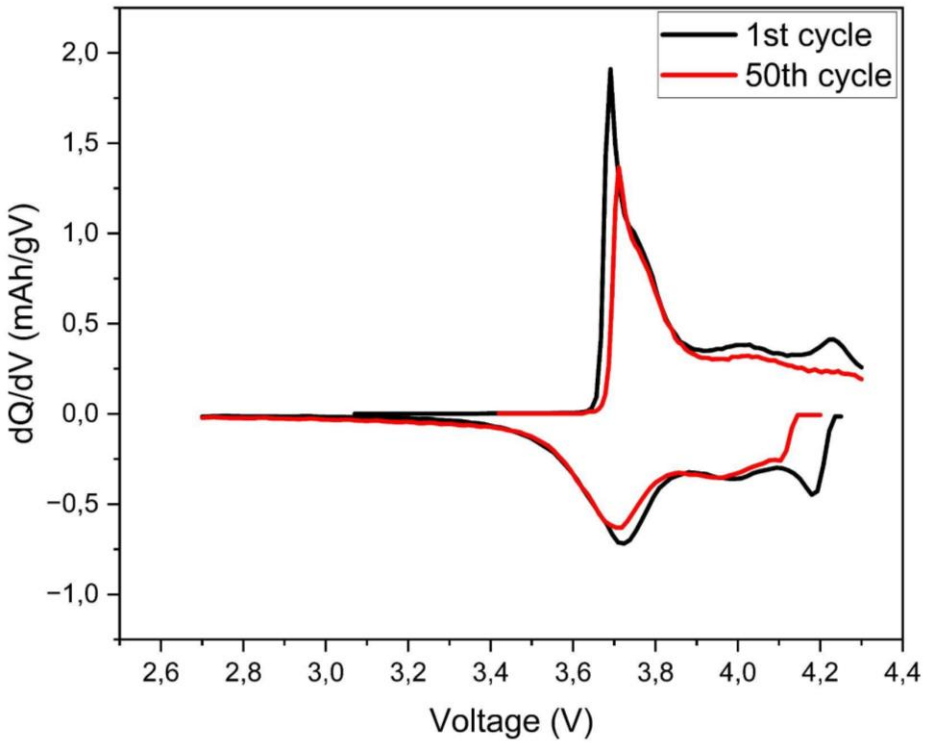

Figure 4.14 : dQ/dV-voltage curves of NMC811OH-Air at C/3 rate 1st cycle and 50th cycle.

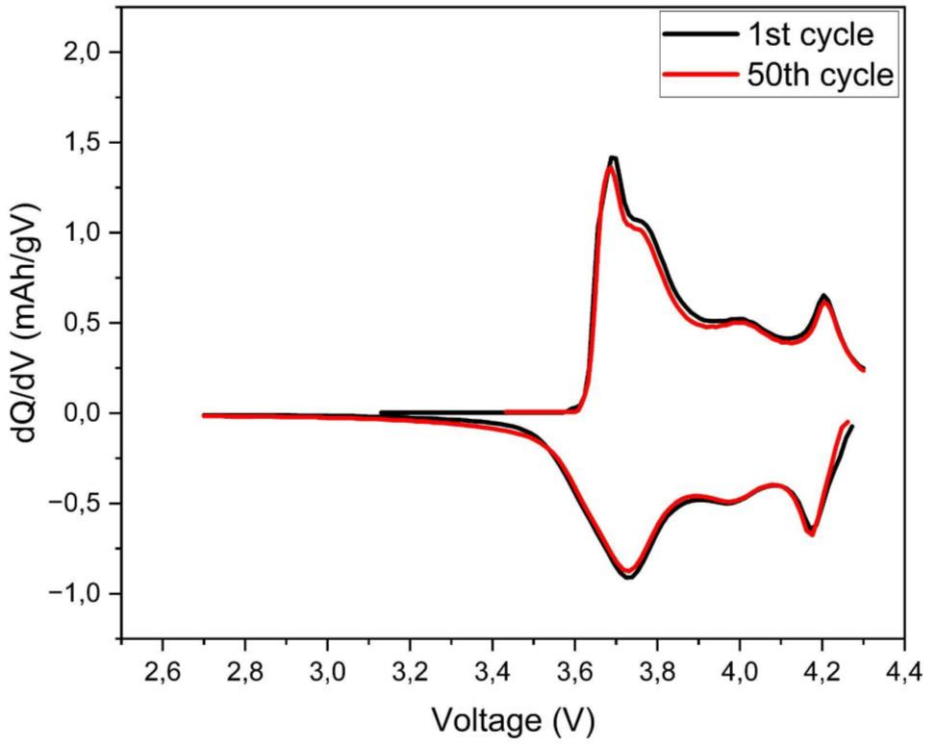

Figure 4.15 : dQ/dV-voltage curves of NMC811OH-Ox at C/3 rate 1st cycle and 50th cycle.

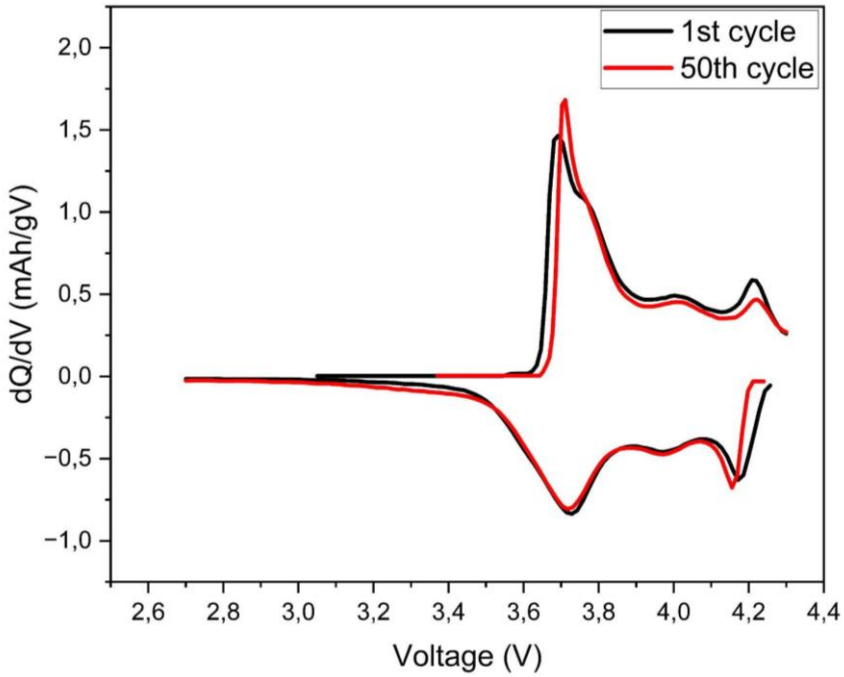

Figure 4.16 : dQ/dV-voltage curves of NMC811OH1B-Ox at C/3 rate 1st cycle and 50th cycle.

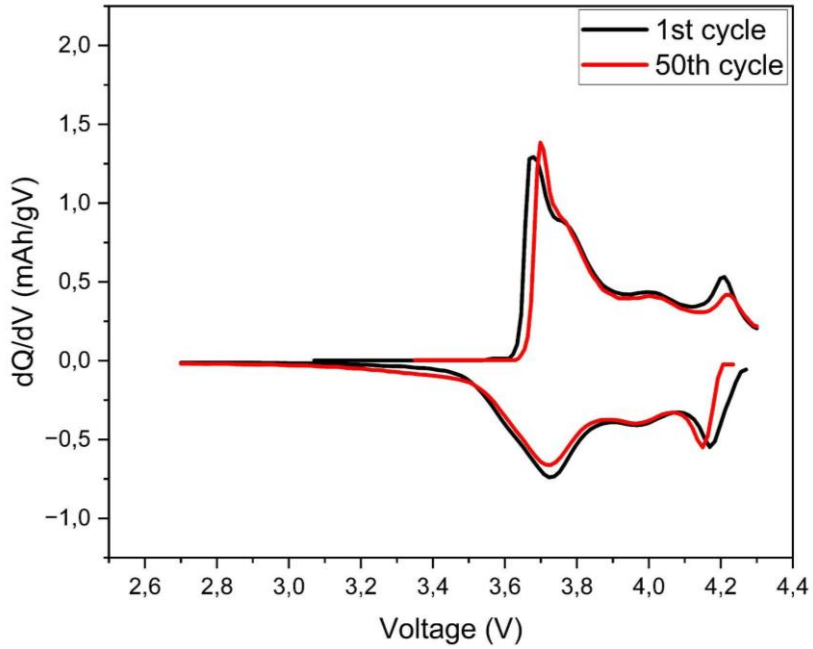

Figure 4.17 : dQ/dV-voltage curves of NMC811OH-Ox1B at C/3 rate 1st cycle and 50th cycle.

The galvanostatic charge discharge capacity curves of Figures 4.18, 4.19, 4.20, 4,21 are given NMC811OH-Air, NMC811OH-Ox, NMC811OH1B-Ox, NMC811OH-OxB1 respectively. As in the dQ/dV-voltage curves, the approach of the voltages of the charge and discharge curves to each other as a result of cycles indicates the loss of capacity due to the potential difference at the initial voltages. Initial charge start

voltage of cycles have changed after 203 cycle are 0.21 V, 0.12 V, 0.17 V and 0.20 V for NMC811OH-Air, NMC811OH-Ox, NMC811OH1B-Ox, NMC811OH-OxB1 respectively. It is similar to the result obtained from dQ/dV anodic curves.

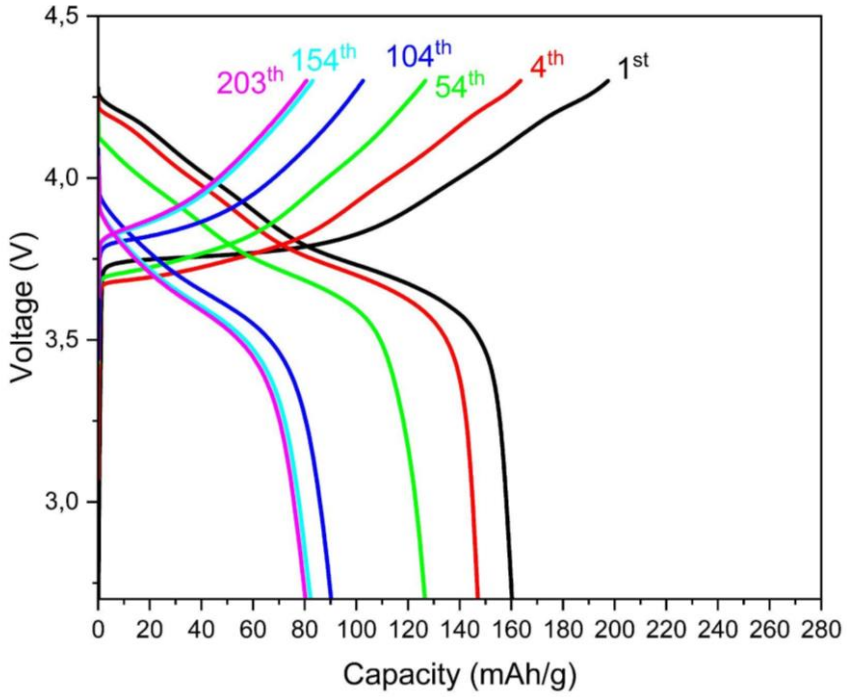

Figure 4.18 : Galvanostatic charge discharge capacity of NMC811OH-Air.

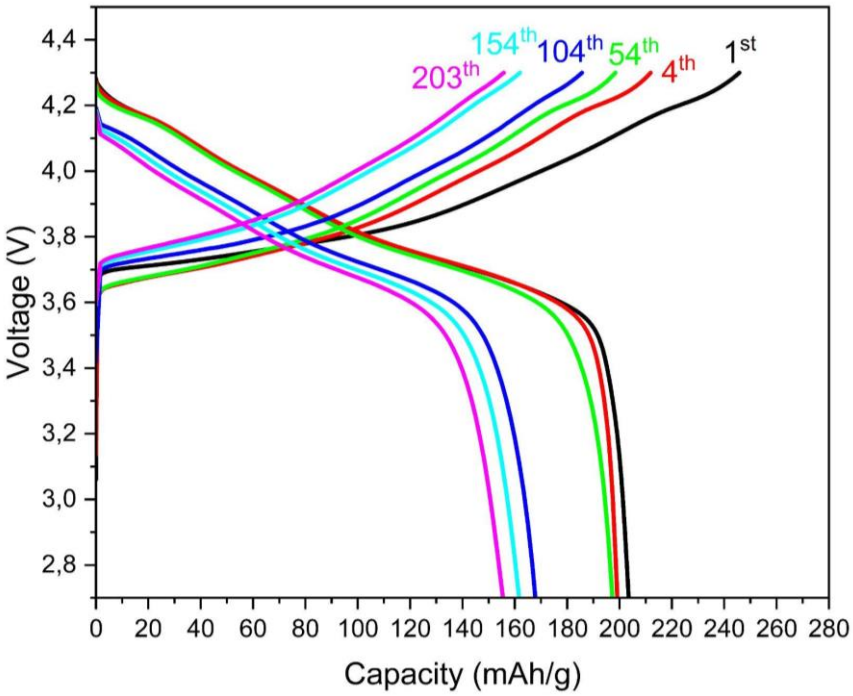

Figure 4.19 : Galvanostatic charge discharge capacity of NMC811OH-Ox.

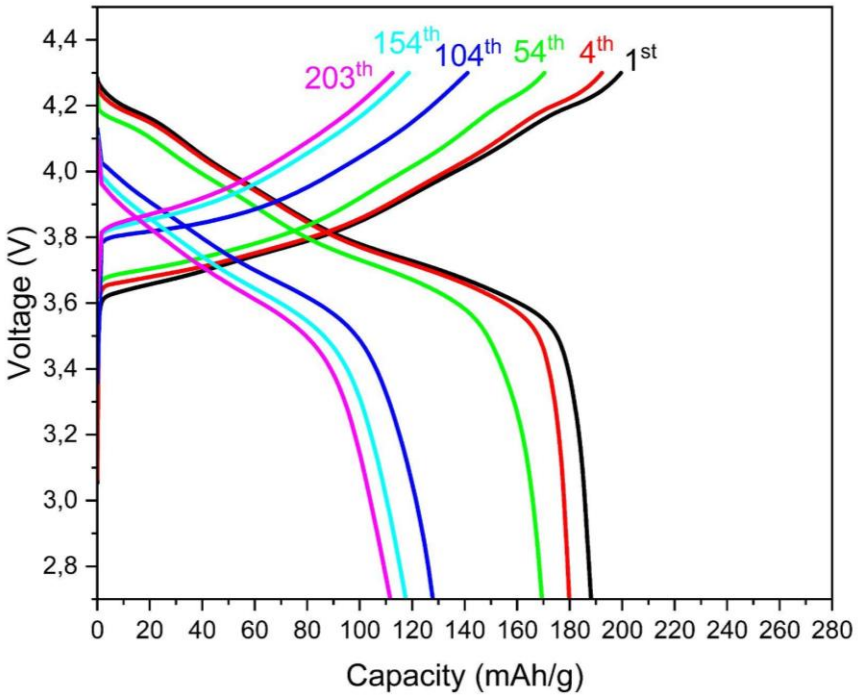

Figure 4.20 : Galvanostatic charge discharge capacity of NMC811OH1B-Ox.

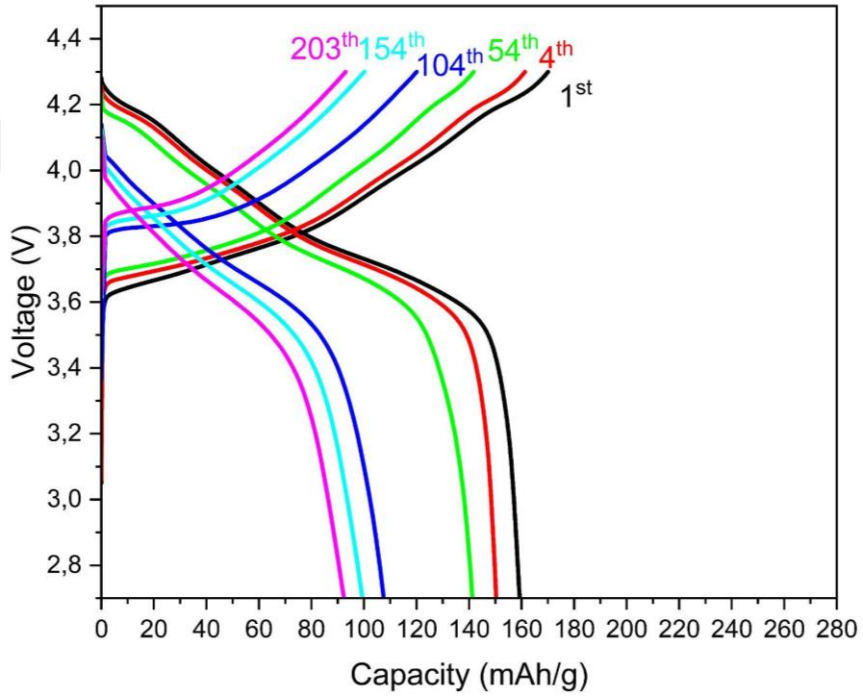

Figure 4.21 : Galvanostatic charge discharge capacity of NMC811OH-OxB1.

4.2.2 Potentiostatic test results

4.2.2.1 Cyclic voltammetry

The cyclic voltammetry results of Figures. 4.23, 4.24, 4.25, 4.26 are given NMC811OH-Air, NMC811OH-Ox, NMC811OH-OxB1, NMC811OHB1-Ox

respectively. The obtained oxidation peaks in cyclic voltammetry curves are related to H1 to M (around 3.75 V), M to H2 (around 4V) and H2 to H3 (around 4.2V) transformation, respectively [215]. First upper peak refers to anodic reaction peak and first lower peak refers to cathodic peak. First anodic and first cathodic peak voltage difference shows the reversibility of reactions [211]. Voltage gaps NMC811OH-Air, NMC811OH-Ox, NMC811OH-OxB1, NMC811OHB1-Ox are 0.226V, 0.12V, 0.194V and 0.155V respectively for H1-M transformation. NMC811OH-Ox's reversibility can be considered good compared to others. The H2-H3 peak shift towards higher potentials during CV indicating an increase in the polarization of the electrode which necessitates higher energy to achieve specific redox reactions. As a result, mechanisms such as capacity loss and electrolyte dissolution are likely to occur [74]. The peak related to H2-H3 phase transformation is shifted to higher voltage value as the covalency structure of TM-O bonds is modified by boron doping (Figure 4.24 and 4.25). The anodic and cathodic peak positions related to H2-H3 phase transformation could be used to discuss the reversibility of anisotropic changes occurred in cycling. In the first cycle, voltage differences between the anodic and cathodic peaks of this reaction (H2-H3 transformation) are found to be 0.052V, 0.044V, 0.078V and 0.054V for NMC811OH-Air, NMC811OH-Ox, NMC811OH-OxB1, NMC811OHB1-Ox.

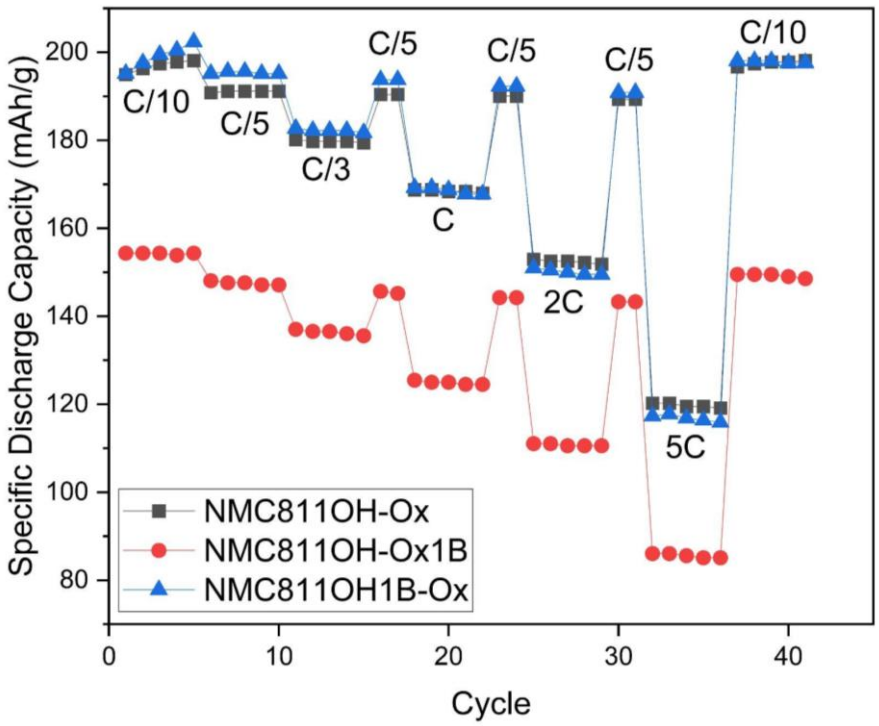

Figure 4.22 : Rate test of samples calcined in an oxygen-rich environment.

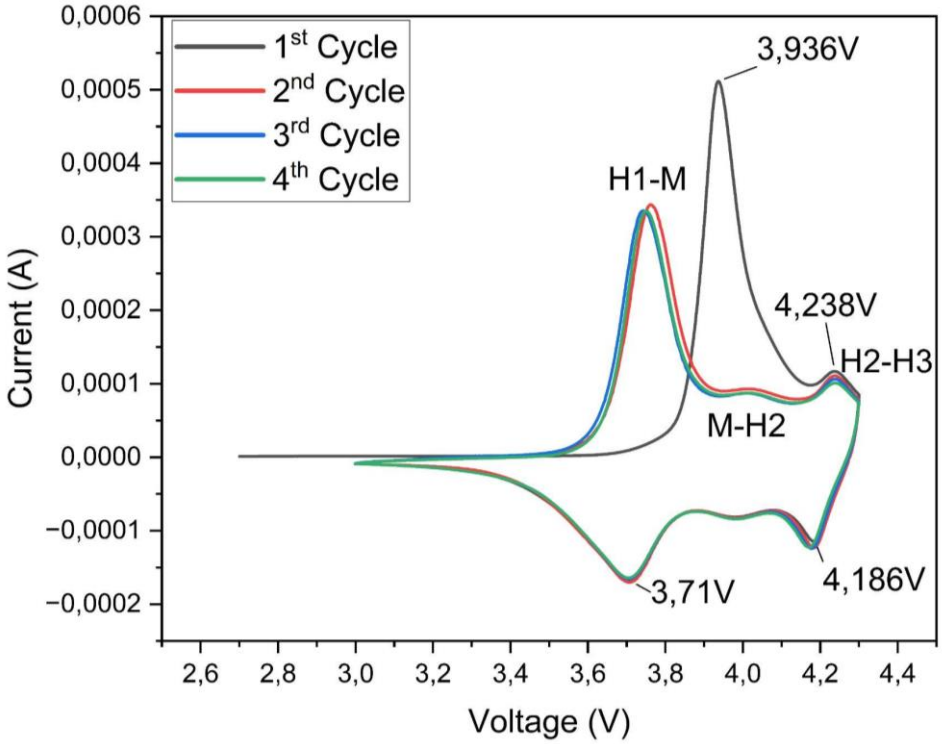

Figure 4.23 : Cyclic voltammetry curve of NMC811OH-Air sample.

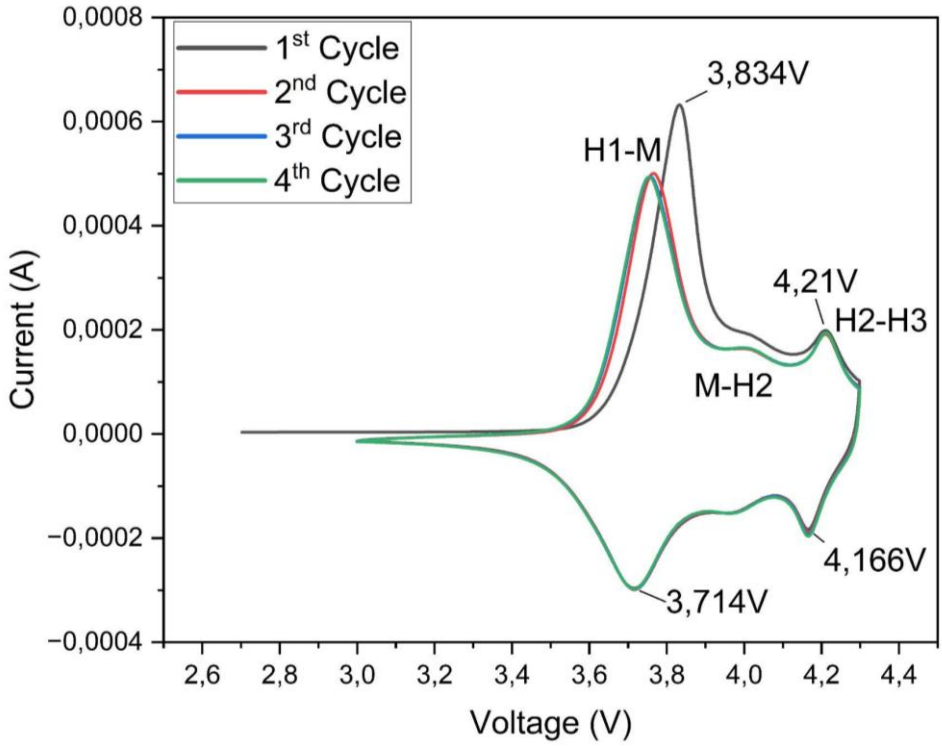

Figure 4.24 : Cyclic voltammetry curve of NMC811OH-Ox sample.

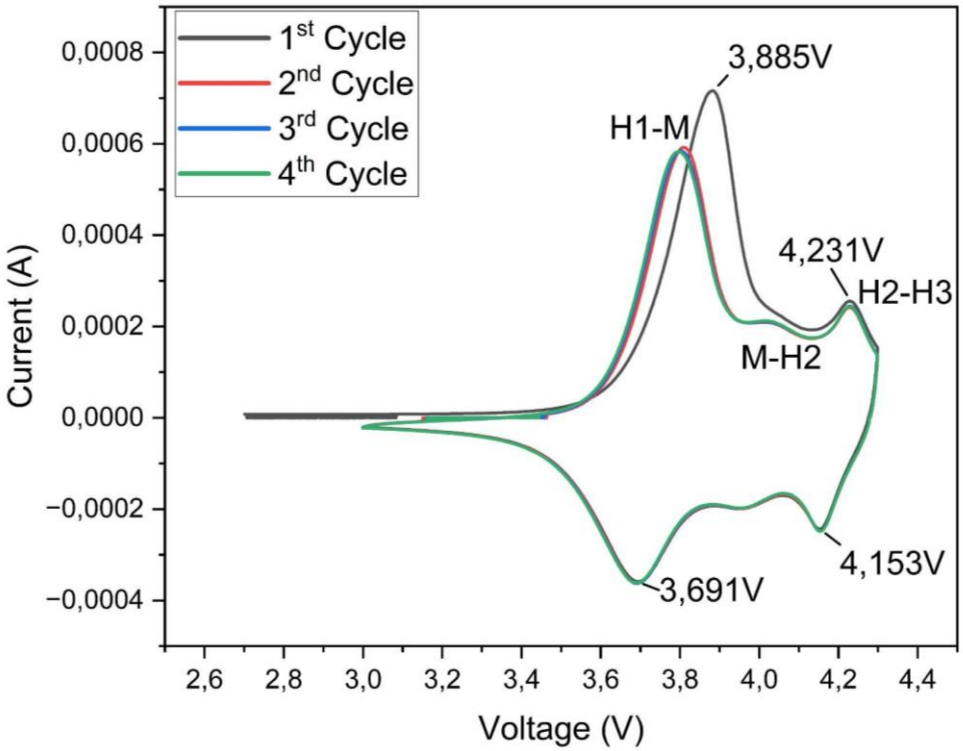

Figure 4.25 : Cyclic voltammetry curve of NMC811OH-OxB1 sample.

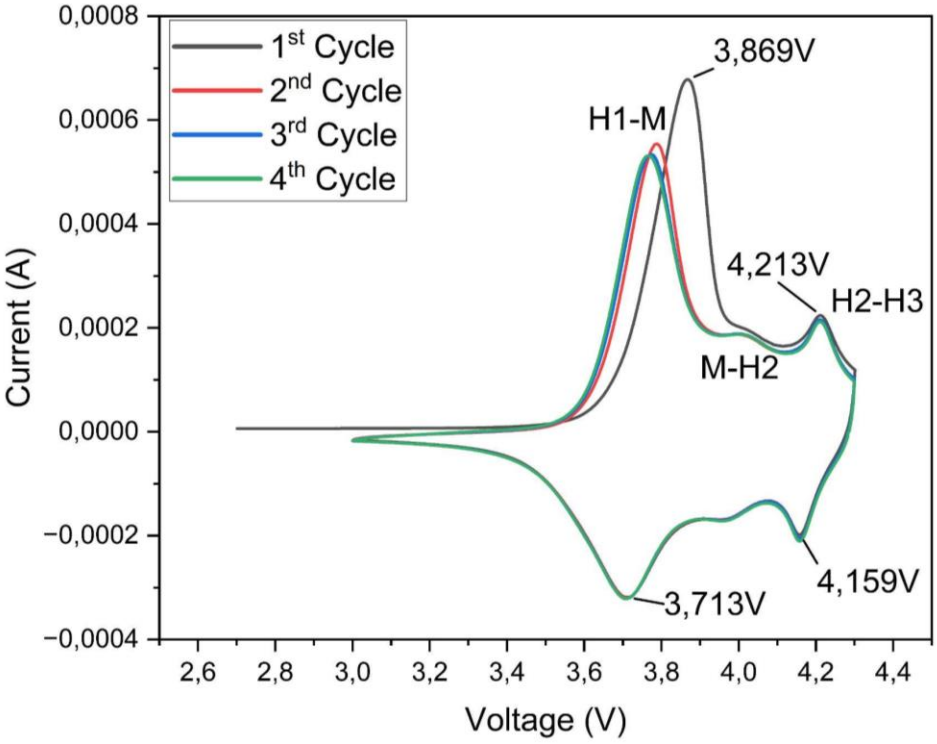

Figure 4.26 : Cyclic voltammetry curve of NMC811OHB1-Ox sample.

Then, after 4 cycles, voltage differences between the anodic and cathodic peaks of this reaction (H2-H3 transformation) are found to be 0.0064V, 0.0045V, 0.0077V, and 0.0054V for NMC811OH-Air, NMC811OH-Ox, NMC811OH-OxB1,

NMC811OHB1-Ox. Voltage range does not change in samples produced in oxygen environment can be associated with the irregular distribution of lithium ions[218] When the current change is examined, the loss current after 4 cycles of NMC811OH-Air, NMC811OH-Ox, NMC811OH-OxB1, NMC811OHB1-Ox are found to be 13.8%, 2.6%, 5.9% and 4.7% respectively. The fact that the number of peaks and the area under the CV curve of each electrode from 1^{st} to 2^{nd} cycle have been changed proves that an irreversible reaction occurs on each electrode surface initially. A scrutiny comparison demonstrates that NMC811OH-Air samples reveals the most remarkable decrease in the area remained under CV curve. Knowing that NMC811OH-Air sample is exposed to air during storage, possible lithium carbonate and hydroxide compounds formation over the particle surface and its morphological as well as structural properties may lead such performance [65]. Oxygen losses of samples made in an oxygen environment are proportional to their particle morphology.

5. CONCLUSIONS AND RECOMMENDATIONS

- NMC811 and 1% boron-doped NMC811 precursors have been successfully synthesized via co-precipitation method.
- The NMC 811 and 1% boron-doped NMC811 precursors are spherical and are composed of dense and finely oriented primary particles having a particle size range of 10-15 micrometers.
- Boron is also doped during calcination using air and oxygen atmosphere. After calcination the shape of the particles stayed spherical and their sizes were similar to the precursors.
- All samples show high crystallinity and good separation of (006)/(012) and (108)/(110) peaks.
- I(003)/I(104) ratio of NMC811OH-Air, NMC811OH-Ox, NMC811OH-OxB1, NMC811OHB1-Ox are calculated to be 1.22, 1.24, 1.17 and 1.22 respectively, showing well ordered structures and low cation mixings.
- Initial charge values of NMC811OH-Air, NMC811OH-Ox, NMC811OH-OxB1, NMC811OHB1-Ox samples at C/10 were obtained 160 mAh/g, 203 mAh/g, 156 mAh/g, 188 mAh/g respectively. After 100 cycle at C/3, NMC811OH-Ox showed the highest capacity retention of 96.4%.
- In the cyclic voltammetry test, all samples show characteristic peaks H1-M and H2-H3. NMC811OH-Ox and NMC811OHB1-Ox show higher reversibility .
- It is understood that not only the whereabouts of the doping, the calcination parameters are vital for effective boron doping due to the probability of having lithium deficiency as a result of Li and B containing (Li_3BO_3) byproduct formations. Advanced analyses are needed to understand the formation mechanism and their effect on the structure and electrochemical behavior of the cathode active materials.

REFERENCES

[1] **Keyser P. T.** (1993). The purpose of the Parthian Galvanic cells: a first-century A.D. electric battery used for analgesia. Journal of Near Eastern studies, 52(2), 81–98. https://doi.org/10.1086/373610

[2] **Battery University.** (2022, February 22). *BU-101: When was the battery invented?* https://batteryuniversity.com/article/bu-101-when-was-the-battery-invented

[3] **Kurzweil, P.** (2010). Gaston Planté and his invention of the lead–acid battery—The genesis of the first practical rechargeable battery. Journal of Power Sources, 195, 4424-4434.

[4] **Url-1** Electrochemistry Encyclopedia -- volta and the "pile." (n.d.). https://knowledge.electrochem.org/encycl/art-v01-volta.htm

[5] **Pavlov, D. D.** (2011). Lead-acid batteries: Science and Technology A Handbook of lead-acid battery technology and its influcence on the product Detchko Pavlov. Elsevier.

[6] **Url-2** Developing controls for a 12V lithium- ion starter battery. (n.d.). https://repositorio.ufsc.br/xmlui/bitstream/handle/123456789/170512/PFC-20141-LucasVentura.pdf?sequence=1&isAllowed=y

[7] **Hirschlag, A.** (2022, February 28). *The battery invented 120 years before its time*. BBC News. https://www.bbc.com/future/article/20210223-the-battery-invented-120-years-too-soon

[8] **Vangapally, N., Penki, T. R., Elias, Y., Muduli, S., Maddukuri, S., Luski, S., Aurbach, D., & Martha, S. K. (2023).** Lead-acid batteries and lead–carbon hybrid systems: A Review. *Journal of Power Sources*, *579*, 233312. https://doi.org/10.1016/j.jpowsour.2023.233312

[9] **Wulandari, T., Fawcett, D., Majumder, S., & Poinern, G.** (2023). Lithium-Based Batteries, History, Current Status, Challenges and Future Perspectives. https://doi.org/10.22541/au.169022042.20615901/v1

[10] **Reddy, M. V., Mauger, A., Julien, C. M., Paolella, A., & Zaghib, K.** (2020). Brief history of early lithium-battery development. Materials, 13(8), 1884. https://doi.org/10.3390/ma13081884

[11] **Yoshino, A.** (2014). 1 - Development of the Lithium-Ion Battery and Recent Technological Trends. In Lithium-Ion Batteries Advances and Applications (pp. 1–20). Elsevier B.V. https://doi.org/10.1016/B978-0-444-59513-3.00001-7

[12] **Toro, L., Moscardini, E., Baldassari, L., Forte, F., Falcone, I., Coletta, J., & Toro, L.** (2023). A systematic review of battery recycling technologies: Advances, challenges, and future prospects. *Energies*, *16*(18), 6571. https://doi.org/10.3390/en16186571

[13] **Iea, & Aie.** (2009). Energy Technology Transitions for Industry : Strategies for the Next Industrial Revolution. Éditions OCDE. https://doi.org/10.1787/9789264068612-en

[14] **Url-3** 15 common lithium-ion battery applications. Ufine Battery [Official]. (n.d.). https://www.ufinebattery.com/blog/15-common-applications-of-lithium-ion-battery-technology/

[15] **Iea.** (n.d.). Policies to promote electric vehicle deployment – Global EV outlook 2021 – analysis. IEA. https://www.iea.org/reports/global-ev-outlook-2021/policies-to-promote-electric-vehicle-deployment

[16] **Url-4** Phase-out targets: LDV | Zev Transition Council. (n.d.). https://zevtc.org/tracking-progress/light-duty-vehicle-map/

[17] **Schumer, C., Elliott, C., & Gasper, R.** (2023, July 6). 5 countries taking action to reach net-zero targets. World Resources Institute. https://www.wri.org/insights/countries-taking-action-reach-net-zero-targets

[18] **Url-5** *$210 billion of announced investments in Electric Vehicle Manufacturing headed for the U.S. Atlas EV Hub.* (2023, February 23). https://www.atlasevhub.com/data_story/210-billion-of-announced-investments-in-electric-vehicle-manufacturing-headed-for-the-u-s/

[19] **Garsten, E.** (2024, November 7). *Ev sales pace is running short of power going into 2024. Forbes*. https://www.forbes.com/sites/edgarsten/2023/12/14/ev-sales-pace-is-running-short-of-power-going-into-2024/?sh=41cb17a37985

[20] **Insights, G. M. (n.d.).** *Lithium-ion battery market size, Growth Analysis Report 2032*. Global Market Insights Inc. https://www.gminsights.com/industry-analysis/lithium-ion-battery-market

[21] **Url-6** *Lithium-ion battery market size to hit USD 387.05 bn by 2032*. Precedence Research. (n.d.). https://www.precedenceresearch.com/lithium-ion-battery-market

[22] **Frith, J. T., Lacey, M. J., & Ulissi, U.** (2023). A non-academic perspective on the future of lithium-based batteries. *Nature Communications*, 14(1). https://doi.org/10.1038/s41467-023-35933-2

[23] **Raccichini, R., Amores, M., & Hinds, G.** (2019). Critical Review of the Use of Reference Electrodes in Li-Ion Batteries: A Diagnostic Perspective. BATTERIES-BASEL, 5(1), 12. https://doi.org/10.3390/batteries5010012

[24] **Shi, H., Barker, J., Saïdi, M. Y., Koksbang, R., & Morris, L.** (1997). Graphite structure and lithium intercalation. Journal of Power Sources, 68(2), 291–295. https://doi.org/10.1016/s0378-7753(96)02562-1

[25] **Hossain, M. A. M., Hannan, M. A., Ker, P. J., Tiong, S. K., Salam, M. A., Abdillah, M., & Mahlia, T. M. I.** (2024). Silicon-based nanosphere anodes for lithium-ion batteries: Features, progress, effectiveness, challenges, and prospects. Journal of Energy Storage, 99, 113371. https://doi.org/10.1016/j.est.2024.113371

[26] **Hossain, M. H., Chowdhury, M. A., Hossain, N., Islam, M. A., & Mobarak, M. H.** (2023). Advances of lithium-ion batteries anode materials—A review. Chemical Engineering Journal Advances, 16. https://doi.org/10.1016/j.ceja.2023.100569

[27] **Li, A., Yuen, A. C., Wang, W., De Cachinho Cordeiro, I. M., Wang, C., Chen, T. B., Zhang, J., Chan, Q. N., & Yeoh, G. H.** (2021). A review on lithium-ion battery separators towards enhanced safety performances and modelling approaches. Molecules, 26(2), 478. https://doi.org/10.3390/molecules26020478

[28] **Xiao, Y., Fu, A., Zou, Y., Huang, L., Wang, H., Su, Y., & Zheng, J.** (2022). High safety lithium-ion battery enabled by a thermal-induced shutdown separator. Chemical Engineering Journal, 438. https://doi.org/10.1016/j.cej.2022.135550

[29] **Horváth, D. V., Tian, R., Gabbett, C., Coleman, J. N., & Nicolosi, V.** (2022). Quantifying the Effect of Separator Thickness on Rate Performance in Lithium-Ion Batteries. Journal of the Electrochemical Society, 169(3). https://doi.org/10.1149/1945-7111/ac5654

[30] **Martins, V. L.** (2023). Advances on liquid electrolytes for Li-ion and Li metal batteries. CURRENT OPINION IN ELECTROCHEMISTRY, 38, 101241. https://doi.org/10.1016/j.coelec.2023.101241

[31] **Etacheri, V., Marom, R., Elazari, R., Salitra, G., & Aurbach, D. (2011).** Challenges in the development of advanced Li-ion batteries: a review. ENERGY & ENVIRONMENTAL SCIENCE, 4(9), 3243–3262. https://doi.org/10.1039/c1ee01598b

[32] **Das, D., Manna, S., & Puravankara, S.** (2023). Electrolytes, Additives and Binders for NMC Cathodes in Li-Ion Batteries-A Review. BATTERIES-BASEL, 9(4), 193. https://doi.org/10.3390/batteries9040193

[33] **Arumugam Manthiram.** (2020). A reflection on lithium-ion battery cathode chemistry. Nature Communications, 11(1), 1–9. https://doi.org/10.1038/s41467-020-15355-0

[34] **Sebastian, M.** (2016). The Influence of Diphenyl Octyl Phosphate on the Electrode Interfaces of Lithium-Ion Batteries. https://doi.org/10.13140/RG.2.2.12801.76641

[35] **Needham, S. A., Wang, G. X., Liu, H. K., Drozd, V. A., & Liu, R. S.** (2007). Synthesis and electrochemical performance of doped LiCoO~~2~~ materials. Journal of Power Sources, 174(2), 828–831. https://doi.org/10.1016/j.jpowsour.2007.06.228

[36] **Berg, H.** (2015). Batteries for Electric Vehicles: Materials and Electrochemistry. Cambridge University Press. pp 100–111

[37] **Mizushima, K., Jones, P.C., Wiseman, P.J. and Goodenough, J.B.** (1980) Materials Research Bulletin, 15, 783-789. https://doi.org/10.1016/0025-5408(80)90012-4

[38] **Xia, H., Meng, S., Lu, L., & Ceder, G.** (2007). Electrochemical Behavior and Li Diffusion Study of $LiCoO_2$ Thin Film Electrodes Prepared by PLD.

[39] **Zubi, G., Dufo-López, R., Carvalho, M., & Pasaoglu, G. (2018).** The lithium-ion battery: State of the art and future perspectives. Renewable and Sustainable Energy Reviews, 89, 292–308. https://doi.org/10.1016/j.rser.2018.03.002

[40] **Chung, K. Y., Ryu, C.-W., & Kim, K.-B.** (2005). Onset mechanism of jahn-teller distortion in 4 V LiMn~~2~~O ~~4~~ and its suppression by LiM~~0.05~~Mn~~1.95~~O ~~4~~(M = Co, Ni) coating. Journal of the Electrochemical Society, 152(4), A791–A795. https://doi.org/10.1149/1.1870755

[41] **Feng, X., Zhang, J., & Yin, L.** (2016). Effect of AlP coating on electrochemical properties of LiMn~~2~~O~~4~~ cathode material for lithium ion battery. Materials Research Bulletin, 74, 421–424. https://doi.org/10.1016/j.materresbull.2015.11.008

[42] **Tyagi, R., Lanjan, A., & Srinivasan, S.** (2022). Co-doping strategies to improve the electrochemical properties of lixmn2O4 cathodes for li-ion batteries. ChemElectroChem, 9(3). https://doi.org/10.1002/celc.20211626

[43] **Sun C, Rajasekhara S, Goodenough JB, Zhou** F. Monodisperse porous LiFePO4 microspheres for a high power Li-ion battery cathode. J Am Chem Soc. 2011 Feb 23;133(7):2132-5. doi: 10.1021/ja1110464. Epub 2011 Jan 26. PMID: 21268579.

[44] **Zhang B, He Y, Gao H, Wang X, Liu J, Xu H, Wang L, He X.** Unraveling the doping mechanisms in lithium iron phosphate. Energy Materials. 2022; 2(2): 200013. http://dx.doi.org/10.20517/energymater.2022.12

[45] **Saji, V. S., Kim, Y.-S., Kim, T.-H., Cho, J., & Song, H.-K.** (2011). One-dimensional (1D) nanostructured and nanocomposited LiFePO4: its perspective advantages for cathode materials of lithium ion batteries. PHYSICAL CHEMISTRY CHEMICAL PHYSICS, 13(43), 19226–19237. https://doi.org/10.1039/c1cp22818h

[46] **Al-Samet, M. A. M. M., & Burgaz, E.** (2023). Improving the lithium-ion diffusion and electrical conductivity of LiFePO4 cathode material by doping magnesium and multi-walled carbon nanotubes. Journal of Alloys and Compounds, 947. https://doi.org/10.1016/j.jallcom.2023.169680

[47] **Ahsan, Z., Bo, D., Cai, Z., Wen, C., Yang, W., Ma, Y., Zhang, S., Song, G., & Javed, M. S.** (2024). Recent Progress in Capacity Enhancement of LiFePO4 Cathode For Li-ion Batteries. Journal of Electrochemical Energy Conversion and Storage, Preprints, 1–54. https://doi.org/10.1115/1.4047222

[48] **Wani, T. A., & Suresh, G.** (2021). A comprehensive review of LiMnPO4 based cathode materials for lithium-ion batteries: current strategies to improve its performance. Journal of Energy Storage, 44. https://doi.org/10.1016/j.est.2021.103307

[49] **Bianchini, M., Roca-Ayats, M., Hartmann, P., Brezesinski, T., & Janek, J.** (2019). There and Back Again-The Journey of LiNiO2 as a Cathode Active Material. ANGEWANDTE CHEMIE-INTERNATIONAL EDITION, 58(31), 10434–10458. https://doi.org/10.1002/anie.201812472

[50] **Luo, B., Jiang, B., Peng, P., Huang, J., Chen, J., Li, M., Chu, L., & Li, Y.** (2019). Improving the electrochemical performance of LiNi1/3Co1/3Mn1/3O2 cathode material via tungsten modification. Electrochimica Acta, 297, 398–405. https://doi.org/10.1016/j.electacta.2018.11.202

[51] **Jow, T. R., Marx, M. B., & Allen, J. L.** (2012). Distinguishing Li ^^+^^ charge transfer kinetics at NCAelectrolyte and graphite-electrolyte interfaces, and NCAelectrolyte and LFPelectrolyte interfaces in Li-ion cells. Journal of the Electrochemical Society, 159(5), A604–A612. https://doi.org/10.1149/2.079205jes

[52] **Purwanto, A., Yudha, C.S., Ubaidillah, U., Widiyandari, H., Ogi, T., & Haerudin, H.** (2018). NCA cathode material: synthesis methods and performance enhancement efforts. Materials Research Express, 5.

[53] **Chen, Y., Song, S., Zhang, X., & Liu, Y.** (2019). The challenges, solutions and development of high energy Ni-rich NCM/NCA LiB cathode materials. Journal of Physics: Conference Series, 1347(1). https://doi.org/10.1088/1742-6596/1347/1/012012

[54] **Ziraki, S., Moaddeli, M., Kanani, M., & Hashemi, B.** (2022). Sensitivity of structural and electronic properties of Li-ion battery cathode materials to Hubbard U correction: an efficient first-principle approach. Physica Scripta, 97.

[55] **Li, X., Fan, Y., Johannessen, B., Xu, X., See, K. W., & Pang, W. K.** (2024). O3-Type Cathodes for Sodium-Ion Batteries: Recent Advancements and Future Perspectives. BATTERIES & SUPERCAPS. https://doi.org/10.1002/batt.202300618

[56] **Christian M. Julien, Alain Mauger, Karim Zaghib, & Henri Groult.** (2014). Comparative Issues of Cathode Materials for Li-Ion Batteries. Inorganics, 2(1), 132–154. https://doi.org/10.3390/inorganics2010132

[57] **Schipper, F., Erickson, E. M., Erk, C., Ji-Yong Shin, Chesneau, F. F., & Aurbach, D.** (2017). Review--Recent Advances and Remaining Challenges for Lithium Ion Battery Cathodes I. Nickel-Rich, LiNixCoyMnzO2. Journal of The Electrochemical Society, 164(1), A6220–A6228. https://doi.org/10.1149/2.0351701jes

[58] **Xia, Y., Zheng, J., Wang, C., & Gu, M.** (2018). Designing principle for Ni-rich cathode materials with high energy density for practical applications. Nano Energy, 49, 434–452. https://doi.org/10.1016/j.nanoen.2018.04.062

[59] **Lu, Y., Zhang, Y., Zhang, Q., Cheng, F., & Chen, J.** (2020). Recent advances in Ni-rich layered oxide particle materials for lithium-ion batteries. Particuology, 53, 1–11. https://doi.org/10.1016/j.partic.2020.09.004

[60] **Aryal, S., Kahvecioglu, O., Durham, J. L., Lipson, A. L., & Pupek, K. Z.** (2021). Roles of Mn and Co in Ni-rich layered oxide cathodes synthesized utilizing a Taylor Vortex Reactor. Electrochimica Acta. https://doi.org/10.1016/j.electacta.2021.138929

[61] **Manthiram, A., Knight, J. C., Myung, S.-T., Oh, S.-M., & Sun, Y.-K. (2016).** Nickel-Rich and Lithium-Rich Layered Oxide Cathodes: Progress and Perspectives. Advanced Energy Materials, 6(1). https://doi.org/10.1002/aenm.201501010

[62] **Choi, D., Shamim, N., Crawford, A., Huang, Q., Vartanian, C. K., Viswanathan, V. V., Paiss, M. D., Alam, M. J. E., Reed, D. M., & Sprenkle, V. L.** (2021). Li-ion battery technology for grid application. Journal of Power Sources, 511. https://doi.org/10.1016/j.jpowsour. 2021.230419

[63] **Ahangari, M., Szalai, B., Lujan, J., Zhou, M., & Luo, H.** (2024). Advancements and Challenges in High-Capacity Ni-Rich Cathode Materials for Lithium-Ion Batteries. Materials (1996-1944), 17(4), 801. https://doi.org/10.3390/ma17040801

[64] **Noh, H.-J., Youn, S., Yoon, C. S., & Sun, Y.-K.** (2013). Comparison of the structural and electrochemical properties of layered Li[NixCoyMnz]O2 (x = 1/3, 0.5, 0.6, 0.7, 0.8 and 0.85) cathode material for lithium-ion batteries. Journal of Power Sources, 233, 121–130. https://doi.org/10.1016/j.jpowsour.2013.01.063

[65] **Hou, P., Yin, J., Ding, M., Huang, J., & Xu, X.** (2017). Surface/Interfacial Structure and Chemistry of High-Energy Nickel-Rich Layered Oxide Cathodes: Advances and Perspectives. SMALL, 13(45), 1701802. https://doi.org/10.1002/smll.201701802

[66] **Park, K.-J., Hwang, J.-Y., Ryu, H.-H., Sun, Y.-K., Maglia, F., Kim, S.-J., Lamp, P., & Yoon, C. S.** (2019). Degradation Mechanism of Ni-Enriched NCA Cathode for Lithium Batteries: Are Microcracks Really Critical? ACS Energy Letters, 4(6), 1394–1400. https://doi.org/10.1021/acsenergylett.9b00733

[67] **Jie Chen, Huiping Yang, Tianhao Li, Chaoyang Liu, Hui Tong, Jiaxin Chen, Zengsheng Liu, Lingfeng Xia, Zhaoyong Chen, Junfei Duan, & Lingjun Li.** (2019). The Effects of Reversibility of H2-H3 Phase Transition on Ni-Rich Layered Oxide Cathode for High-Energy Lithium-Ion Batteries. Frontiers in Chemistry, 7. https://doi.org/10.3389/fchem.2019.00500

[68] **Wu, F., Liu, N., Chen, L., Su, Y., Tan, G., Bao, L., Zhang, Q., Lu, Y., Wang, J., Chen, S., & Tan, J.** (2019). Improving the reversibility of the H2-H3 phase transitions for layered Ni-rich oxide cathode towards retarded structural transition and enhanced cycle stability. Nano Energy, 59, 50–57. https://doi.org/10.1016/j.nanoen.2019.02.027

[69] **Zhang, S. S.** (2020). Problems and their origins of Ni-rich layered oxide cathode materials. Energy Storage Materials, 24, 247–254. https://doi.org/10.1016/j.ensm.2019.08.013

[70] **Malik, M., Chan, K. H., & Azimi, G.** (2022). Review on the synthesis of LiNixMnyCo1-x-yO2 (NMC) cathodes for lithium-ion batteries. Materials Today Energy, 28. https://doi.org/10.1016/j.mtener.2022.101066

[71] **Song, Y., Li, B., Ge, L., Zhou, L., Qiu, Z., Li, X., Yan, Z., Xue, Q., Xing, W., Cui, Y., Geng, L., Tang, Y., Nan, J., Wu, W., & Xu, H.** (2024). Li/Ni Intermixing: The Real Origin of Lattice Oxygen Stability in Co-Free Ni-Rich Cathode Materials. Advanced Energy Materials, 14(7). https://doi.org/10.1002/aenm.202303207

[72] **Jingxi Li, Gemeng Liang, Wei Zheng, Shilin Zhang, Kenneth Davey, Wei Kong Pang, & Zaiping Guo.** (2023). Addressing cation mixing in layered structured cathodes for lithium-ion batteries: A critical review. Nano Materials Science, 5(4), 404–420. https://doi.org/10.1016/j.nanoms.2022.09.001

[73] **Teichert, P., Eshetu, G. G., Jahnke, H., & Figgemeier, E.** (2020). Degradation and Aging Routes of Ni-Rich Cathode Based Li-Ion Batteries. BATTERIES-BASEL, 6(1), 8. https://doi.org/10.3390/batteries6010008

[74] **Chen, Z., Wang, J., Chao, D., Baikie, T., Bai, L., Chen, S., Zhao, Y., Sum, T. C., Lin, J., & Shen, Z.** (2016). Hierarchical Porous LiNi1/3Co1/3Mn1/3O2 Nano-/Micro Spherical Cathode Material: Minimized Cation Mixing and Improved Li+ Mobility for Enhanced Electrochemical Performance. SCIENTIFIC REPORTS, 6, 25771. https://doi.org/10.1038/srep25771

[75] **Julien, C., Mauger, A., Zaghib, K., & Groult, H.** (2016). Optimization of Layered Cathode Materials for Lithium-Ion Batteries. Materials (1996-1944), 9(7), 595. https://doi.org/10.3390/ma9070595

[76] **Yamamoto, Y., Ohtsuka, M., Azuma, Y., Takahashi, T., & Muto, S.** (2018). Cation mixing in LiNi0.8Co0.15Al0.05O2 positive electrode material studied using high angular resolution electron channeling X-ray spectroscopy. Journal of Power Sources, 401, 263–270. https://doi.org/10.1016/j.jpowsour.2018.08.100

[77] **Lu, H., Zhou, H., Svensson, A. M., Fossdal, A., Sheridan, E., Lu, S., & Vullum-Bruer, F.** (2013). High capacity li[ni0.8co0.1mn0.1]o2 synthesized by sol–gel and co-precipitation methods as cathode materials for lithium-ion batteries. Solid State Ionics, 249–250, 105–111. https://doi.org/10.1016/j.ssi.2013.07.023

[78] **L. Tan, H. Liu,** High rate chargeedischarge properties of LiNi1/3Co1/3Mn1/3O2 synthesized via a low temperature solid-state method, Solid State Ion 181 (2010) 1530e1533, https://doi.org/10.1016/j.ssi.2010.08.016.

[79] **Elong, K., Firdaus Kasim, M., Azahidi, A., & Osman, Z.** (2023). Lini0.3Mn0.3Co0.3O2 (NMC 111) cathode material synthesize via combustion method: Effect of combustion fuel on structure, morphology and their electrochemical performances. Materials Today: Proceedings. https://doi.org/10.1016/j.matpr.2023.02.283

[80] **Jayaraman, V. K., Kannan, P., Gangadharappa, V. A., Kumaresan, H. N., & Prakash, A. S. (2023).** An alternative approach for NMC-based Li-ion battery cathode production and its techno-economic analysis. Clean Technologies and Environmental Policy, 26(2), 319–330. https://doi.org/10.1007/s10098-023-02616-x

[81] **Almazrouei, M., Park, S., Houck, M., De Volder, M., Hochgreb, S., & Boies, A.** (2024). Synthesis pathway of layered-oxide cathode materials for lithium-ion batteries by spray pyrolysis. ACS Applied Materials & Interfaces, 16(26), 33633–33646. https://doi.org/10.1021/acsami.4c06503

[82] **Li, Y., Li, X., Wang, Z., Guo, H., & Wang, J.** (2018). Spray pyrolysis synthesis of nickel-rich layered cathodes lini 1−2 x CO x mn x O_2 (x = 0.075, 0.05, 0.025) for lithium-ion batteries. Journal of Energy Chemistry, 27(2), 447–450. https://doi.org/10.1016/j.jechem.2017.11.025

[83] **Widiyandari, H., Sukmawati, A. N., Sutanto, H., Yudha, C., & Purwanto, A.** (2019). Synthesis of lini0.8mn0.1co0.1O2 cathode material by hydrothermal method for high energy density lithium ion battery. Journal of Physics: Conference Series, 1153, 012074. https://doi.org/10.1088/1742-6596/1153/1/012074

[84] **Essehli, R., Parejiya, A., Muralidharan, N., Jafta, C. J., Amin, R., Dixit, M. B., Bai, Y., Liu, J., & Belharouak, I.** (2022). Hydrothermal synthesis of co-free NMA cathodes for high performance li-ion batteries. Journal of Power Sources, 545, 231938. https://doi.org/10.1016/j.jpowsour.2022.231938

[85] **Le Thi, T., Phan Van, T., Nguyen Van, B., To Van, N., Nguyen Van, T., Doan, T. P., Ngo, T. L., Vu, N. H., Nguyen, T.-T., Nguyen, H. N., Anh Duy, N. V., & Dang, M. T.** (2023). Modified coprecipitation synthesis of nickel-rich NMC (li1.0ni0.6mn0.2co0.2O2) for lithium-ion batteries: A simple, cost-effective, environmentally friendly method. ACS Omega, 8(48), 45414–45427. https://doi.org/10.1021/acsomega.3c04717

[86] **Vaccari, M., Barontini, F., Bertei, A., Puccini, M., & Tognotti, L.** (2023). Co-precipitation of Cathode Active Materials Precursors in Lithium-ion Batteries Recycling: Experiments and Modeling. The Italian Association of Chemical Engineering, 99.

[87] **Entwistle, T., Sanchez-Perez, E., Murray, G. J., Anthonisamy, N., & Cussen, S. A.** (2022). Co-precipitation synthesis of nickel-rich cathodes for Li-Ion Batteries. Energy Reports, 8, 67–73. https://doi.org/10.1016/j.egyr.2022.06.110

[88] **Mishina, N.E., Akhmatov, A.A., Zilberman, B.Y. et al.** Solubility and coprecipitation of barium and strontium nitrates in HNO3 solutions and multicomponent systems. Radiochemistry 52, 523–529 (2010). https://doi.org/10.1134/S1066362210050140

[89] **Sarode, A. L., Wang, P., Obara, S., & Worthen, D. R.** (2014). Supersaturation, nucleation, and crystal growth during single- and biphasic dissolution of amorphous solid dispersions: Polymer effects and implications for oral bioavailability enhancement of poorly water soluble drugs. European Journal of Pharmaceutics and Biopharmaceutics, 86(3), 351–360. https://doi.org/10.1016/j.ejpb.2013.10.005

[90] **Ertl, G., L., Knozinger, H. & Weitkamp, J.** (2008). Preparation of Solid Catalysts. 62-63. Grünstad: Wiley-VCH

[91] **Mokhtari Motameni Shirvan, M., Famili, M. H., & Golbang, A.** (2016). A review on the application of nucleation theories in thermoplastic foams. Plastic and Polymer Technology, 4(0), 11. https://doi.org/10.14355/papt.2016.04.002

[92] **Aspillaga, L., Jan Bautista, D., Daluz, S. N., Hernandez, K., Renta, J. A., & Lopez, E. C.** (2023). Nucleation and crystal growth: Recent advances and future trends. ASEC 2023, 22. https://doi.org/10.3390/asec2023-15281

[93] **Para, M. L., Alidoost, M., Shiea, M., Boccardo, G., Buffo, A., Barresi, A. A., & Marchisio, D.** (2022). A modelling and experimental study on the co-precipitation of Ni0.8MN0.1Co0.1(OH)2 as precursor for Battery Cathodes. Chemical Engineering Science, 254, 117634. https://doi.org/10.1016/j.ces.2022.117634

[94] **Huang, B., Cheng, L., Li, X., Zhao, Z., Yang, J., Li, Y., Pang, Y., & Cao, G.** (2022). Layered cathode materials: Precursors, synthesis, microstructure, electrochemical properties, and Battery Performance. Small, 18(20). https://doi.org/10.1002/smll.202107697

[95] **van Westen, T., & Groot, R. D.** (2018). Effect of temperature cycling on Ostwald ripening. Crystal Growth & Design, 18(9), 4952–4962. https://doi.org/10.1021/acs.cgd.8b00267

[96] **Feng, Z., Barai, P., Gim, J., Yuan, K., Wu, Y. A., Xie, Y., Liu, Y., & Srinivasan, V.** (2018). In situ monitoring of the growth of nickel, manganese, and cobalt hydroxide precursors during co-precipitation synthesis of Li-ion cathode materials. Journal of The Electrochemical Society, 165(13). https://doi.org/10.1149/2.0511813jes

[97] **Yang, Y., Xu, S., Xie, M., He, Y., Huang, G., & Yang, Y.** (2015). Growth mechanisms for spherical mixed hydroxide agglomerates prepared by co-precipitation method: A case of ni1/3co1/3mn1/3(oh)2. Journal of Alloys and Compounds, 619, 846–853. https://doi.org/10.1016/j.jallcom.2014.08.152

[98] **Xu, C., Guan, S., Li, L., Sun, C., An, B., & Geng, X.** (2021). Electrochemical Properties of LiNi0.6Co0.2Mn0.2O2 Cathode Materials Prepared with Different Ammonia Content. Coatings, 11(8), 932. https://doi.org/10.3390/coatings11080932

[99] **Zhang, L., Wu, B., Li, N., Mu, D., Zhang, C., & Wu, F.** (2013). Rod-like hierarchical nano/micro li1.2ni0.2mn0.6o2 as high performance cathode materials for lithium-ion batteries. Journal of Power Sources, 240, 644–652. https://doi.org/10.1016/j.jpowsour.2013.05.019

[100] **Gan, Y., Baak, J. P., Chen, T., Ye, H., Liao, W., Lv, H., Wen, C., & Zheng, S.** (2023). Supersaturation and precipitation applicated in Drug Delivery Systems: Development Strategies and Evaluation Approaches. Molecules, 28(5), 2212. https://doi.org/10.3390/molecules28052212

[101] **Ding, Y., Mu, D., Wu, B., Zhao, Z., & Wang, R.** (2020). Controllable synthesis of spherical precursor NI0.8Co0.1Mn0.1(OH)2 for nickel-rich cathode material in Li-Ion Batteries. Ceramics International, 46(7), 9436–9445. https://doi.org/10.1016/j.ceramint.2019.12.204

[102] **Park, J., Park, S., Beak, M., Jeong, S., & Kwon, K.** (2022). Impacts of residual electrolyte components of spent lithium-ion batteries on the physical/electrochemical properties of resynthesized cathode active materials. Journal of Cleaner Production, 379, 134570. https://doi.org/10.1016/j.jclepro.2022.134570

[103] **Bizzotto, F., Dachraoui, W., Grissa, R., Zhao, W., Pagani, F., Querel, E., Kühnel, R.-S., & Battaglia, C.** (2023). Modification of NMC811 with titanium for enhanced cycling and high-voltage stability. Electrochimica Acta, 462, 142758. https://doi.org/10.1016/j.electacta.2023.142758

[104] **Skvortsova, I. A., Orlova, E. D., Boev, A. O., Aksyonov, D. A., Moiseev, I., Pazhetnov, E. M., Savina, A. A., & Abakumov, A. M.** (2023). Comprehensive analysis of boron-induced modification in lini0.8mn0.1co0.1o2 positive electrode material for lithium-ion batteries. Journal of Power Sources, 583, 233571. https://doi.org/10.1016/j.jpowsour.2023.233571

[105] **Lipson, A. L., Ross, B. J., Durham, J. L., Liu, D., LeResche, M., Fister, T. T., Liu, L., & Kim, K.** (2021). Stabilizing NMC 811 Li-ion battery cathode through a rapid coprecipitation process. ACS Applied Energy Materials, 4(2), 1972–1977. https://doi.org/10.1021/acsaem.0c03112

[106] **Liu, T., Yu, L., Lu, J., Zhou, T., Huang, X., Cai, Z., Dai, A., Gim, J., Ren, Y., Xiao, X., Holt, M. V., Chu, Y. S., Arslan, I., Wen, J., & Amine, K.** (2021). Rational design of mechanically robust ni-rich cathode materials via concentration gradient strategy. Nature Communications, 12(1). https://doi.org/10.1038/s41467-021-26290-z

[107] **B. Zhu, Z. Xu, Y. Ning, G. Wei, J. Qu,** Managing ammonia-alkali balance to control precursor characteristics in co-precipitation process for enhanced electrochemical performance of nickel-rich cathode materials, Solid State Sci. 142 (2023), 107224, https://doi.org/10.1016/j.solidstatesciences.2023.107224.

[108] **Baldan,** A. Review Progress in Ostwald ripening theories and their applications to nickel-base superalloys Part I: Ostwald ripening theories . Journal of Materials Science 37, 2171–2202 (2002). https://doi.org/10.1023/A:1015388912729

[109] **Tahri, Y., Kožíšek, Z., Gagnière, E., Chabanon, E., Bounahmidi, T., & Mangin, D.** (2016). Modeling the Competition between Polymorphic Phases: Highlights on the Effect of Ostwald Ripening.

[110] **Hwa Lee, S., Young Kwon, K., Kil Choi, B., & Deog Yoo, H.** (2022). A Kinetic descriptor to optimize co-precipitation of nickel-rich cathode precursors for lithium-ion batteries. Journal of Electroanalytical Chemistry, 924, 116828. https://doi.org/10.1016/j.jelechem.2022.116828

[111] **Ratchagar, V., Muralidharan, M., Silambarasan, M., Jagannathan, K., Kamaraj, P., Subbiah, S. K., Vivekanand, P. A., Periyasami, G., Rahaman, M., Karthikeyan, P., & Gonfa, G.** (2023). COPRECIPITATION methodology synthesis of cobalt-oxide nanomaterials influenced by ph conditions: Opportunities in optoelectronic applications. International Journal of Photoenergy, 2023, 1–9. https://doi.org/10.1155/2023/2493231

[112] **Liu, P., Yang, X., Xiao, L. et al.** Preparation of Ternary Precursor Derived from Spent LiNixCoyMn1−x−yO_2 Materials. JOM 71, 4492–4499 (2019). https://doi.org/10.1007/s11837-019-03789-x

[113] **Van Bommel A. and Dahn J. R.,** "Analysis of the growth mechanism of coprecipitated spherical and dense nickel, manganese, and cobalt-containing hydroxides in the presence of aqueous ammonia," Chem. Mater., vol. 21, no. 8, pp. 1500–1503, 2009, doi: 10.1021/cm803144d.

[114] **Shen, Y., Wu, Y., Xue, H., Wang, S., Yin, D., Wang, L., & Cheng, Y.** (2021). Insight into the coprecipitation-controlled crystallization reaction for preparing lithium-layered oxide cathodes. ACS Applied Materials & Interfaces, 13(1), 717–726. https://doi.org/10.1021/acsami.0c19493

[115] **Hendrickx, M., Paulus, A., Kirsanova, M. A., Van Bael, M. K., Abakumov, A. M., Hardy, A., & Hadermann, J.** (2022). The influence of synthesis method on the local structure and electrochemical properties of Li-rich/MN-rich NMC cathode materials for Li-Ion Batteries. Nanomaterials, 12(13), 2269. https://doi.org/10.3390/nano12132269

[116] **Vu D. L. and Lee J. won ,** "Properties of LiNi0.8Co0.1Mn0.1O2 as a high energy cathode material for lithiumion batteries," Korean J. Chem. Eng., vol. 33, no. 2, pp. 514–526, 2016, doi: 10.1007/s11814-015-0154-3.

[117] **D. Wang, I. Belharouak, G.M. Koenig, G. Zhou, K. Amine,** Growth mechanism of Ni0. 3Mn0. 7CO3 precursor for high capacity Li-ion battery cathodes, J. Mater. Chem. 21 (2011) 9290e9295, https://doi.org/10.1039/C1JM11077B.

[118] **Zhang S, Deng C., Fu B.L., Yang S.Y., Ma L.,** Synthetic optimization of spherical Li[Ni1/3Mn1/3Co1/3]O2 prepared by a carbonate co-precipitation method, Powder Technol. 198 (2010) 373–380, https://doi.org/10.1016/j.powtec.2009.12.002

[119] **L. Xu, F. Zhou, J. Kong, H. Zhou, Q. Zhang, Q. Wang, G. Yan,** Influence of precursor phase on the structure and electrochemical properties of Li (Ni0.6Mn0.2Co0.2)O2 cathode materials, Solid State Ion 324 (2018) 49–58, https://doi.org/10.1016/j.ssi.2018.06.010.

[120] **Fakhrudin, M., & Kartini, E.** (2023). NMC cathode precursor synthesis by hydroxide co-precipitation method: A mini review. AIP Conference Proceedings, 2932, 020007. https://doi.org/10.1063/5.0174823

[121] **Bezerra, D. M., & Assaf, E. M.** (2018). Influence of the preparation method on the structural properties of mixed metal oxides. Science and Technology of Materials, 30(3), 166–173. https://doi.org/10.1016/j.stmat.2018.07.001

[122] **Zhu, Q., Xiao, H., Chen, A., Geng, S., & Huang, Q.** (2019). CFD study on double- to single-loop flow pattern transition and its influence on macro mixing efficiency in fully baffled tank stirred by a rushton turbine. Chinese Journal of Chemical Engineering, 27(5), 993–1000. https://doi.org/10.1016/j.cjche.2018.10.002

[123] **Montante, G., Brucato, A., Lee, K. C., & Yianneskis, M.** (1999). An experimental study of double-to-single-loop transition in stirred vessels. The Canadian Journal of Chemical Engineering, 77(4), 649–659. https://doi.org/10.1002/cjce.5450770405

[124] **Zhu, Q., Xiao, H., Zhang, R., Geng, S., Huang, Q.,** "Effect of impeller type on preparing spherical and dense Ni1-x-yCoxMny(OH)2 precursor via continuous co-precipitation in pilot scale A case of Ni0,6Co0,2Mn0,2(OH)2," Electrochimica Acta, vol. 318, pp. 1-13, 2019. doi.org/10.1016/j.electacta.2019.06.008

[125] **Alpay, B. C., & Keles, O.** (2023). Effect of impeller design on the properties of Li1.03Ni0.8Mn0.1Co0.1O2 cathode material synthesized via co-precipitation method. Journal of Alloys and Compounds, 947, Makale 169583. https://doi.org/10.1016/j.jallcom.2023.169583

[126] **Ngoepe, N., Gutierrez, A., Barai, P., Chen, J., Ngoepe, P. E., & Croy, J. R.** (2021). The effects of process parameters on the properties of manganese-rich carbonate precursors: A study of co-precipitation synthesis using semi-batch reactors. Chemical Engineering Science, 241, 116694. https://doi.org/10.1016/j.ces.2021.116694

[127] **Vidal Laveda, J., Low, J. E., Pagani, F., Stilp, E., Dilger, S., Baran, V., Heere, M., & Battaglia, C.** (2019). Stabilizing capacity retention in NMC811/graphite full cells via TMSPI electrolyte additives. ACS Applied Energy Materials, 2(10), 7036–7044. https://doi.org/10.1021/acsaem.9b00727

[128] **Wang, E., Ye, X., Zhang, B., Qu, B., Guo, J., & Zheng, S.** (2024). Enhancing the stability of 4.6 v LiCoO2 cathode material via gradient doping. Nanomaterials, 14(2), 147. https://doi.org/10.3390/nano14020147

[129] **Ouyang, C. Y., Shi, S. Q., & Lei, M. S.** (2009). Jahn–teller distortion and electronic structure of LIMN2O4. Journal of Alloys and Compounds, 474(1–2), 370–374. https://doi.org/10.1016/j.jallcom.2008.06.123

[130] **Ghosh, S., charjee, U. B., Bhowmik, S., & Martha, S. K.** (2021). A review on high-capacity and high-voltage cathodes for next-generation lithium-ion batteries. Journal of Energy and Power Technology, 4(1), 1–1. https://doi.org/10.21926/jept.2201002

[131] **Wang, B., Son, S.-B., Badami, P., Trask, S. E., Abraham, D., Qin, Y., Yang, Z., Wu, X., Jansen, A., & Liao, C.** (2023). Understanding and mitigating the dissolution and delamination issues encountered with high-voltage lini0.5mn1.5o4. Batteries, 9(9), 435. https://doi.org/10.3390/batteries9090435

[132] **Liu, Z., Yu, A., & Lee, J. Y.** (1999). Synthesis and characterization of lini1−x−ycoxmnyo$_2$ as the cathode materials of secondary lithium batteries. Journal of Power Sources, 81–82, 416–419. https://doi.org/10.1016/s0378-7753(99)00221-9

[133] **Ohzuku, T., & Makimura, Y.** (2001). Layered lithium insertion material of LiCo1/3NI1/3MN1/3O$_2$ for lithium-ion batteries. Chemistry Letters, 30(7), 642–643. https://doi.org/10.1246/cl.2001.642

[134] **Liang, C., Kong, F., Longo, R. C., KC, S., Kim, J.-S., Jeon, S., Choi, S., & Cho, K.** (2016). Unraveling the origin of instability in ni-rich Lini1–2xcoxmnxO$_2$ (NCM) cathode materials. The Journal of Physical Chemistry C, 120(12), 6383–6393. https://doi.org/10.1021/acs.jpcc.6b00369

[135] **Yousuf, S., Mridha, M. M., & Magri, R.** (2024). Structures and electronic states of nickel-rich oxides for lithium ion batteries. Materials Advances, 5(5), 2069–2087. https://doi.org/10.1039/d3ma00906h

[136] **Chen, J., Yang, H., Li, T., Liu, C., Tong, H., Chen, J., Liu, Z., Xia, L., Chen, Z., Duan, J., & Li, L.** (2019). The effects of reversibility of H2-H3 phase transition on NI-rich layered oxide cathode for high-energy lithium-ion batteries. Frontiers in Chemistry, 7. https://doi.org/10.3389/fchem.2019.00500

[137] **Mikheenkova, A., Mukherjee, S., Hirsbrunner, M., Törnblom, P., Tai, C.-W., Segre, C. U., Ding, Y., Zhang, W., Asmara, T. C., Wei, Y., Schmitt, T., Rensmo, H., Duda, L., & Hahlin, M.** (2024). The role of oxygen in Automotive Grade Lithium-Ion Battery Cathodes: An atomistic survey of ageing. Journal of Materials Chemistry A, 12(4), 2465–2478. https://doi.org/10.1039/d3ta05516g

[138] **Shang, T., Gao, A., Xiao, D., Zhang, Q., Rong, X., Tang, Z., Lin, W., Lin, T., Meng, F., Li, X., Wen, Y., Wang, X., Su, D., Chen, Z., Hu, Y.-S., Li, H., Yu, Q., Zhang, Z., Wu, L., … Nan, C.-W.** (2024). An orbital strategy for regulating the jahn–teller effect. National Science Review, 11(9). https://doi.org/10.1093/nsr/nwae255

[139] **Ryu, H.H., Park, K.J., Yoon, C.S. , Sun, Y.K.** Capacity fading of Ni-rich Li [NixCoyMn1–x–y]O$_2$ ($0.6 \leq x \leq 0.95$) cathodes for high-energy-density lithium-ion batteries: bulk or surface degradation? Chem. Mater. 30 (2018) 1155–1163.

[140] **Cui, Z., Li, X., Bai, X., Ren, X., & Ou, X.** (2023). A comprehensive review of foreign-ion doping and recent achievements for nickel-rich cathode materials. Energy Storage Materials, 57, 14–43. https://doi.org/10.1016/ j.ensm.2023.02.003

[141] **Dose, W. M., Li, W., Temprano, I., O'Keefe, C. A., Mehdi, B. L., De Volder, M. F., & Grey, C. P.** (2022). Onset potential for electrolyte oxidation and NI-rich cathode degradation in lithium-ion batteries. ACS Energy Letters, 7(10), 3524–3530. https://doi.org/10.1021/acsenergylett.2c01722

[142] **Chu, Y., Mu, Y., Zou, L., Wu, F., Yang, L., Feng, Y., & Zeng, L.** (2024). Oxygen release in NI-rich layered cathode for lithium-ion batteries: Mechanisms and mitigating strategies. ChemElectroChem, 11(14). https://doi.org/10.1002/celc.202300653

[143] **Liu, W., Oh, P., Liu, X., Lee, M., Cho, W., Chae, S., Kim, Y., & Cho, J.** (2015). Nickel-rich layered lithium transition-metal oxide for high-energy Lithium-Ion Batteries. Angewandte Chemie International Edition, 54(15), 4440–4457. https://doi.org/10.1002/anie.201409262

[144] **Jung, R., Metzger, M., Maglia, F., Stinner, C., & Gasteiger, H. A.** (2017). Oxygen release and its effect on the cycling stability of $Li_{x}Ni_{y}Mn_{z}Co_{z}O_{2}$ (nmc) cathode materials for Li-Ion Batteries. Journal of The Electrochemical Society, 164(7). https://doi.org/10.1149/2.0021707jes

[145] **Yin, S., Deng, W., Chen, J., Gao, X., Zou, G., Hou, H., & Ji, X.** (2021). Fundamental and solutions of microcrack in NI-rich layered oxide cathode materials of lithium-ion batteries. Nano Energy, 83, 105854. https://doi.org/10.1016/j.nanoen.2021.105854

[146] **Amatucci, G. G., Tarascon, J. M., and Klein, L. C.** CoO2, The End Member of the LixCoO2 Solid Solution, J. Electrochem. Soc. 143, 1114 (1996).

[147] **Cai, C., Zhang, D., Zhang, Q., Chen, K., Hua, W., Peng, C., & Xue, D.** (2023). Origin of oxygen-redox and transition metals dissolution in ni-rich lixni0.8co0.1mn0.1o2 cathode. The Journal of Chemical Physics, 158(11). https://doi.org/10.1063/5.0139471

[148] **Adenusi, H., Chass, G. A., Passerini, S., Tian, K. V., & Chen, G.** (2023). Lithium batteries and the solid electrolyte interphase (SEI)—Progress and outlook. Advanced Energy Materials, 13(10). https://doi.org/10.1002/aenm.202203307

[149] **Yang, C.-K., Qi, L.-Y., Zuo, Z., Wang, R.-N., Ye, M., Lu, J., & Zhou, H.-H.** (2016). Insights into the inner structure of high-nickel agglomerate as high-performance lithium-ion cathodes. Journal of Power Sources, 331, 487–494. https://doi.org/10.1016/j.jpowsour.2016.09.068

[150] **Liu, C., Roters, F. & Raabe, D.** Role of grain-level chemo-mechanics in composite cathode degradation of solid-state lithium batteries. Nat Commun 15,7970(2024). https://doi.org/10.1038/s41467-024-52123-w

[151] **Liao, Q.-T., Guo, S.-J., Qi, M.-Y., Zhang, S.-D., Ma, P.-Z., Li, J.-Y., Cao, A.-M., & Wan, L.-J.** (2023). The Genesis and control of microcracks in nickel-rich cathode materials for lithium-ion batteries. Sustainable Energy & Fuels, 7(19), 4805–4824. https://doi.org/10.1039/d3se00844d

[152] **Liang, R., Yu, F.-D., Goh, K., Sun, G., Wang, M.-J., Zhu, H., Liu, X.-Y., Huang, G.-S., & Wang, Z.-B.** (2019). Influence of oxygen percentage in calcination atmosphere on structure and electrochemical properties of LiNi0.8Co0.1Mn0.1O2 cathode material for lithium-ion batteries. Ceramics International, 45(15), 18965–18971. https://doi.org/10.1016/j.ceramint.2019.06.134

[153] **Tiozzo, A., Ghaseminezhad, K., Mazzucco, A., Giuliano, M., Rocca, R., Dotoli, M., Nicol, G., Nervi, C., Baricco, M., & Sgroi, M. F.** (2024). Investigating the influence of three different atmospheric conditions during the synthesis process of NMC811 cathode material. Crystals, 14(2), 137. https://doi.org/10.3390/cryst14020137

[154] **Kim, S., Wang, R., Wiff, P., de Verthamon, G., Briand, F., & Prost, L.** (2022). Improving electrochemical properties of lini0.8mn0.1co0.1o2 cathode materials for lithium ion batteries by controlling calcination gas atmosphere. Solid State Ionics, 386, 116031. https://doi.org/10.1016/j.ssi.2022.116031

[155] **Ronduda, H., Zybert, M., Szczęsna-Chrzan, A., Trzeciak, T., Ostrowski, A., Szymański, D., Wieczorek, W., Raróg-Pilecka, W., & Marcinek, M.** (2020). On the sensitivity of the NI-rich layered cathode materials for Li-ion batteries to the different calcination conditions. Nanomaterials, 10(10), 2018. https://doi.org/10.3390/nano10102018

[156] **Song, M., Lee, D., Kim, J., Heo, Y., Nam, C., Ko, D., & Lim, J.** (2023). Chemical decomposition pathway of residual lithium carbonate of li-ion battery cathodes. Journal of Power Sources, 560, 232699. https://doi.org/10.1016/j.jpowsour.2023.232699

[157] **Mubarok, Moh. W., Fakhrudin, M., & Kartini, E.** (2023). The effect of lithium excess on synthesizing NMC 811 cathode material. AIP Conference Proceedings, 2932, 020006. https://doi.org/10.1063/5.0174701

[158] **Raju, K., Wheatcroft, L., Lai, M. C., Mahadevegowda, A., Piper, L. F., Ducati, C., Inkson, B. J., & De Volder, M.** (2024). Influence of cathode calendering density on the cycling stability of li-ion batteries using NMC811 single or poly crystalline particles. Journal of The Electrochemical Society, 171(8), 080519. https://doi.org/10.1149/1945-7111/ad6378

[159] **Sanad, M. M. S., Meselhy, N. K., El-Boraey, H. A., & Taghan, A.** (2023). Controllable engineering of new ZnAl2O4-decorated LiNi0·8Mn0·1Co0·1O2 cathode materials for high performance lithium-ion batteries. Journal of Materials Research and Technology, 23, 1528–1542. https://doi.org/https://doi.org/10.1016/j.jmrt.2023.01.102

[160] **Wu, F., Li, Q., Chen, L., Lu, Y., Su, Y., Bao, L., Chen, R., & Chen, S.** (2019). Use of CE to reinforce the interface of Ni-rich Lini0.8co0.1mn0.1O2 cathode materials for lithium-ion batteries under high operating voltage. ChemSusChem, 12(4), 935–943. https://doi.org/10.1002/cssc.201802304

[161] **Schipper, F., Bouzaglo, H., Dixit, M., Erickson, E. M., Weigel, T., Talianker, M., Grinblat, J., Burstein, L., Schmidt, M., Lampert, J., Erk, C., Markovsky, B., Major, D. T., & Aurbach, D**. (2017). From Surface Zro2 Coating to bulk zr doping by high temperature annealing of nickel-rich lithiated oxides and their enhanced electrochemical performance in lithium ion batteries. Advanced Energy Materials, 8(4). https://doi.org/10.1002/aenm.201701682

[162] **Lu, T., Wang, Z., He, J., Qiu, Y., Chen, X., Chen, A., Liu, X., He, L., Li, J., Sun, F., & Zhao, Z.** (2024). Enhancing the electrochemical performance of Lini0.8Co0.1Mn0.1O2 by surface modification with homemade high-purity hexagonal phase tungsten oxide nanoparticles. Journal of Alloys and Compounds, 1007, 176482. https://doi.org/10.1016/j.jallcom.2024.176482

[163] **Xiao, Z., Hu, C., Song, L., Li, L., Cao, Z., Zhu, H., Liu, J., Li, X., & Tang, F.** (2017). Modification research of lialo2-coated LiNi0.8Co0.1Mn0.1O2 as a cathode material for lithium-ion battery. Ionics, 24(1), 91–98. https://doi.org/10.1007/s11581-017-2178-7

[164] **Liang, H., Wang, Z., Guo, H., Wang, J., & Leng, J.** (2017). Improvement in the electrochemical performance of Lini0.8Co0.1Mn0.1O2 cathode material by LI2ZRO3 coating. Applied Surface Science, 423, 1045–1053. https://doi.org/10.1016/j.apsusc.2017.06.283

[165] **Xu, Y.-D., Xiang, W., Wu, Z.-G., Xu, C.-L., Li, Y.-C., Guo, X.-D., Lv, G.-P., Peng, X., & Zhong, B.-H.** (2018). Improving cycling performance and rate capability of ni-rich Lini0.8Co0.1Mn0.1O2 cathode materials by Li4ti5o12 coating. Electrochimica Acta, 268, 358–365. https://doi.org/10.1016/j.electacta.2018.02.049

[166] **Xiong, X., Wang, Z., Guo, H., Zhang, Q., & Li, X.** (2013). Enhanced electrochemical properties of lithium-reactive V2O5coated on the Lini0.8co0.1mn0.1o2cathode material for lithium ion batteries at 60 °C. J. Mater. Chem. A, 1(4), 1284–1288. https://doi.org/10.1039/c2ta 00678b

[167] **Huang, J., Fang, X., Wu, Y., Zhou, L., Wang, Y., Jin, Y., Dang, W., Wu, L., Rong, Z., Chen, X., & Tang, X.** (2018). Enhanced electrochemical performance of Lini0.8Co0.1Mn0.1O2 by surface modification with lithium-active MOO3. Journal of Electroanalytical Chemistry, 823, 359–367. https://doi.org/10.1016/j.jelechem.2018.06.035

[168] **Liu, Y., Tang, L., Wei, H., Zhang, X., He, Z., Li, Y., & Zheng, J.** (2019). Enhancement on structural stability of NI-rich cathode materials by in-situ fabricating dual-modified layer for lithium-ion batteries. Nano Energy, 65, 104043. https://doi.org/10.1016/j.nanoen.2019.104043

[169] **Zhang, M., Zhao, H., Tan, M., Liu, J., Hu, Y., Liu, S., Shu, X., Li, H., Ran, Q., Cai, J., & Liu, X.** (2019). Yttrium modified NI-rich Lini0.8Co0.1Mn0.1O2 with enhanced electrochemical performance as high energy density cathode material at 4.5 v high voltage. Journal of Alloys and Compounds, 774, 82–92. https://doi.org/10.1016/ j.jallcom. 2018.09.281

[170] **Wang, C., Peng, W., Li, Z., Liang, Y., Zhong, S., & Zhang, Q.** (2019). Synthesis and characterization of Nano SNO2 modification on lini0.8mn0.1ni0.1o2 cathode materials for lithium ion batteries. Frontiers in Energy Research, 7. https://doi.org/10.3389/fenrg.2019.00125

[171] **Liang, L., Hu, G., Jiang, F., & Cao, Y.** (2016). Electrochemical behaviours of SIO 2 -coated lini 0.8 co 0.1 mn 0.1 o 2 cathode materials by a novel modification method. Journal of Alloys and Compounds, 657, 570–581. https://doi.org/10.1016/j.jallcom.2015.10.177

[172] **Llanos, P. S., Ahaliabadeh, Z., Miikkulainen, V., Lahtinen, J., Yao, L., Jiang, H., Kankaanpää, T., & Kallio, T. M.** (2024). High voltage cycling stability of LIF-coated NMC811 electrode. ACS Applied Materials & Interfaces, 16(2), 2216–2230. https://doi.org/10.1021/acsami.3c14394

[173] **Zheng, S., Dou, A., Su, M., & Liu, Y.** (2020). Influence of nb doping on electrochemical performance of nanostructured cation disordered Li1+x/100ni1/2–x/100ti1/2–x/100nbx/100O2 composites cathode for Li-Ion Batteries. Journal of Nanoscience and Nanotechnology, 20(1), 452–459. https://doi.org/10.1166/jnn.2020.16884

[174] **Zhang, X., Jiang, W. J., Mauger, A., Qilu, Gendron, F., & Julien, C. M.** (2010). Minimization of the cation mixing in li1+x(nmc)1−xo2 as cathode material. Journal of Power Sources, 195(5), 1292–1301. https://doi.org/10.1016/j.jpowsour.2009.09.029

[175] **Zha, G., Hu, W., Agarwal, S., Ouyang, C., Hu, N., & Hou, H.** (2021). High performance layered lini0.8co0.07fe0.03mn0.1o2 cathode materials for Li-Ion Battery. Chemical Engineering Journal, 409, 128343. https://doi.org/10.1016/j.cej.2020.128343

[176] **Chen, M., Zhao, E., Chen, D., Wu, M., Han, S., Huang, Q., Yang, L., Xiao, X., & Hu, Z.** (2017). Decreasing li/ni disorder and improving the electrochemical performances of ni-rich Lini0.8co0.1mn0.1O2 by ca doping. Inorganic Chemistry, 56(14), 8355–8362. https://doi.org/10.1021/acs.inorgchem.7b01035

[177] **Weigel, T., Schipper, F., Erickson, E. M., Susai, F. A., Markovsky, B., & Aurbach, D.** (2019). Structural and electrochemical aspects of Lini0.8co0.1mn0.1O2 cathode materials doped by various cations. ACS Energy Letters, 4(2), 508–516. https://doi.org/10.1021/acsenergylett.8b02302

[178] **Konishi, H., Yoshikawa, M., & Hirano, T.** (2013). The effect of thermal stability for high-ni-content layer-structured cathode materials, lini0.8mn0.1−xco0.1moxo2 (x = 0, 0.02, 0.04). Journal of Power Sources, 244, 23–28. https://doi.org/10.1016/j.jpowsour.2013.05.004

[179] **Wang, J., Nie, Y., Miao, C., Tan, Y., Wen, M., & Xiao, W.** (2021). Enhanced electrochemical properties of ni-rich layered cathode materials via mg2+ and ti4+ co-doping for lithium-ion batteries. Journal of Colloid and Interface Science, 601, 853–862. https://doi.org/10.1016/j.jcis.2021.05.167

[180] **Gao, S., Zhan, X., & Cheng, Y.-T.** (2019). Structural, electrochemical and Li-ion transport properties of ZR-modified LiNi0.8Co0.1Mn0.1O2 positive electrode materials for Li-Ion Batteries. Journal of Power Sources, 410–411, 45–52. https://doi.org/10.1016/j.jpowsour.2018.10.094

[181] **Xin, F., Zhou, H., Zong, Y., Zuba, M., Chen, Y., Chernova, N. A., Bai, J., Pei, B., Goel, A., Rana, J., Wang, F., An, K., Piper, L. F., Zhou, G., & Whittingham, M. S.** (2021). What is the role of NB in nickel-rich layered oxide cathodes for lithium-ion batteries? ACS Energy Letters, 1377–1382. https://doi.org/10.1021/acsenergylett.1c00190

[182] **Zhang, D., Liu, Y., Wu, L., Feng, L., Jin, S., Zhang, R., & Jin, M.** (2019). Effect of ti ion doping on electrochemical performance of NI-rich Lini0.8Co0.1Mn0.1O2 Cathode material. Electrochimica Acta, 328, 135086. https://doi.org/10.1016/j.electacta.2019.135086

[183] **Dong, M., LI, X., WANG, Z., LI, X., GUO, H., & HUANG, Z.** (2017). Enhanced cycling stability of La modified Lini 0.8–X Co 0.1 mn 0.1 la x O 2 for Li-Ion Battery. Transactions of Nonferrous Metals Society of China, 27(5), 1134–1142. https://doi.org/10.1016/s1003-6326(17)60132-8

[184] **Lei, Y., Ai, J., Yang, S., Lai, C., & Xu, Q.** (2019). NB-doping in lini0.8co0.1mn0.1o2 cathode material: Effect on the cycling stability and voltage decay at high rates. Journal of the Taiwan Institute of Chemical Engineers, 97, 255–263. https://doi.org/10.1016/j.jtice.2019.02.006

[185] **Sidorov, N. V., Teplyakova, N. A., Makarova, O. V., Palatnikov, M. N., Titov, R. A., Manukovskaya, D. V., & Birukova, I. V.** (2021). Boron influence on defect structure and properties of lithium niobate crystals. Crystals, 11(5), 458. https://doi.org/10.3390/cryst11050458

[186] **Kim, U.-H., Park, G.-T., Son, B.-K., Nam, G. W., Liu, J., Kuo, L.-Y., Kaghazchi, P., Yoon, C. S., & Sun, Y.-K.** (2020). Heuristic solution for achieving long-term cycle stability for NI-rich layered cathodes at full depth of discharge. Nature Energy, 5(11), 860–869. https://doi.org/10.1038/s41560-020-00693-6

[187] **Colalongo, M., Ali, B., Martens, I., Mirolo, M., Laakso, E., Atzori, C., Confalonieri, G., Kus, P., Kobets, A., Kong, X., Schulli, T., Drnec, J., Kankaanpää, T., & Kallio, T.** (2024). Comprehensive study of zr-doped NI-rich cathode materials upon lithiation and co-precipitation synthesis steps. ACS Applied Materials & Interfaces, 16(22), 28683–28693. https://doi.org/10.1021/acsami.4c05058

[188] **Banerjee, H. & Grey, C.** (2024). Stability and Redox Mechanisms of Ni-Rich NMC Cathodes: Insights from First-Principles Many-Body Calculations. https://doi.org/10.1021/acs.chemmater.4c00928.s005

[189] **Url-7** Libretexts. (2023, June 21). 7.11: Electronegativity. Chemistry LibreTexts.https://chem.libretexts.org/Bookshelves/General_ Chemistry/ChemPRIME_(Moore_et_al.)/07:_Further_Aspects_of_Covalent_Bonding/7.11:_Electronegativity

[190] **Rahman, M. M., & Lin, F.** (2021). Oxygen redox chemistry in rechargeable Li-ion and Na-Ion Batteries. Matter, 4(2), 490–527. https://doi.org/10.1016/j.matt.2020.12.004

[191] **Url-8** Libretexts. (2023a, January 30). Polarizability. Chemistry LibreTexts. https://chem.libretexts.org/Bookshelves/Physical_and_Theoretical_Chemistry_Textbook_Maps/Supplemental_Modules_(Physical_and_Theoretical_Chemistry)/Physical_Properties_of_Matter/Atomic_and_Molecular_Properties/Polarizability

[192] **Ahrens, L.** Anion Affinity and Polarizing Power of Cations. Nature 169, 463 (1952). https://doi.org/10.1038/169463a0

[193] **U.S. National Library of Medicine.** (n.d.). Electronegativity. National Center for Biotechnology Information. PubChem Compound Database. https://pubchem.ncbi.nlm.nih.gov/ptable/electronegativity/

[194] **Ahaliabadeh, Z., Kong, X., Fedorovskaya, E., & Kallio, T.** (2022). Extensive comparison of doping and coating strategies for NI-rich positive electrode materials. Journal of Power Sources, 540, 231633. https://doi.org/10.1016/j.jpowsour.2022.231633

[195] **Dixit, M., Markovsky, B., Schipper, F., Aurbach, D., & Major, D. T.** (2017). Origin of structural degradation during cycling and low thermal stability of ni-rich layered transition metal-based electrode materials. The Journal of Physical Chemistry C, 121(41), 22628–22636. https://doi.org/10.1021/acs.jpcc.7b06122

[196] **Kleiner, K., Ying, B., Teng, Z., Avdeev, M., Senyshyn, A., Peng, J., Simonsen, S. B., Dolotko, O., Schmuch, R., Indris, S., Merz, M., Nagel, P., Schuppler, S., Ehrenberg, H., & Winter, M.** (2023). Insights into Homogenous Bulk Boron Doping at the Tetrahedral Site of NCM811 Cathode Materials: Structure Stabilization by Inductive Effect on Tm-O-B Bonds. https://doi.org/10.21203/rs.3.rs-3498657/v1

[197] **Zheng, C. (Allen).** (2022). Examining the benefits of using boron compounds in lithium batteries: A Comprehensive Review of Literature. Batteries, 8(10), 187. https://doi.org/10.3390/batteries8100187

[198] **Wu, C.-Y., Bao, Q., Tsai, Y.-T., & Duh, J.-G.** (2021). Tuning (003) interplanar space by boric acid co-sintering to enhance Li+ storage and transfer in Li(Ni0.8Co0.1Mn0.1)O2 Cathode. Journal of Alloys and Compounds, 865, 158806. https://doi.org/10.1016/j.jallcom.2021.158806

[199] **Park, K., Jung, H., Kuo, L., Kaghazchi, P., Yoon, C. S., & Sun, Y.** (2018). Improved cycling stability of Li[Ni0.90Co0.05Mn0.05]o2 through microstructure modification by boron doping for li-ion batteries. Advanced Energy Materials, 8(25). https://doi.org/10.1002/aenm.201801202

[200] **Xie, Q., Li, W., Dolocan, A., & Manthiram, A.** (2019). Insights into boron-based polyanion-tuned high-nickel cathodes for high-energy-density lithium-ion batteries. Chemistry of Materials, 31(21), 8886–8897. https://doi.org/10.1021/acs.chemmater.9b02916

[201] **Susai, F. A., Bano, A., Maiti, S., Grinblat, J., Chakraborty, A., Sclar, H., Kravchuk, T., Kondrakov, A., Tkachev, M., Talianker, M., Major, D. T., Markovsky, B., & Aurbach, D.** (2023). Stabilizing NI-rich high energy cathodes for advanced lithium-ion batteries: The case of lini0.9co0.1O2. Journal of Materials Chemistry A, 11(24), 12958–12972. https://doi.org/10.1039/d3ta00444a

[202] **Amalraj, S. F., Raman, R., Chakraborty, A., Leifer, N., Nanda, R., Kunnikuruvan, S., Kravchuk, T., Grinblat, J., Ezersky, V., Sun, R., Deepak, F. L., Erk, C., Wu, X., Maiti, S., Sclar, H., Goobes, G., Major, D. T., Talianker, M., Markovsky, B., & Aurbach, D.** (2021). Boron doped NI-rich lini0.85co0.10mn0.05o2 cathode materials studied by structural analysis, solid state NMR, computational modeling, and Electrochemical Performance. Energy Storage Materials, 42, 594–607. https://doi.org/10.1016/j.ensm.2021.08.005

[203] **Lee, S.-H., Jin, B.-S., & Kim, H.-S.** (2019). Superior performances of B-doped LiNi0.84Co0.10MN0.06O2 Cathode for advanced libs. Scientific Reports, 9(1). https://doi.org/10.1038/s41598-019-54115-z L.-Y. Kuo, O. Guillon, P. Kaghazchi, ACS Sustainable Chem. Eng. 2021,9, 7437

[204] **Hu, G., Wang, W., Du, K., Peng, Z., Zeng, J., Li, L., & Cao, Y.** (2022). Enhancing the electrochemical performance of co-less ni-rich Lini0.925Co0.03Mn0.045O2 cathode material via co-modification with Li2b4o7 coating and B3+ doping. SSRN Electronic Journal. https://doi.org/10.2139/ssrn.4092192

[205] **Zhang, N., Li, Y., & Qiao, Y.** (2021). Boosting the electrochemical performance of lini0.6mn0.2co0.2o2 through a trace amount of Mg-B co-doping. Journal of Materials Science & Technology, 89, 167–178. https://doi.org/10.1016/j.jmst.2021.02.023

[206] **Huang, B., Yang, X., Xu, G. et al.** Boron-doped single crystal LiNi0.6Mn0.2Co0.2O2 with improved electrochemical performance for lithium-ion batteries. Ionics 25, 5819–5827 (2019). https://doi.org/10.1007/s11581-019-03166-3

[207] **Lv, Y., Huang, S., Lu, S., Ding, W., Yu, X., Liang, G., Zou, J., Kang, F., Zhang, J., & Cao, Y.** (2022). B2O3/LIBO2 dual-modification layer stabilized NI-rich cathode for lithium-ion battery. Journal of Power Sources, 536, 231510. https://doi.org/10.1016/j.jpowsour.2022.231510

[208] **Kim, K.J., Jo, Y.N., Lee, W.J., Subburaj, T., Prasanna, K., Lee C.W.** (2014) Effects of inorganic salts on the morphological, structural, and electrochemical properties of prepared nickel-rich Li[Ni0.6Co0.2Mn0.2]O2, J. Power Sources, 268, 349-355.

[209] **Roitzheim, C., Kuo, L.-Y., Sohn, Y. J., Finsterbusch, M., Möller, S., Sebold, D., Valencia, H., Meledina, M., Mayer, J., Breuer, U., Kaghazchi, P., Guillon, O., & Fattakhova-Rohlfing, D.** (2021). Boron in NI-rich NCM811 cathode material: Impact on atomic and Microscale Properties. ACS Applied Energy Materials, 5(1), 524–538. https://doi.org/10.1021/acsaem.1c03000

[210] **You, B., Wang, Z., Chang, Y., Yin, W., Xu, Z., Zeng, Y., Yan, G., & Wang, J.** (2023). Multi-scale boron penetration toward stabilizing nickel-rich cathode. Fundamental Research, 3(4), 618–626. https://doi.org/10.1016/j.fmre.2022.03.001

[211] **Elgrishi, N., Rountree, K. J., McCarthy, B. D., Rountree, E. S., Eisenhart, T. T., & Dempsey, J. L.** (2017). A practical beginner's guide to cyclic voltammetry. Journal of Chemical Education, 95(2), 197–206. https://doi.org/10.1021/acs.jchemed.7b00361

[212] **Hassanzadeh-Tabrizi, S. A.** (2023). Precise calculation of crystallite size of nanomaterials: A Review. Journal of Alloys and Compounds, 968, 171914. https://doi.org/10.1016/j.jallcom.2023.171914

[213] **Kushwaha, P., & Chauhan, P.** (2021). Microstructural evaluation of iron oxide nanoparticles at different calcination temperature by Scherrer, Williamson-hall, size-strain plot and Halder-Wagner methods. Phase Transitions, 94(10), 731–753. https://doi.org/10.1080/01411594.2021.1969396

[214] **Lee, K. E., Kim, Y., Kim, J. S., Kim, K. S., Hong, K. J., Nam, S.-C., Kim, H., Lee, D., & Park, K.-Y.** (2024). Comparison study of a thermal-driven microstructure in a high-ni cathode for lithium-ion batteries: Critical calcination temperature for polycrystalline and single-crystalline design. ACS Applied Materials & Interfaces. https://doi.org/10.1021/acsami.4c00514

[215] **Li, H., Li, J., Ma, X., & Dahn, J. R.** (2018). Synthesis of single Crystal Lini0.6mn0.2co0.2O2with enhanced electrochemical performance for Lithium Ion Batteries. *Journal of The Electrochemical Society*, *165*(5). https://doi.org/10.1149/2.0951805jes

[216] **Choi, J., Dong, L., Yu, C.-Y., O'Meara, C., Lee, E., & Kim, J.-H.** (2021). Relationship of chemical composition and moisture sensitivity in Linixmnyco1−x−yO2 for lithium-ion batteries. Journal of Electrochemical Energy Conversion and Storage, 18(4). https://doi.org/10.1115/1.4051208

[217] **Busà, C., Belekoukia, M., & Loveridge, M. J. (2021).** The effects of ambient storage conditions on the structural and electrochemical properties of NMC-811 cathodes for Li-Ion Batteries. *Electrochimica Acta*, *366*, 137358. https://doi.org/10.1016/j.electacta.2020.137358

[218] **Xin, F., Goel, A., Chen, X., Zhou, H., Bai, J., Liu, S., Wang, F., Zhou, G., & Whittingham, M. S.** (2022). Electrochemical characterization and microstructure evolution of ni-rich layered cathode materials by niobium coating/substitution. Chemistry of Materials, 34(17), 7858–7866. https://doi.org/10.1021/acs.chemmater.2c01461

CURRICULUM VITAE

Name Surname **:** İbrahim Can TOPAKTAŞ

EDUCATION **:**

- **B.Sc.** **:** 2020, Istanbul Technical University, Engineering Faculty, Metallurgical and Materials Engineering

PUBLICATION, PRESENTATIONS AND PATENTS ON THE THESIS:

- **Topaktaş, İ. C.,** Karahan, B. D, Keleş Ö., **"**The Effects of Feeding Rate and the Calcination Conditions on the NMC811 Cathodes for Lithium-ion Batteries" International Graduate Research Symposium (IGRS'24), İstanbul, Turkey, 8-10 May, 2024